PLASMA-BASED SYNTHESIS OF NANOSTRUCTURED MATERIALS AND THEIR CHARACTERIZATION

by

RAKESH P CHAUDHARY

Presented to the Faculty of the Graduate School of
The University of Texas at Arlington in Partial Fulfillment
of the Requirements
for the Degree of

DOCTOR OF PHILOSOPHY

THE UNIVERSITY OF TEXAS AT ARLINGTON
May 2017

Acknowledgements

I would like to express my deepest appreciation and gratitude to my advisor Professor Ali R. Koymen for his support and guidance throughout this thesis. I would like to thank Professor Yaowu Hao for allowing me access to his laboratory and Professor Muhammad N. Huda for a fruitful collaboration. I would also like to express my appreciation to Professors Yaowu Hao, Muhammad N. Huda, Qiming Zhang and Alex Weiss for serving in my dissertation supervisory committee.

I would also like to thank our collaborators Dr. Samarendra K. Mohanty, Dr. Kim Kangasniemi, Dr. Masaya Takahashi, and Dr. “Max” Qinhong Hu for allowing use of their research facility and for their help in measurements. I appreciate and thank Physics department and staff for their support. I am indebted to my colleagues and I appreciate creative discussions with Sajib, Orathai Thumthan and Dr. Chienwen Huang (Kevin). Most of all, I want to thank my wife Kinjal, who more than anyone has provided inspiration, counsel, friendship and love. This work is dedicated to her. I finally would like to thank my family in India for supporting me throughout my studies.

April 19, 2017

Abstract

PLASMA-BASED SYNTHESIS OF NANOSTRUCTURED MATERIALS AND THEIR CHARACTERIZATION

Rakesh P Chaudhary, PhD

The University of Texas at Arlington, 2017

Supervising Professor: Ali R. Koymen

The aim of this thesis is to explore the novel cost-effective synthesis technique to develop nanostructured materials and investigate their structural and magnetic properties. Nanomaterials were synthesized by a plasma discharge between desired metal electrodes in the cavitation field of an organic solvent. Multifunctional core-shell magnetic nanoparticles of 3d transition elements (Fe, Ni) and bimetallic (FeNi) were synthesized by varying experimental conditions. The phase, crystallinity and the magnetic properties of the materials synthesized were found to be dependent on experimental reaction parameters such as different solvents, electrodes, the spacing between electrodes, applied voltage, experiment time and high-temperature annealing. Fe and Gd-based nanoparticles were developed for high-performance magnetic resonance imaging (MRI) contrast enhancement. Biocompatible hybrid composite of Fe core – C shell nanoparticles evaluated as negative MRI contrast agents display remarkably high transverse relaxivity (r_2) of 70 $mM^{-1}S^{-1}$ at 7T.

In addition to 3d transition magnetic materials, magnetism of multilayer graphene nanosheets with only s and p electrons was investigated to understand and explain the intrinsic origin of ferromagnetism in carbon-based material. Apart from magnetic

materials, noble metal Pd nanoparticles were developed using one-step process for hydrogen storage. The role of hydrogen on the dilation of Pd lattice was investigated using the experiment and density functional theory (DFT) studies. This method demonstrates that plasma discharge method using appropriate electrodes and solvents can be used to synthesize desired nanoparticles. This potential emphasizes the importance of adopting this methodology, which offers advantages that include a rapid reaction rate and ability to form very small nanoparticles with narrow size distribution.

Table of Contents

List of Illustrations

List of Tables

Chapter 1

Magnetism and magnetic materials

1.1 Basics of magnetism

Magnetic properties of substances are due to the existence of orbital and spin magnetic moments of electrons. Their interactions are the basis of creating macroscopic ordered substances that have various behaviors when interacting with a magnetic field.

The moment due to orbital motion of an electron is

$$\mu(orbit) = \frac{eh}{4\pi m} \tag{1.1}$$

where μ is an orbital magnetic moment of the atom, m is the mass of the electron, e is the charge of the electron, and h is the Planck constant. The moment due to spin of an electron is

$$\mu(spin) = \frac{eh}{4\pi m} \tag{1.2}$$

The natural unit for electronic magnetism is, therefore, the Bohr magneton, defined as

$$\mu_B = \frac{eh}{4\pi m} = 9.27 \times 10^{-24}\, A\, m^2 \tag{1.3}$$

The characterization of magnetic properties is made using magnetization M and magnetic susceptibility χ expressed as

$$M = \frac{m}{V} \tag{1.4}$$

where m is a magnetic moment and V is volume.

$$\chi = \frac{M}{H} \tag{1.5}$$

where H is a magnetic field.

The variation of these parameters with temperature (T) and external field: M (H), M (T) and χ (T) are generally investigated and used to describe magnetic properties of substances. The following classification distinguishes the ordered substances based on the collective interaction of atomic moments [1].

1.2 Classification of magnetism

1.2.1 Diamagnetism

Diamagnetism is a fundamental property of all matter, although it is usually very weak. Diamagnetic substances are composed of atoms which have no net magnetic moments (i.e., all the orbitals are filled and there are no unpaired electrons). However, when exposed to a field *H*, the magnetic moments are induced in the opposite direction from the external field. The main characteristics are a temperature independent susceptibility and a negative magnetization produced under an external field. The susceptibility χ is < 0 (order of 10^{-6} per unit volume) for diamagnetic materials [1-4].

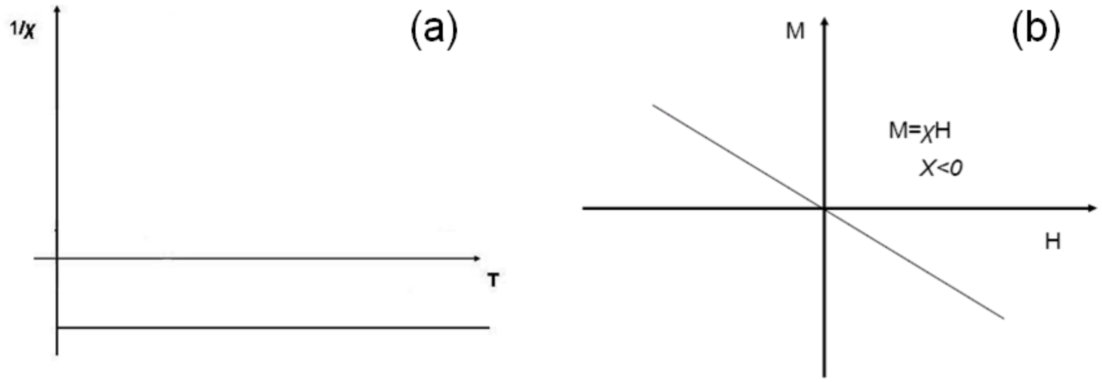

Figure 1.1 Diamagnetic systems: (a) Inverse susceptibility dependence with temperature and (b) Magnetization as a function of the external magnetic field.

1.2.2 Paramagnetism

This behavior is observed for atoms which have a net magnetic moment due to unpaired electrons in partially filled orbitals. In the presence of an external field, there is a partial alignment of the atomic moments with the field direction, resulting in a net positive magnetization. However, the magnetization is zero when the external field is removed because there is no cooperative interaction between magnetic moments. The Curie law $\chi = \frac{C}{T}$ gives a temperature dependent susceptibility. The susceptibility χ is > 0 (in the order of 10^{-5} –

10^{-3}) for paramagnetic materials [1, 2, 4]. The efficiency of an external field in aligning the moments is opposed by randomizing effects of temperature.

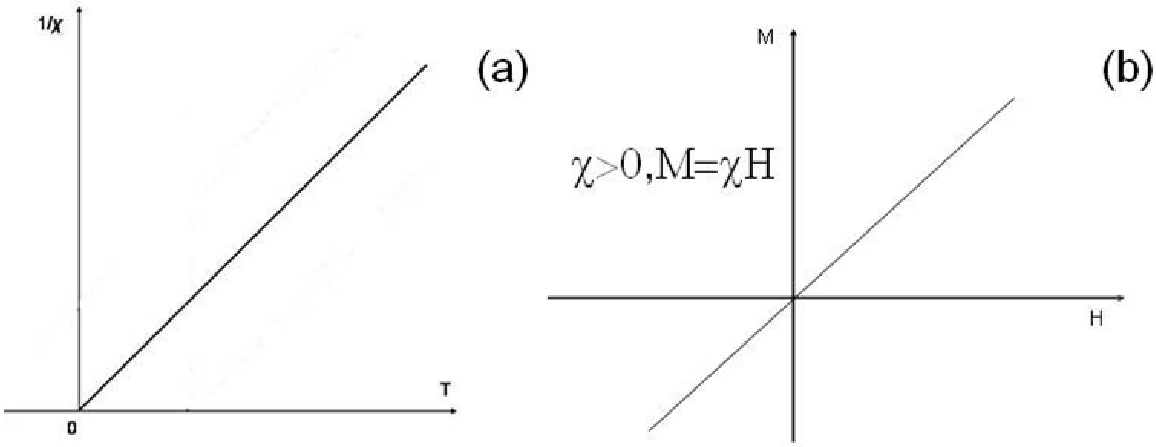

Figure 1.2 Paramagnetic system: (a) Inverse susceptibility dependence with temperature and (b) Magnetization as a function of external magnetic field.

1.2.3 Ferromagnetism

Ferromagnetism is characteristic for atoms which have permanent magnetic moments. There is strong interaction between atomic moments which keep them aligned even in the absence of an applied magnetic field. These moments originate from the overall contribution of electron spin and orbital magnetic moments. The elements Fe, Ni, and Co and many of their alloys are typical ferromagnetic materials [5, 6]. Magnetic susceptibility as high as 10^6 is possible for ferromagnetic materials [7-17].

Two distinct characteristics of ferromagnetic materials are their spontaneous magnetization and the existence of magnetic ordering temperature. The spontaneous magnetization is the net magnetization that exists inside a uniformly magnetized microscopic volume in the absence of an external field. As temperature increases, the arrangements of atomic moments are disturbed by the thermal agitation, resulting in the temperature dependence of spontaneous magnetization. In spite of the presence of spontaneous magnetization, a large piece of ferromagnetic or ferromagnetic substance is usually not spontaneously magnetized but exists

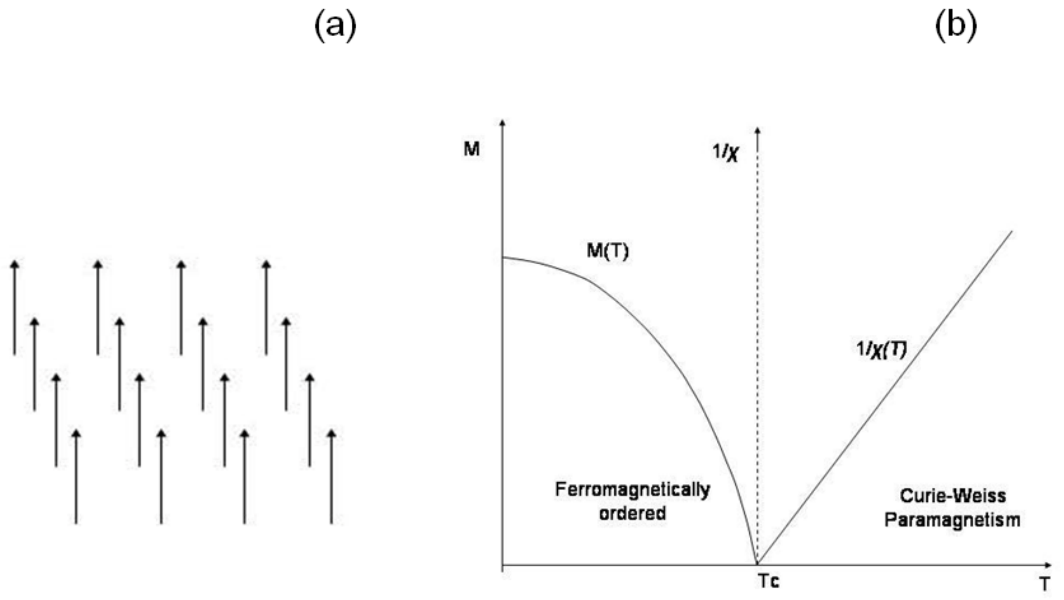

Figure 1.3 (a) Ferromagnetic order below T_C and (b) Magnetization and inverse susceptibility dependence with temperature.

rather in a demagnetized state. This is because the interior of the piece is divided into many magnetic domains, each of which is spontaneously magnetized. Since the direction of domain magnetization varies from domain to domain, the resultant magnetization can be changed from zero to the value of spontaneous magnetization. The saturation magnetization (M_s) is the maximum induced magnetic moment that can be obtained in a magnetic field beyond which no further increase in magnetization occurs. Saturation magnetization is an intrinsic property and dependent on temperature.

Above T_C, Curie temperature, the special order disappears and the substance is paramagnetic: the orientation of the moments is random due to the thermal agitation, each moment acting independent of the others. Below T_C, the individual magnetic moments of the atoms are lined up and they act together as a very large magnetic moment [1-4].

1.2.4 Antiferromagnetism

In the case of antiferromagnetic order, the magnetic moments are lined up but the adjacent moments are aligned in opposite directions to each other. The result will be a small value of magnetic moment M. M (H) is similar with a paramagnet, but the origin is quite different: the antiferromagnetic state is a long range order state.

Above a certain temperature, Neel temperature - T_N (figure 1.4), the substances is paramagnetic, and the same Curie-Weiss law $\chi = \frac{C}{T-\theta}$, will describe the susceptibility temperature dependence, with the paramagnetic temperature, $\theta<0$, $\theta \neq T_N$.

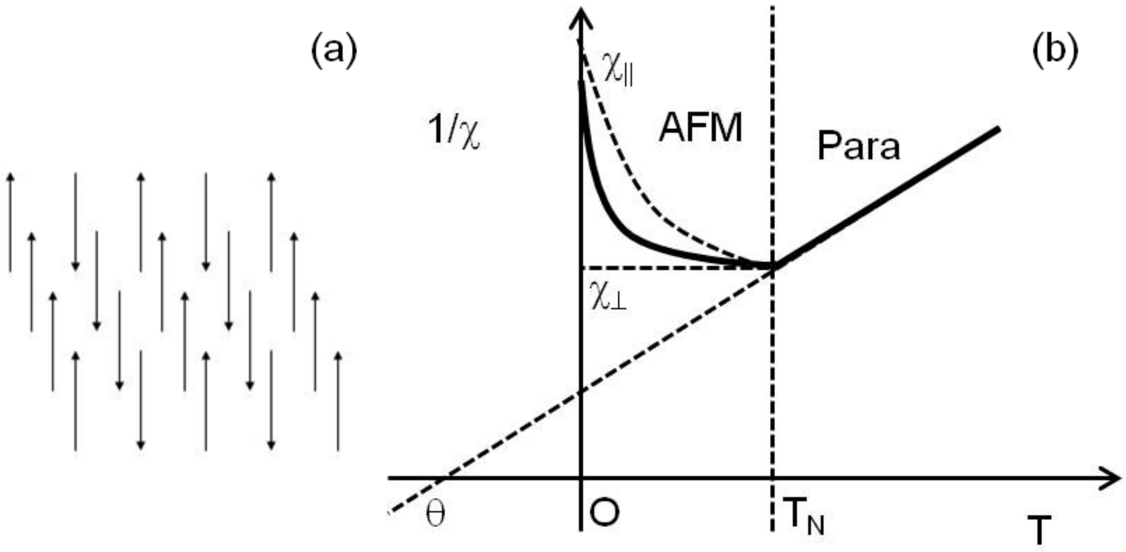

Figure 1.4 (a) Antiferromagnetic order and (b) Inverse susceptibility dependence with temperature.

If the field is applied parallel to the moment axis there will be a net change in the magnetization as each of the sublattices change their magnetization magnitude. If the field is applied perpendicular to the field axis the change in net magnetization is due to the orientation change for each sublattice. Some examples of antiferromagnetic crystals are manganese oxide (MnO), manganese sulfide (MnS), Cobalt/Cobalt Oxide (Co/Co) and iron oxide (FeO) [1-4, 12, 18].

1.2.5 Ferrimagnetism

The ferrimagnetic order is very similar to the antiferromagnetic at the atomic level: the adjacent magnetic moments are locked in opposite directions, but with distinctive magnitudes (figure1.5). There is a certain temperature called compensation temperature, T_{comp}, where the opposite magnetic moment will cancel each other and the net magnetization for the system is zero. The behavior in an externally applied field of the ferrimagnetic substances is similar to the ferromagnetic substances: M (H) shows hysteresis and above Curie temperature, the magnetic order disappears.

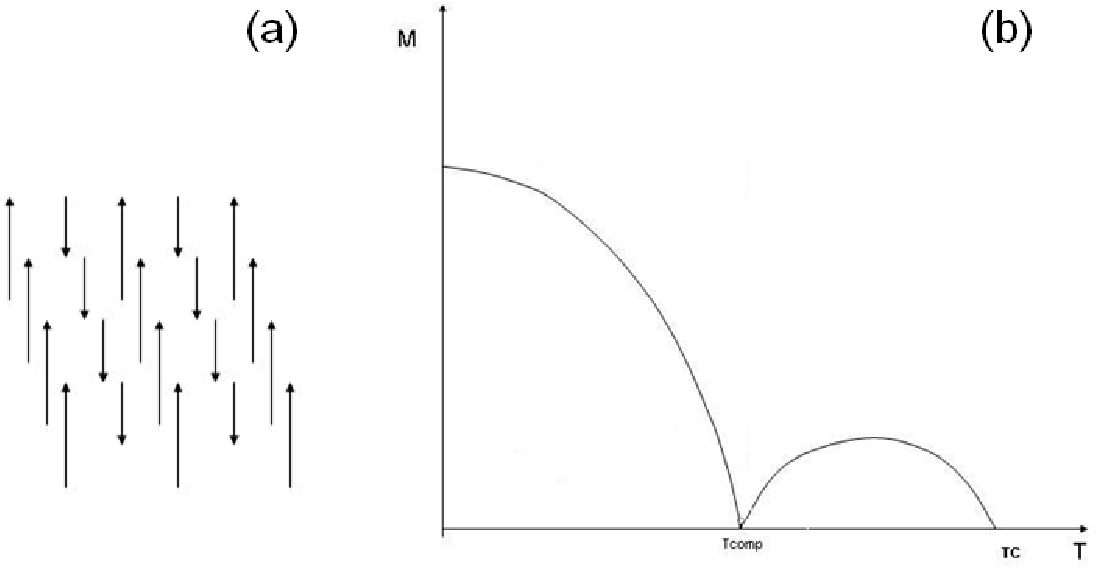

Figure 1.5 a) Ferrimagnetic order and b) Magnetization dependence with temperature for a ferrimagnetic system.

1.3 Characteristics of ferromagnetic materials

1.3.1 Curie temperature

Even though electronic exchange forces in ferromagnets are very large, thermal energy eventually overcomes the exchange interaction and produces a randomizing effect. This effect becomes dominant at a particular temperature called the Curie temperature (T_C). Below the Curie temperature, the magnetic structure is ordered, and above the Curie temperature, the magnetic structure is disordered. The saturation magnetization goes to zero at the Curie temperature. The Curie temperature is an intrinsic property of materials and is a diagnostic parameter that can be used for mineral identification. However, it is not full proof because different magnetic minerals, in principle, can have the same Curie temperature [1-4].

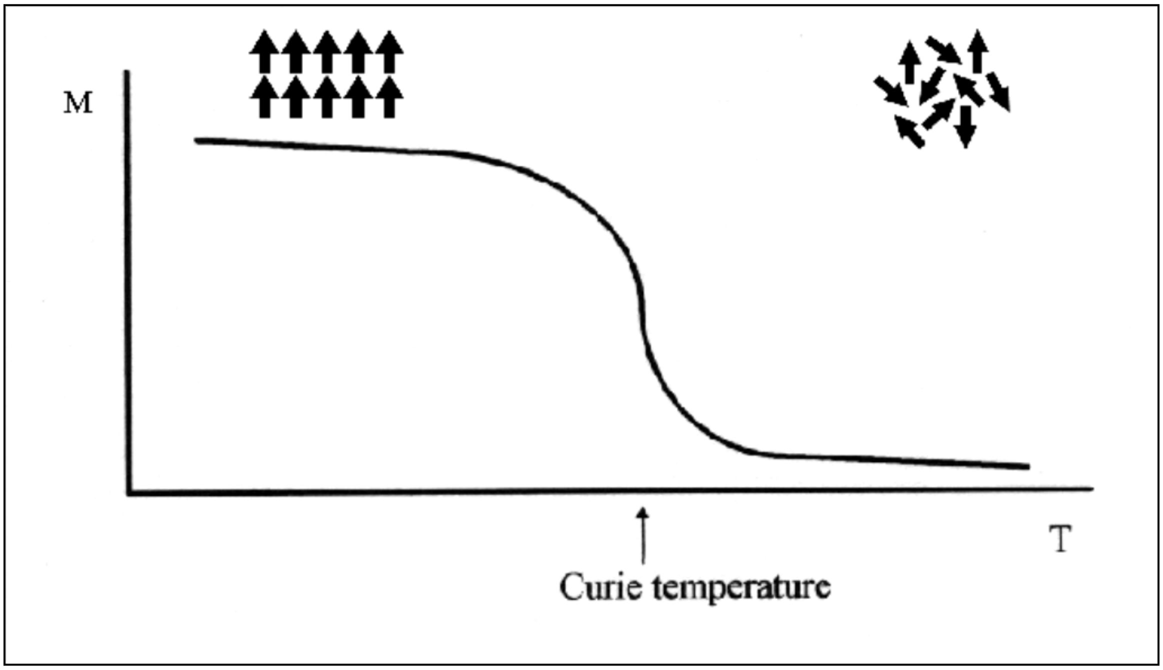

Figure 1.6 Magnetization as a function of temperature for the Curie transition in a ferromagnetic material. Different spin ordering is displayed for the ferromagnetic region (below T_C) and the paramagnetic region (above T_C).

1.3.2 Magnetic domains

Many magnetic materials do not exhibit any magnetization if no external magnetic field is applied. Weiss attributed this “absence” of magnetism to the formation of domains in polycrystals: domains are magnetized in different directions so that the average net magnetization is almost zero.

The alignment of the different magnetic dipoles in a superparamagnetic, ferromagnetic or ferrimagnetic material creates a magnetic field in space that is associated with an energy value. This energy can be minimized by creating oppositely faced domains in the material, so that the field, and consequently also the energy, are decreased. The so-called ‘‘domain walls’’ that are thus created carry a certain value of energy associated as well. The formation of domains is in fact governed by the minimization of the total energy.

Domain walls are the region between the domains. Classification of domain walls can be made according to the angle between two adjacent domains. As shown in Figure 1.6, a 180° domain wall separates domains of opposite magnetizations and a 90° domain wall separates domains with perpendicular magnetizations.

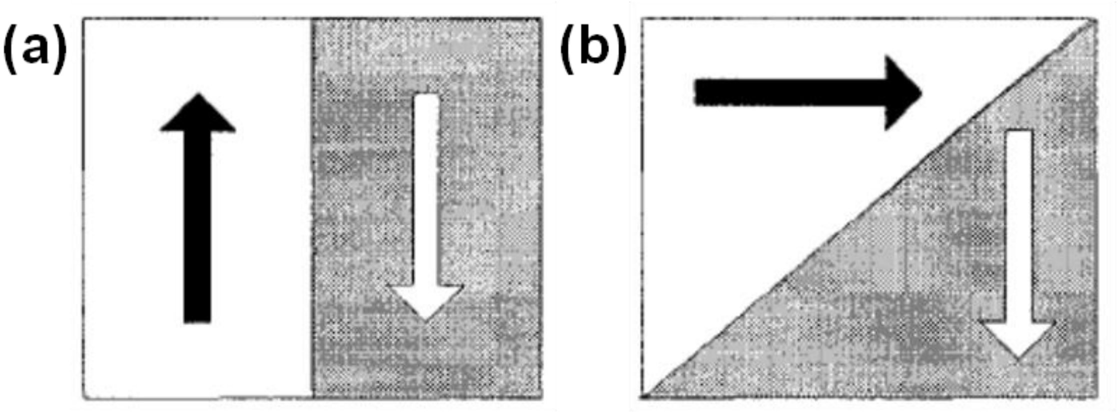

Figure 1.7 (a) 180° domain wall and (b) 90° domain wall.

The most common type of 180° domain wall is a Bloch wall in which the magnetization rotates in the plane parallel to the domain wall. The other possible configuration is the Neel wall where the magnetization in the domain wall rotates in a plane perpendicular to the plane of the wall.

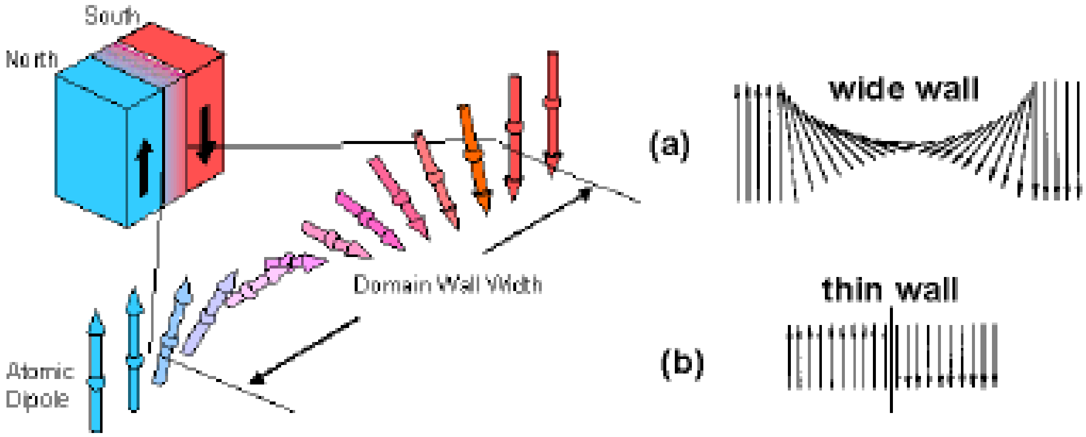

Figure 1.8 Schematic representation of a 180 º domain wall with (a) wide wall with gradual magnetization change, and (b) thin wall with abrupt magnetization change.

Domain walls have a finite width that is determined principally by exchange and magnetocrystalline anisotropy energy. Exchange energy tends to keep magnetic moment parallel to each other and can be kept small if the 180 ° rotation takes place gradually with the wide wall as shown in Figure 1.8 (a), but large with the thin wall as shown in Figure 1.8 (b). However, for the wide wall structure, the magnetizations within the wall are no longer aligned along an easy axis of magnetization. This produces an anisotropy energy, which is high in (a) but low in (b). The exchange energy tends to make the wall as wide as possible whereas the anisotropy tends to make the wall as thin as possible. As a result of this competition between exchange and anisotropy energies, the domain wall has a finite width (on the order of few nanometers).

1.3.3 Hysteresis loops

Ferromagnets can retain the memory of an applied field even after the field is removed. This behavior is called hysteresis, and a plot of the variation of magnetization with magnetic field shown in Figure 1.9 is called a hysteresis loop [19, 20]. The hysteresis loop is a means of characterizing magnetic materials, and various parameters can be determined from it.

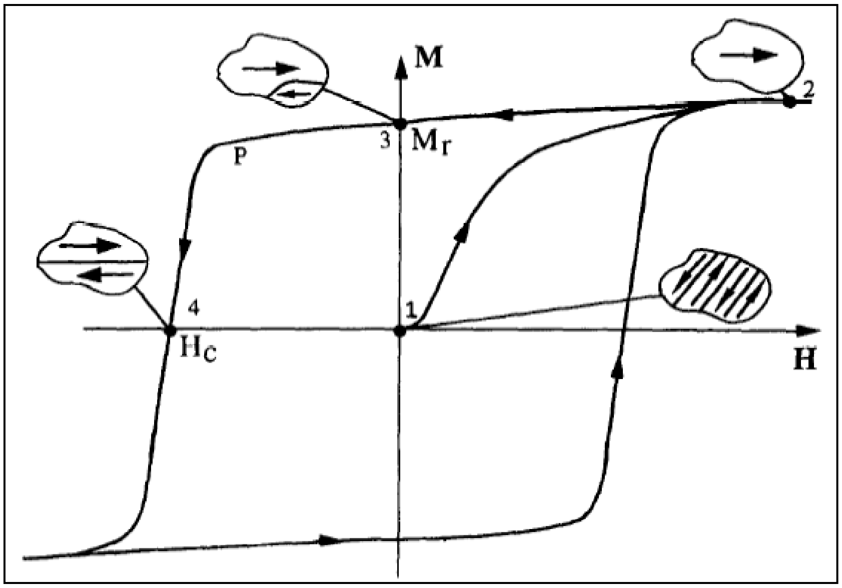

Figure 1.9 The magnetization curve and hysteresis loop of a permanent magnet showing the magnetic domain structure in the (1) virgin state, (2) at saturation, (3) at remanence, and (4) at the coercive field.

Initially, the moments of the constituent domains are randomly oriented in such a way that there is no net *B (or M)* field. As shown in Figure 1.9, on the application of a field to an unmagnetized sample, the polarization increases initially by the growth of favorably oriented domains, which will be magnetized in the easy direction of the crystal. When the polarization can increase no further by the growth of domains, the direction of magnetization of the domains then rotates away from the easy axis to align with the field. When all of the domains have fully aligned with the applied field, saturation is reached, and the polarization can increase no further. The maximum value of M is called the saturation magnetization M_S, and the resultant M-H curve is called the initial magnetization curve. Starting from the saturation point (see Figure 1.9), when the H field is reduced, the curve does not retrace its original path. A hysteresis effect is produced in which the M field lags behind the applied H field or decreases at a lower rate. At zero field, a residual M is called the remanence or remanent magnetization Mr is retained, indicating that the material remains magnetized even in the absence of an external H field. The polarization will only decrease after a sufficiently high field is applied to (1) nucleate and grow domains favorably oriented with respect to the applied field or (2) rotate the direction of magnetization of the domains towards the applied field. After applying a high enough reversal field, saturation polarization will be achieved in the negative direction. If the applied field is then decreased and again applied in the positive direction then the full hysteresis loop is plotted (Figure 1.9). The area contained within the loop indicates the amount of energy absorbed by the material during each cycle of the hysteresis loop. The reverse field required to bring the magnetic induction B of a specimen to zero is called the inductive coercivity (H_b) whereas the reverse field required to bring the magnetization M to zero is called the intrinsic coercivity (H_C). The remanence ratio M_r/M_s is generally used as a measure of squareness of the *M- H* loop.

1.3.4 Magnetic anisotropy

1.3.4.1 Magnetocrystalline anisotropy

In a magnetic material, the electron spin is coupled to the electronic orbital (spin-orbital coupling) and influenced by the local environment (crystalline electric field). Because of the arrangement of atoms in crystalline materials, magnetization along certain orientations is energetically preferred. Magnetocrystalline anisotropy is an intrinsic property. The magnetization process is different when the field is applied along different crystallographic directions, and the anisotropy reflects the crystal symmetry. For a cubic crystal, the anisotropy energy is often expressed as

$$E_{MC} = K_0 + K_1(cos^2\theta_1 cos^2\theta_2 + cos^2\theta_2 cos^2\theta_3 + cos^2\theta_3 cos^2\theta_1)$$
$$+K_2 cos^2\theta_1 cos^2\theta_2 cos^2\theta_3 + \dots\dots\dots\dots \quad (1.6)$$

where $K_0, K_1, K_2 \dots$ are anisotropy constantsθ_1, θ_2 and θ_3 are the angles between the magnetization direction and the three crystal axes, respectively. K_0 is independent of angle and can be ignored since it is the difference in energy between different crystal orientations that is of interest. In many cases, terms involving K_2 are small and can also be neglected.

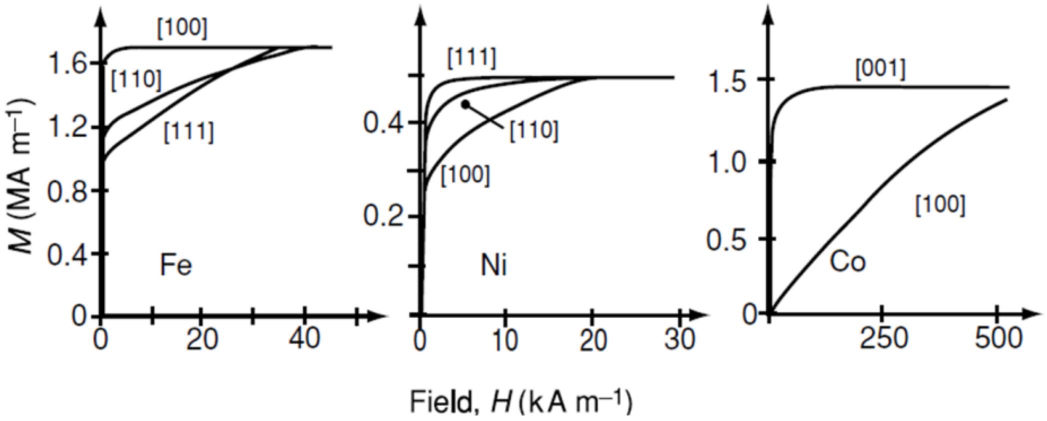

Figure 1.10 Magnetization of single crystals of Fe, Ni, and Co.

The magnetocrystalline anisotropy energy associated with a hexagonal close-packed crystal is expressed as

$$E_{MC} = K_0 + K_1 sin^2\theta + K_2 sin^4\theta \tag{1.7}$$

where K_0, K_1, and. K_2 are anisotropy constants and θ is the angle between the magnetization direction and the *c*-axis. If $K_1 > 0$, the energy is smallest when $\theta = 0$, i.e., along the c-axis, so that this axis is the easy axis. If $K_1 < 0$, the basal plane is the easy axis. As a result of the symmetry of the hexagonal close-packed lattice, the magnetocrystalline anisotropy is a uniaxial anisotropy. Magnetization curves for single crystals of Iron, Nickel, and Cobalt showing easy, medium and hard magnetization direction is shown in Figure 1.10 [20]. The magnitude of anisotropy constants K_1 and K_2 for various bulk materials are given in Table 1-1 [1].

Table 1 Magnitude of the magnetocrystalline anisotropy constants K_1 and K_2 of Fe, Ni, and Co at room temperature.

Material	K_1(J/m^3)	K_2(J/m^3)
bcc-Fe	4.8×10^4	-0.5×10^4

fcc-Ni	- 0.5 ×10^4	- 0.2 × 10^4
hcp-Co	4.5 ×10^5	1.5 × 10^5

1.3.4.2 Shape anisotropy

The magnetization of a spherical object in an applied magnetic field is independent of the orientation of the applied field. However, it is easier to magnetize a non-spherical object along its long axis than along its short axis [21]. If a rod-shaped object is magnetized with a north pole at one end and a south pole at the other, the field lines emanate from the north pole and end at the south pole. Inside the material, the field lines are oriented from the north pole to the south pole and hence they are opposed to the magnetization of the material, since the magnetic moment points from the south pole to the north pole. Thus, the magnetic field inside the material tends to demagnetize the material and is known as the demagnetizing field $\overrightarrow{H_d}$.

In uniformly magnetized ellipsoids [20], if the magnetization lies along a principle direction, then the demagnetizing field is also uniform and given by:

$$\overrightarrow{H_d} = -N\vec{M}, \tag{1.8}$$

where N is the demagnetizing factor and is dependent on the shape of the body, but can only be calculated exactly for an ellipsoid where the magnetization is uniform throughout the sample.

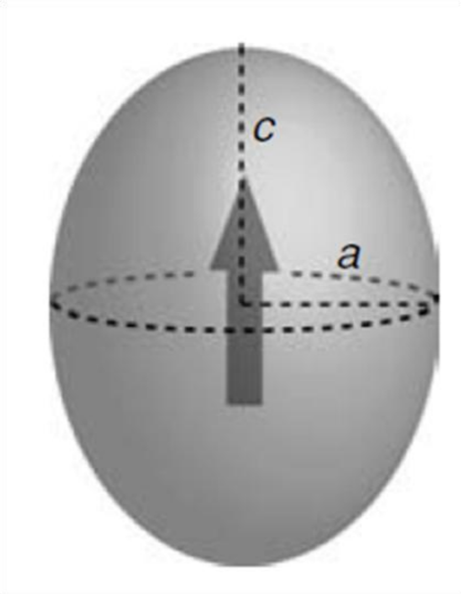

Figure 1.11 Magnetization of a prolate ellipsoid of revolution with c > a and no magnetocrystalline anisotropy. The c axis is the easy direction of magnetization.

The energy of demagnetizing field then becomes:

$$E_d = \frac{1}{2}\mu_0 VN\vec{M}, \tag{1.9}$$

where N is the demagnetizing factor and V is the volume of the ellipsoid. Other simple shapes can be approximated to ellipsoids. The anisotropy energy is related to the difference in energy ΔE_d when the ellipsoid is magnetized along its hard and easy directions. N is the demagnetizing factor for the easy direction; $N' = \frac{1}{2}(1 - \mathrm{N})$ is the demagnetizing factor for the perpendicular, hard directions (Table 1-2) [3]. Hence $\Delta E_d = \frac{1}{2}\mu_0 VM^2\left[\frac{1}{2}(1-N) - N\right]$, this gives for a prolate ellipsoid

$$K_{sh} = \frac{1}{4}\mu_0 M^2(1-3N) \tag{1.10}$$

This is zero for a sphere $\left(N = \frac{1}{3}\right)$, as expected. Shape anisotropy is only fully effective in samples which are so small that they do not break up into domains.

Table 2 Demagnetizing factors N for finite rods magnetized parallel to long axis.

Aspect ratio (length/diameter)	*N*
0	1
1	0.27
2	0.14
5	0.04
10	0.0172
20	0.00617

1.3.5 Soft magnets

Magnetic materials are broadly classified into two main groups: soft and hard depending on their hysteresis characteristics. Soft magnetic materials can be easily magnetized and demagnetized by low-strength magnetic field. When an applied field is removed, soft magnetic materials will return to a state of relatively low residual magnetization. Soft magnetic materials are used primarily to enhance or channel the flux produced by an electric current. The main parameter, which is often used as a figure of merit for soft magnetic materials, is the relative permeability, which is a measure of how readily the material responds to the applied magnetic field. The other main parameters of interest are the coercivity, the saturation magnetization, and the electrical conductivity. Figure 1.12 shows a typical MH loop for soft magnetic materials which have an intrinsic coercivity of less than 100 Oe and high saturation magnetization M_S but low M_r.

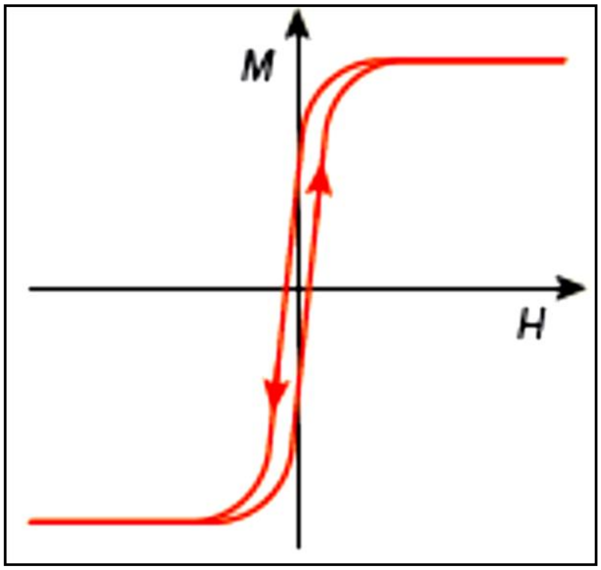

Figure 1.12 The magnetization curve and hysteresis loop of a soft magnet.

1.3.6 Permanent magnets

Hard magnets, also referred to as permanent magnets, are magnetic materials that can retain their magnetism after being magnetized. The term “hard” is used to describe materials that have sufficiently high resistance to demagnetizing field. Coercivity is, therefore, the key to distinguishing between hard and soft phase magnetic materials. As shown in Figure 1.13, materials that have an intrinsic coercivity of greater than 1000 Oe and typically high remanence *Mr* are hard magnetic materials [22-28]. Such material has high energy product $(BH)_{max}$ *[9]*, which is the figure of merit of the permanent magnet.

Maximum Energy Product *(BH)max:* In *B-H* loop, the maximum value of the product of *B* and *H* is called the maximum energy product, (*(BH)max)* and is a measure of the maximum amount of useful work that can be performed by the magnet. Its unit is KJ/m^3 (MGOe). For a permanent magnetic material, the *(BH)max* is twice the maximum magnetostatic energy available from a magnet of optimal shape. The product tends to increase with both increasing coercive field *Hc* and saturation magnetization *Ms.* However, for materials with sufficiently high *Hc* values (*Hc* >

2πMs), the theoretical limit for the energy product is limited only by *Ms* and is given by $(BH)max \leq (2\pi Ms)^2$.

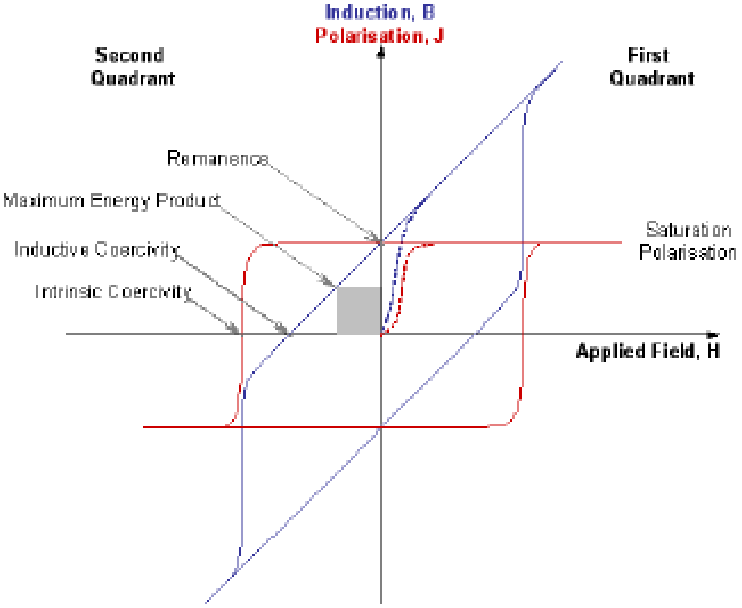

Figure 1.13 Typical *M-H* and *B-H* loops of ferromagnetic materials.

1.3.7 Magnetism in particles

Ferromagnetic nanoparticles (also called as magnetic nanoparticles) exhibit a variety of unique magnetic phenomena that is drastically different from those of their bulk counterparts because of the high surface to volume ratio of the particle at nanometer scale. Magnetic properties of small ferromagnetic particles, such as coercivity and saturation magnetization, are mainly dominated by two key features: (1) a size limit below which the specimen cannot be broken into domains, and so it remains with single domain; and (2) the thermal energy in small particles, which decouples the magnetization from the particle itself to give rise to the phenomenon of superparamagnetism. These two key features are represented by two key sizes (on the length scale): the single domain size and the superparamagnetic size as shown in Figure 1.14 [1, 19].

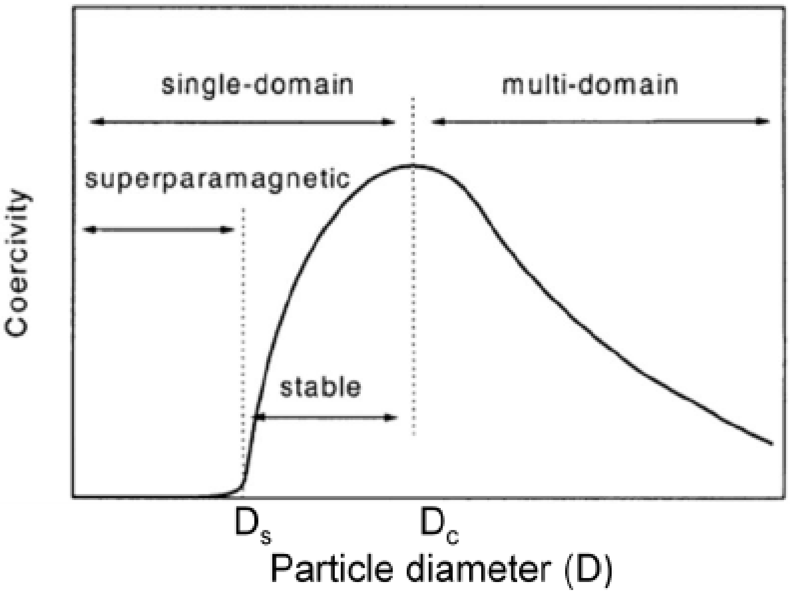

Figure 1.14 Variation of coercivity with particle diameter.

1.3.7.1 Single-domain particles

The magnetostatic energy of a ferromagnet could be decreased by restructuring the material into domains. There is a limit to this because the formation of domains costs energy as a result of domain wall formation. Thus, in a large body, there could be minimum domain size below which the energy cost of domain formation exceeds the benefits of decreasing the magnetostatic energy. When the size of the magnets decreases to a critical particle diameter, the formation of domain walls is energetically less favorable, and the magnets have only a single domain. Technological applications of single-domain magnetic particles depend critically on our fundamental understanding of spin rotation dynamics and their dependence on the particle's intrinsic spin structure. The simplest model proposed by Stoner and Wohlfarth [10] in their pioneering work on moment reversal in single-domain magnetic particles, assumes coherent spin rotation whereby all spins within the single-domain particle are collinear and rotate in unison. It predicts the field strength necessary to reverse the spin orientation direction or coercive field, H_C.

The model assumes uniform magnetization throughout the particle, which remains so throughout the rotation process, an assumption that allows for exact solutions, but not generally observed experimentally. Additional models, allowing for non-uniform, incoherent spin reversal mechanisms have also been developed [29-32]. Generally, the energies required to reverse the spin orientation within a single-domain particle are larger than those needed to induce domain wall movement, yielding coercivity larger than those of the bulk. Figure 1.15 shows the dependence of coercivity as a function of particle size for Co, Fe, and iron oxide particles reproduced from the classic paper by Luborsky [33].

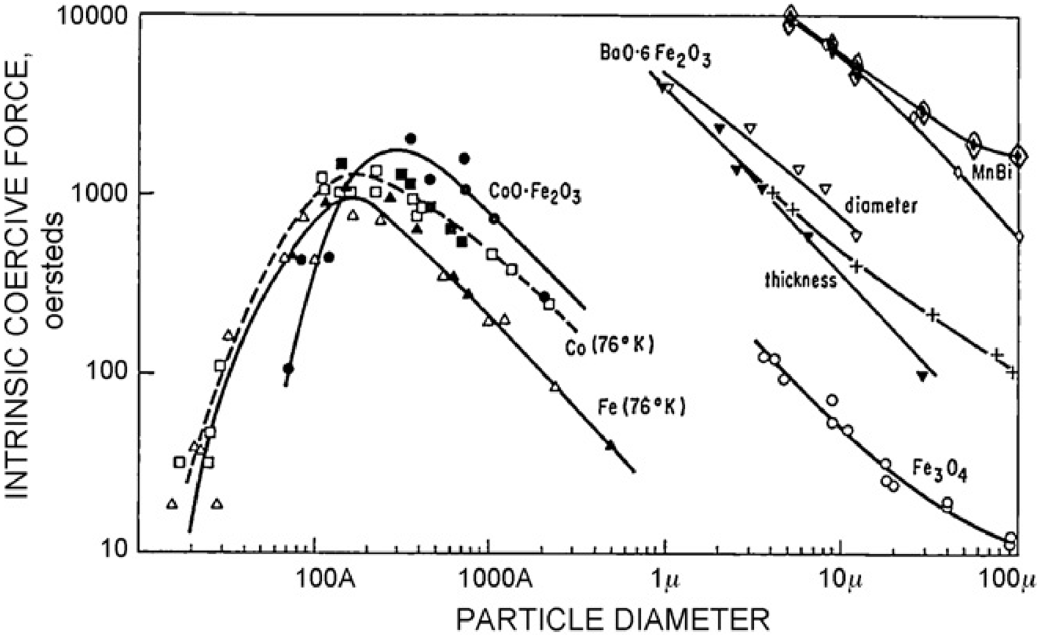

Figure 1.15 Experimental relation between coercivity and diameter for particles deriving their coercive force principally from crystal anisotropy energy.

1.3.7.2 Superparamagnetism

Superparamagnetism is a phenomenon where magnetic materials exhibit a behavior similar to paramagnetism at temperatures below the Curie or the Neel temperature. Superparamagnetism occurs when the material is composed of very small crystallites (1-20 nm). In this case, even though the temperature is below the Curie or Neel temperature, the thermal energy is sufficient to overcome the coupling forces between neighboring atoms and to change the direction of magnetization of the entire crystallite. The material behaves in a manner similar to paramagnetic materials and the magnetic moment of the entire crystallite tends to align in a random way without a magnetic field. The energy required to change the direction of magnetization of a crystallite is called the crystalline anisotropy energy (*KV*) and depends on both on the materials properties and the crystallite size. As the crystallite size decreases, so do the crystalline anisotropy energy, resulting in a decrease in the temperature at which the material becomes superparamagnetic. A typical hysteresis loop of superparamagnetic nanoparticles is shown in Figure 1.16 with Hc = 0 and Mr/ Ms = 0.

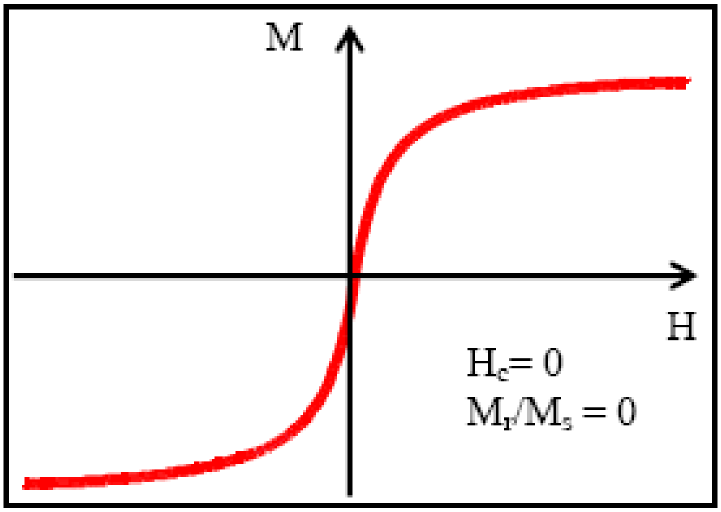

Figure 1.16 A typical M vs H loop for superparamagnetic particles.

The phenomenon of superparamagnetism is timescale-dependent due to the stochastic (random variable) nature of the thermal energy. The time scale for a successful jump can be calculated by:

$$\tau = \tau_0 e^{-KV/k_B T} \tag{1.11}$$

where the attempt timescale τ_0 is about 10^{-9} S, and V is the volume of the particle. This equation (1.7) describes the time scale over which the moment of the particles ($\mu_\rho = M_S V$) attempts to jump the anisotropy energy (*KV*) barrier as shown in Figure 1.17 [34].

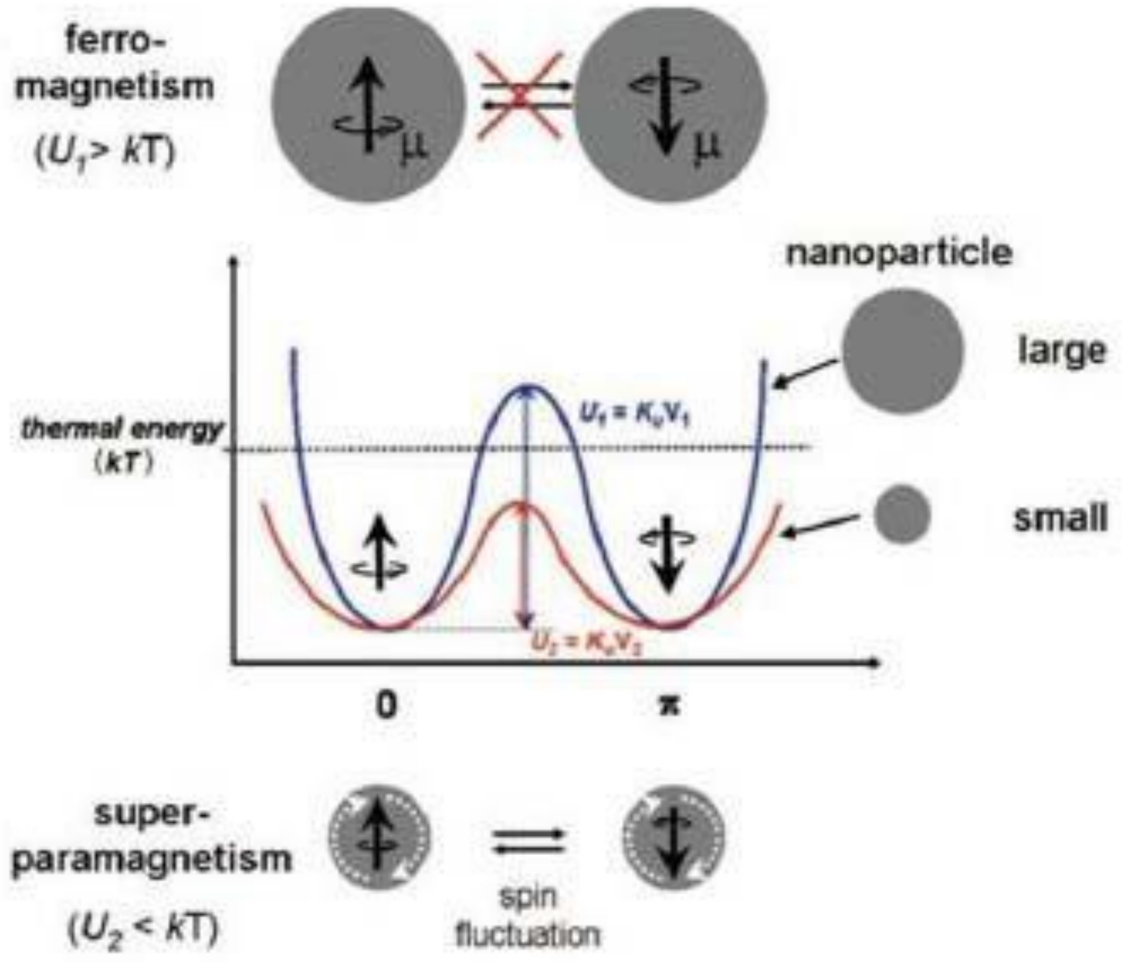

Figure 1.17 Energy diagram of magnetic nanoparticles with different magnetic spin alignment, showing ferromagnetism in a large particle (top) and superparamagnetism in a small nanoparticle (bottom).

Typical experiments with a magnetometer take 10 to 100 s; if Ms reversed at times shorter than the experimental time scale, the system appears superparamagnetic. Using τ=100 s and τ_0=10^{-9} s, we can obtain the critical volume from equation (1.7):

$$V_{sp} = 25k_BT/K \tag{1.12}$$

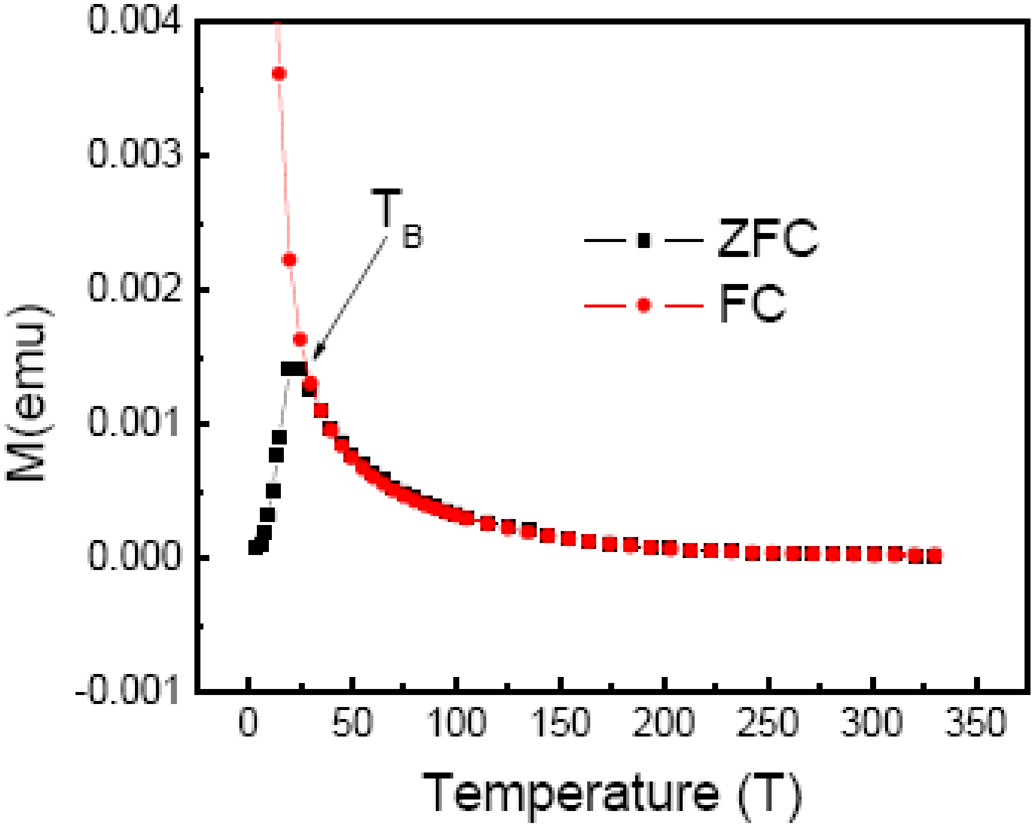

Figure 1.18 Typical ZFC and FC curves showing the blocking temperature of nanoparticles.

A particle with a volume smaller than this quantity behaves as superparamagnetic on the 100 s experimental timescale. Equation (1.8) can be rearranged to yield

$$T_B = KV/25k_B \tag{1.13}$$

T_B is called the blocking temperature; below T_B, the free movement of the moment of particles ($\mu_p = M_sV$) is blocked by the anisotropy; above T_B, k_BT kicks the moment loose so that the system appears superparamagnetic. Blocking temperature (T_B) which is characteristic for ferromagnetic to superparamagnetic transition can be ascertained in nanoparticles by measuring the zero field cooling (ZFC) and field cooling (FC) magnetization temperature as shown in Figure 1.18. As the particles cool in a zero applied field, they will tend to magnetize along preferred crystalline directions in the lattice, thus minimizing the magneto-crystalline energy. Since the orientation of each crystallite varies, the net moment of the system will be zero. Even when a small external field is applied, the moments will remain locked in the preferred crystal directions, as is seen in the low-temperature portion of the ZFC curve. As temperature increases, more thermal energy is available to disturb the system. Therefore, more moments will align with the external field direction in order to minimize the Zeeman energy term. In other words, thermal vibration is providing the activation energy required for the Zeeman interaction. Eventually, the net moment of the system reaches a maximum where the greatest population of moments has aligned with the external field. The peak temperature is called the blocking temperature (T_B). As the temperature rises above T_B, thermal vibrations become strong enough to overcome the Zeeman interaction and thus randomize the moments.

Field cooled (FC) measurements proceed in a similar manner to ZFC, except that the constant external field is applied while cooling and heating. However, the net moment is usually measured while heating. The FC curve will diverge from the ZFC curve at a point near the blocking temperature as seen in Figure 1.18. This divergence occurs because the spins from each particle will tend to align with the easy crystalline axis that is closest to the applied field direction, and will remain frozen in that direction at low temperature [35-37].

Chapter 2

Synthesis of nanostructured materials

The preparation of nanoparticles has received considerable attention in recent decades due to unique physical and chemical properties of nanoparticles [38]. Notable efforts have been devoted to the critical aspect of developing nanoparticles with narrow size and spatial distribution that enables the optimization of these properties for a broad range of applications. There are two basic paradigms for the fabrication of materials in the nanoscale: top-down and bottom-up approaches.

The top-down approach commonly refers to the selective sculpting, or etching, of a bulk material for cutting structures down to the nanoscale regime. The bottom-up approach, on the other hand, aims to create structures by piecing them up together from atomic and molecular-scale components.

Common bottom-up techniques are the template-assisted electrochemical deposition [39, 40] and solution-based growth approaches [41]. A range of solution-based approaches have been used for the preparation of metallic nanoparticles including; co-precipitation [42], sol–gel encapsulation [43], polyol [7, 13, 37], solvothermal [9, 28, 37], hydrothermal [11, 15, 17, 37], combustion [44] , sonochemical [23], and microemulsion methods [45]. These methods differ in degree of complexity (multi-step), production, purity, safety, and economics.

Common top-down techniques are ball milling [26], arc discharge [46], laser ablation [47] and plasma methods [6, 48, 49]. Among these, the top-down approach appears to be the most promising alternative to synthesizing nanoparticles. Throughout this research work, plasma discharge synthesis method caused by ultrasonic cavitation was adopted. This method offers unique advantage which includes a rapid reaction rate with the ability to form very small nanoparticles with a narrow size distribution.

Studies on the use of high-intensity ultrasound for the preparation of organic and inorganic materials have been on the increase. Ultrasonic cavitation is an efficient method to concentrate low-density elastic wave energy into higher densities, as a result of the rapid collapse of cavitation bubbles produced in a suitable liquid medium [50]. The overall picture of cavitation bubble formation is as follows. As an elastic (sound) wave passes through a liquid, it produces alternating regions of reduced density (negative pressure) and increased density (positive pressure). If the sound wave is sufficiently intense, the reduced density regions form cavities (bubbles) filled with the saturated vapor of the liquid. Any gases dissolved in the fluid diffuse through the cavity walls and also contribute to the vapor inside the bubble.

In the contraction phase, the cavity collapses under the effect of positive pressure and surface tension forces, and the vapor-gas mixture within experiences a rapid and strong compression. Depending upon the cavitation conditions, at the moment of collapse, the pressure, P, and temperature, T, inside the cavity may reach extremely high instantaneous values, $P \sim 10^5$–10^6 bar, $T \sim 1000$K [51]. As a result of the simultaneous collapse of many cavities, a cavitation zone is formed in the ambient fluid. The cavitation zone can be considered to be a peculiar kind of "power transformer", in which energy is accumulated rather slowly (∼ 10ms) during the negative pressure phase, but which is released on a very short timescale (∼ 1ns). As a result, the instantaneous power is many orders of magnitude greater than that of the average power introduced to the cavitation medium. These extreme conditions create a specific physical and chemical medium for the realization of many chemical reactions, such as for obtaining nanomaterials [52-54]. An ultrasonic cavitation field, with its many activated tiny bubbles, enhances electrical conductivity due to the radicals and free electrons formed within it. Thus, an electric plasma discharge can be generated at a relatively low electric power, even in insulating organic liquids, such as benzene [46]. Without the ultrasonic irradiation, no plasma discharge can take place at such low electric power levels. Thus, in contrast to traditional arc-discharge units requiring high-power, expensive vacuum equipment, plasma discharge produced under low electric power with ultrasonic irradiation in an organic liquid is cost effective and simpler.

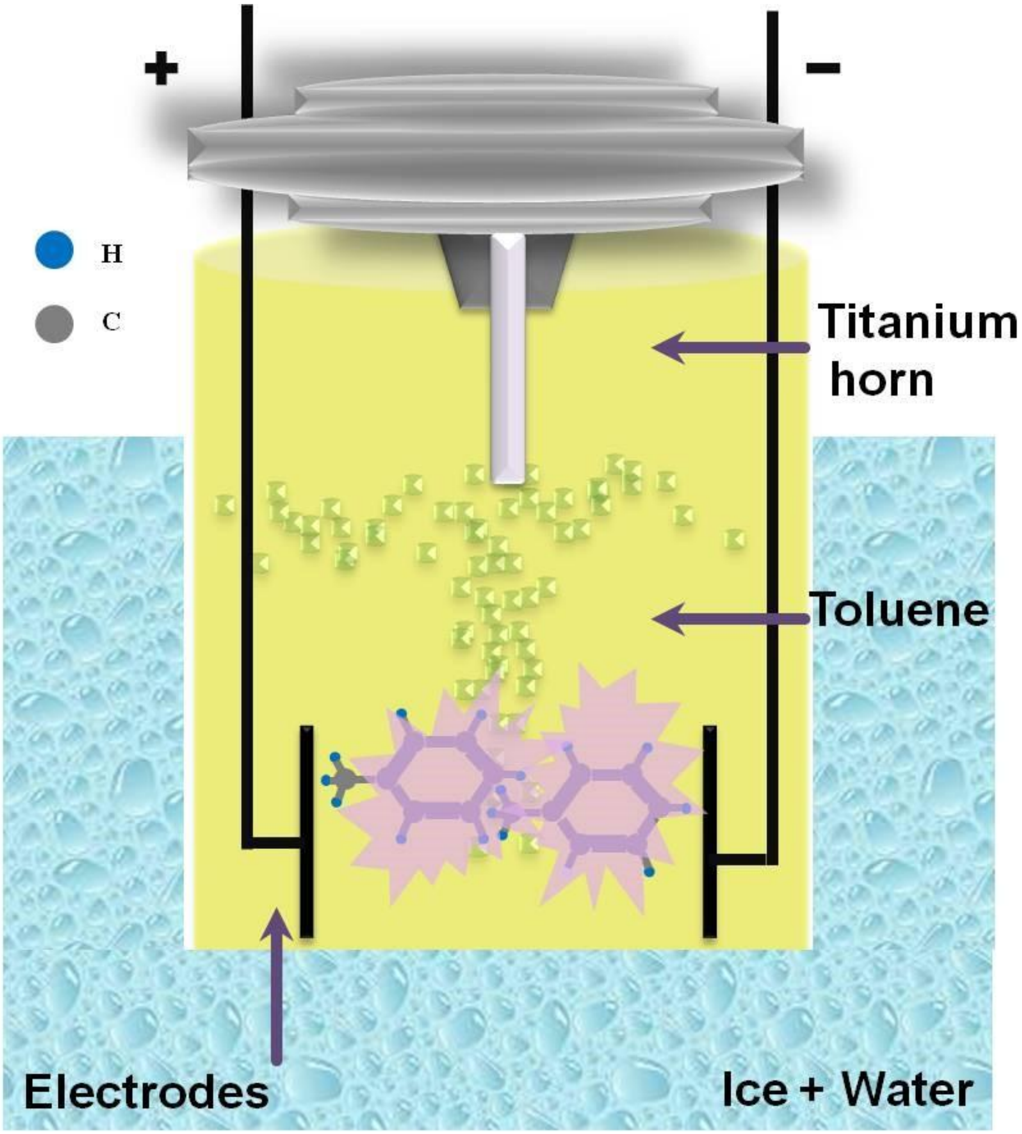

Figure 2.1 Schematic of experimental set up used to synthesize the nanoparticles.

The ultrasonic cavitation field [55, 56] consisting of thousands of tiny bubbles permits the plasma discharge to occur in an insulating solution such as benzene. Figure 2.1 shows a schematic diagram of the experimental apparatus. An ultrasonic processor (Sonics, VCX 750) with a titanium horn 19 mm in diameter was used in the experiment to irradiate 275 ml of benzene (Sigma Aldrich, anhydrous 99.8%) at 750 watts and 20 kHz. A glass vessel filled with ice water was underneath and an Argon gas flow was directed into the closed geometry containing benzene to maintain an inert atmosphere. As shown in figure 1, two electrodes (0.5 mm in diameter) were inserted 0.5 mm apart from each other beneath the bottom of the ultrasonic horn. The distance between the electrodes and the bottom of the horn was kept constant at 10 mm. During the ultrasonic irradiation, the voltage on the electrodes was kept fixed using a constant voltage power unit.

Plasma was generated in the cavitation field just beneath the horn. The current on the electrodes became momentarily higher when the plasma discharge occurred. However, without ultrasonic irradiation, no plasma was generated and sustained with currently used power supply. Ultrasonic cavitation causes a very high localized high temperature and pressure region where thousands of tiny bubbles are collapsing, a region recognized as a so-called hot spot [55-57]. The collapse of cavitation between electrodes in a strong electric field polarizes the π-electrons in toluene and thus creates a plasma. The dissociation of hydrogen and carbon in toluene due to the breaking of chemical bonds leads to a unique way of hydrogen production. Quasi-stable nanoparticles are formed when energetic plasma encounters electrodes either by nucleation in the vapor or molten form and then after the rapid quenching, stable nanoparticles are formed [6, 48, 49, 58]. The plasma discharge was stable during the experiment and hence the positions of the electrodes were fixed throughout the experiment. The experiment continued for an hour, during which particles appeared and were dispersed in the benzene. The liquid turned uniformly black. Evidently, in the static condition particles were condensed and precipitated in the liquid. Benzene molecules can be decomposed into small fragments and/or atoms by plasma discharge in the ultrasonic cavitation field. Due to rapid quenching by the surrounding liquid, they evolve into more stable compounds such as nanoparticles embedded in a carbon matrix.

Chapter 3

Characterization techniques

In this chapter, a summary of the characterization techniques that have been used throughout this Ph.D. work is presented. Transmission electron microscopy (TEM), high-resolution TEM (HRTEM), and powder and X-ray diffraction (XRD) were used for structural characterization. Inductively coupled plasma-optical emission spectroscopy (ICP-OES) and energy dispersive X-ray (EDX) was used for compositional characterization of nanoparticles. A Vibrating Sample Magnetometer (VSM) and a superconducting quantum interference device (SQUID) magnetometer were used for magnetic characterization. A brief description of these equipment and characterization techniques and the techniques used to prepare samples are following.

3.1 X-ray diffraction

Powder X-ray diffraction (XRD) spectra were recorded on a Bruker D8 diffractometer with a Cu K-α wavelength X-ray source. The samples were prepared by drop casting dispersions of nanowires in toluene on a glass substrate. The samples were dried under ambient conditions.

The X-ray diffraction (XRD) is a powerful tool for structural characterization of crystalline materials to determine detailed information on the structure of a material such as crystalline phases, grain sizes, strain, texture etc. The X-rays interact with the electrons in the atoms, when passes through the sample, resulting in scattering of the radiation. The wavelength of the X-ray radiation has values of 1 Å in the order of the lattice parameters in crystalline solids. Thus, if the distance between the atoms is close to the wavelength of the X-rays, interference of the scattered waves in these solids will occur and form a diffraction pattern with constructive and destructive interferences. The X-rays are scattered at characteristic angles based on the spaces between the atomic planes defining their crystalline structure. Since most crystals have several sets of planes passing through their atoms, each of them has a specific interplanar distance and will originate a characteristic angle of diffracted X-rays. The intensity maximum of the diffraction pattern will appear for scattering directions which are univocally related with specific reciprocal lattice vectors of the solid. These directions determine the so-called Bragg reflections (giving Bragg peaks in the spectra) and a set of Miller indexes (hkl) can be assigned to them. The relationship between wavelength (λ) atomic spacing (d_{hkl}) and diffraction angleθ, is given by the Bragg's law:

$$n\,\lambda = 2d_{hkl}\,sin\,\theta, \tag{3.1}$$

where λ is the wavelength of the incident wave, d_{hkl} is the distance between the planes with the miller indexes (hkl), and the angle θ formed by the propagating vectors of the incident and scattered waves shown in Figure 3.1 [59].

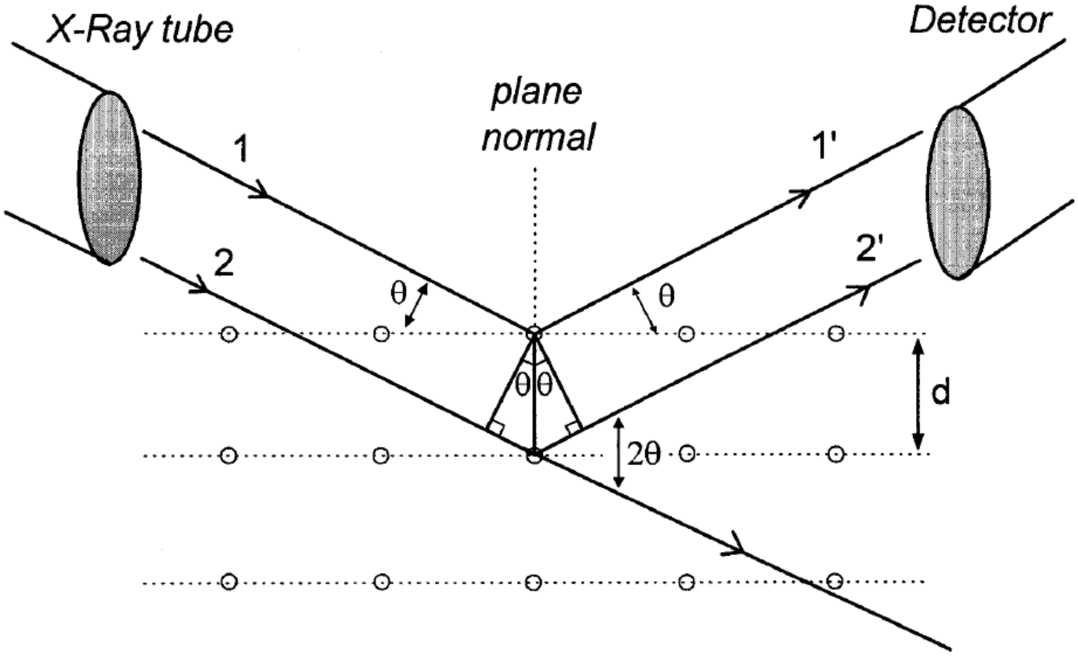

Figure 3.1 X-Ray diffraction by a crystal.

From the broadening it is possible to determine an average crystallite size, in Å, by Debye-Scherrer formula:

$$d_{hkl} = k\,\frac{\lambda}{\beta\,cos\,\theta}, \tag{3.2}$$

where k = 0.8-1.39 (usually close to the unity e.g. 0.9, considering spherical grains), the wavelength λ of the radiation λ_{Cu} = 1.54056 Å, β is the full width at half maximum, or half-width in radians and θ is the position of the maximum of diffraction.

3.2 Transmission electron microscopy

Transmission electron microscopy (TEM) uses the same principle as light (optical) microscopy. Optical microscopy uses light photons, focused or diverged by glass lenses to form a magnified image of a given sample; TEM uses electrons in combination with electromagnetic lenses which can focus the electron beam but (unlike glass lenses and light) cannot diverge it. Owing to the high acceleration used in TEM (typically several hundred kV) the wavelength of the accelerated electrons is far shorter than the typical wavelength of light, making the resolving power of an electron microscope far greater than that of its counterpart.

3.2.1 Electron diffraction

A diffraction pattern arises when the near-parallel electron beam generated by the electron source and projected onto the sample by the condenser lens system in an electron microscope is diffracted (elastically scattered) by the crystal lattice of the studied specimen. Bragg's law of diffraction states that only certain scattering is allowed giving rise to a diffraction pattern in the back-focal plane of the objective lens (objective aperture position in Figure 3.2 below).

To obtain diffraction pattern from a small region of the sample, usually a Selective Area Diffraction aperture (SAED) aperture is used. The spacing between the spots in a given pattern is directly related to inter-planar distances in the crystalline material. The angles between the reflections together with the presence or absence of certain reflections can be used to determine the crystal structure and orientation of a sample. In nanocrystalline materials, a diffraction pattern is mostly obtained from several crystals simultaneously when using parallel illumination. The different orientations of the simultaneously studied nanocrystals lead to a rotational average of the diffraction pattern of the individual crystals called a diffraction ring pattern. Although crystallographic orientation (angular) information is not present in such a diffraction ring pattern, the crystal phase of the studied sample can be easily determined from one. As the spacings of the rings are directly related to the inter-planar distances in the material, they are also directly related to the crystal phase. In effect, an electron ring pattern is near identical to a powder XRD spectrum, except that the scattering nature of electrons is dynamical while that of X-rays is kinematical.

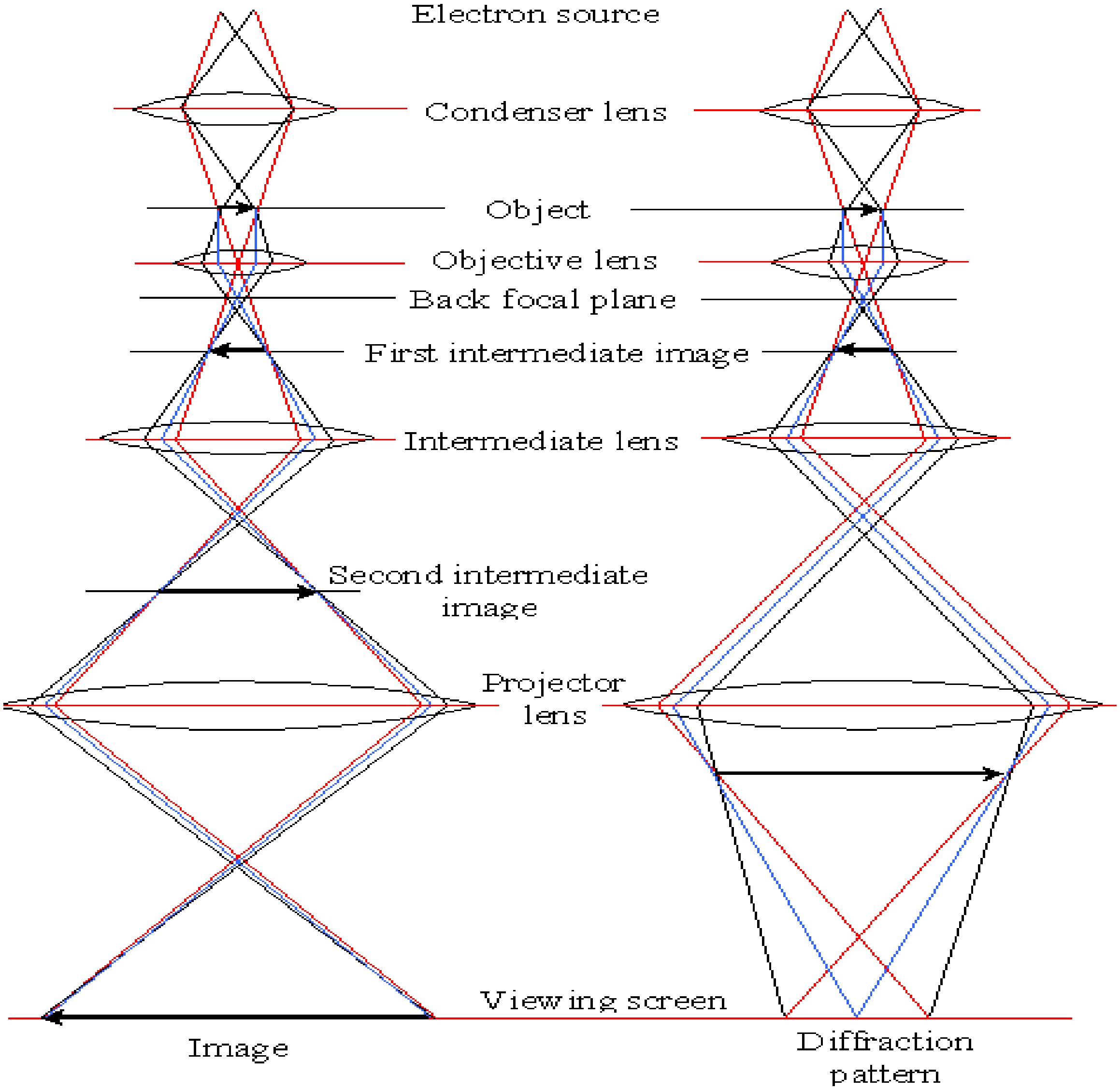

Figure 3.2 Ray diagram for two basic modes of operation in a TEM a) bright field imaging b) selected area electron diffraction (SAED).

Diffraction and imaging in an electron microscope go hand in hand. This follows from the fact that in the electron microscope the electrons are focused using round electromagnetic lenses, which are known to effectively perform Fourier Transforms. This means that the back focal plane of the objective lens is in principle nothing more than the Fourier Transform of the real space sample. In other words; the image and the diffraction pattern of a certain specimen in a well-defined orientation are each other's Fourier Transform. Using the setup of the electron microscope, the operator can perform instant Fourier Transforms by switching between diffraction mode (Fourier space) and imaging mode (Real space) with a simple press of a button. The intermediate and the projector lenses in the microscope are setup in such a way that either a magnified image or the diffraction pattern of the sample is projected on the viewing screen or CCD camera. The ray diagrams for both diffraction and imaging are displayed in Figure 3.2.

3.2.2 Bright field imaging

The general mode of operation in a TEM is so called bright-field imaging. In this mode, the sample is probed using a parallel incoming electron beam (see Figure 3.2).In general , only a small amount of the electrons that have passed through the specimen are used for imaging in the bright-field imaging mode. An objective aperture is placed in the back focal plane of the objective lens to cut out all electrons except the transmitted beam or a selected amount of reflections. This cutting provides a bright field image with enhanced contrast.

3.2.3 High-resolution transmission electron microscopy

Unlike X-ray or neutron diffraction, electron diffraction is highly dynamical, meaning that multiple electron scattering with large phase changes occurs frequently in an electron microscope. In high-resolution transmission electron microscopy (HRTEM) a large objective aperture is inserted in the back focal plane of the objective lens, allowing diffracted beams to interfere both with each other and the transmitted beam, forming an interference (fringe) pattern. As a result the contrast in such an image is dependent on the phase of the various beams giving rise to the name phase contrast imaging for HRTEM imaging.

In high-resolution imaging, it is useful to think of the electron microscope as an information transfer process. The incident electron wave is a plane wave which is dynamically scattered within the crystal. The electron wave at the exit plane of the specimen is called the exit-wave and contains all structural information about the specimen: both the specimen thickness and the atomic positions. This exit wave function and the structural information that it contains, however, should still be transferred to the CCD camera or other recoding medium by the lenses below the specimen. An ideal situation would be that all the frequencies present in the exit-wave would be transferred equally – preferably with a transfer function of 1 or -1 leaving the exit-wave unchanged. However, the information transfer in the electron microscope is not ideal. The frequencies present in the exit-wave are all differently affected by the transfer process and are therefore not transferred equally. In other words: the recorded image (i.e. the intensity of the electron wave at the image plane) is dependent upon the transfer function of the microscope, and is distorted by the lens aberrations (defocus, spherical aberration, chromatic aberration, astigmatism, coma, etc.) of the image forming lenses – predominantly the objective lens. Owing to this non-ideal transfer of information and the image distortion that follows from it, the one-to-one correspondence between a recorded HRTEM image and the imaged object can get lost.

The TEM result is analyzed using the formula

$$R = \frac{n\,\lambda\,L}{d} \qquad (3.3)$$

where λ is the electron wavelength and L is the distance from the specimen to the aperture screen, *d* is the spacing between the planes in the atomic lattice and R is the radius of the ring [60].

3.3 Magnetic characterization

3.3.1 Vibrating sample magnetometer

Vibrating Sample Magnetometer (VSM) is commonly used research tool to measure the magnetic properties of materials. Figure 3.3 shows the main component of the VSM used. Magnetic sample on the tip of a mechanically vibrated rod is placed between the poles of an electromagnet. If the sample is vibrated vertically at a constant frequency and amplitude it induces an electrical signal in pick-up coils which is proportional to its magnetic moment. The constancy of vibration amplitude and frequency is compared with a known sample in the vibrating head. The signal in the pick-up coils is then converted to magnetic moment through the electronics of the magnetometer. Magnet moment sensitivity in VSM is up to 1 μemu.

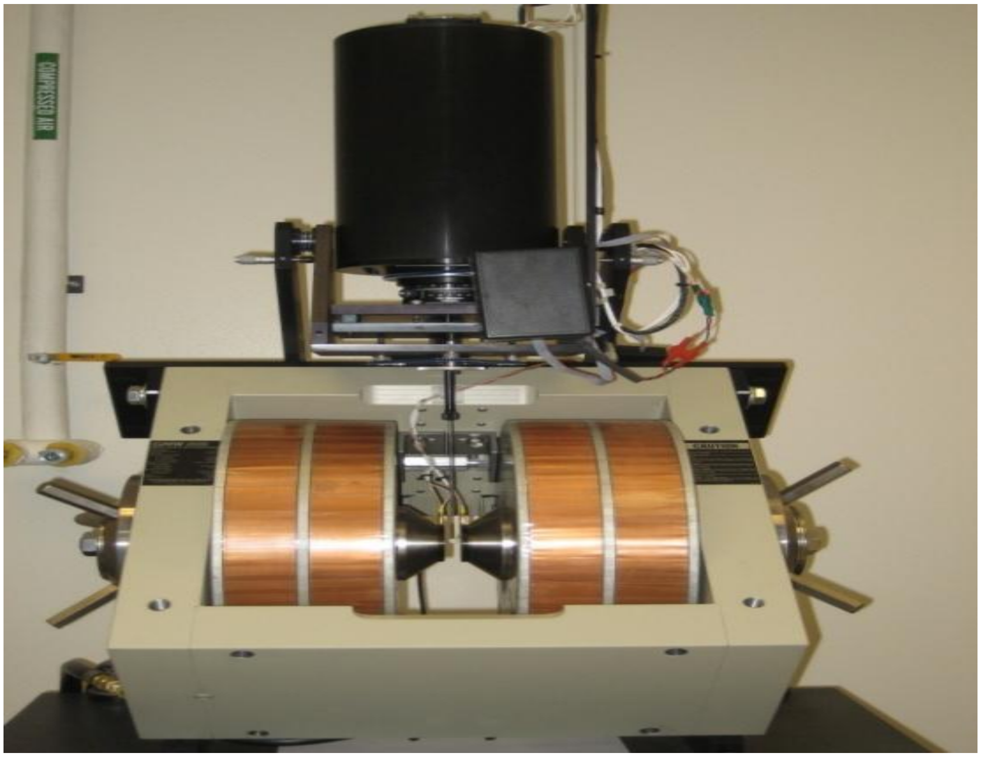

Figure 3.3 Vibrating sample magnetometer used in the experiment.

3.3.2 Superconducting quantum interference device magnetometer

Superconducting Quantum Interference Device Magnetometer (SQUID) uses a superconducting magnet, through which a large amount of current can flow so that large magnetic field can be generated. The magnetic measuring mechanism of SQUID belongs to an inductive technique. During magnetic moment measurement, the sample moves through a system of superconducting detecting coils and the magnetic moment of the sample causes a change in magnetic flux associated with the detecting coils, resulting in electric current produced in the detecting coils. The detecting coils are connected to the SQUID sensor, which functions as a highly linear current-to-voltage converter, producing very accurate variations in the output voltage that is proportional to the moment of the sample. The SQUID can generate a magnetic field as high as 70 kOe and can be operated in temperatures from 2 K to 400 K. The sensitivity of SQUID is 10 nemu up to the applied field of 2.5 kOe and 0.6 μemu above that. Liquid helium is required to operate SQUID, which makes the use of it expensive. SQUID magnetometer is shown in Figure 3.4.

Figure 3.4 Quantum design SQUID magnetometer.

3.4 Spectroscopy characterization

3.4.1 Raman spectroscopy

Raman spectroscopy is a technique based on the scattering of monochromatic light, usually from a laser. Inelastic scattering is when the frequency of photons in monochromatic light changes upon interaction with a sample. The photons of the laser light are absorbed by the sample and subsequently reemitted. The frequency of the reemitted photons is shifted up or down in comparison with the original monochromatic frequency, which is known as the Raman effect**.** The Raman shift provides information about vibrational, rotational, and other molecular modes. Raman spectroscopy can be used to study solid, liquid, and gaseous samples.

The Raman effect is based on molecular deformations in electric field E determined by molecular polarizability α. The laser beam can be considered as an oscillating electromagnetic wave with electrical vector E. Upon interaction with the sample, it induces electric dipole moment P = α E, which deforms molecules. Periodical deformation molecules begin vibrating with characteristic frequency ν_m. The amplitude of vibration is known as nuclear displacement. In other words, monochromatic laser light with frequency $v_0$excites molecules and transforms them into oscillating dipoles. Such oscillating dipoles emit light of the following three frequencies shown in Figure 3.5

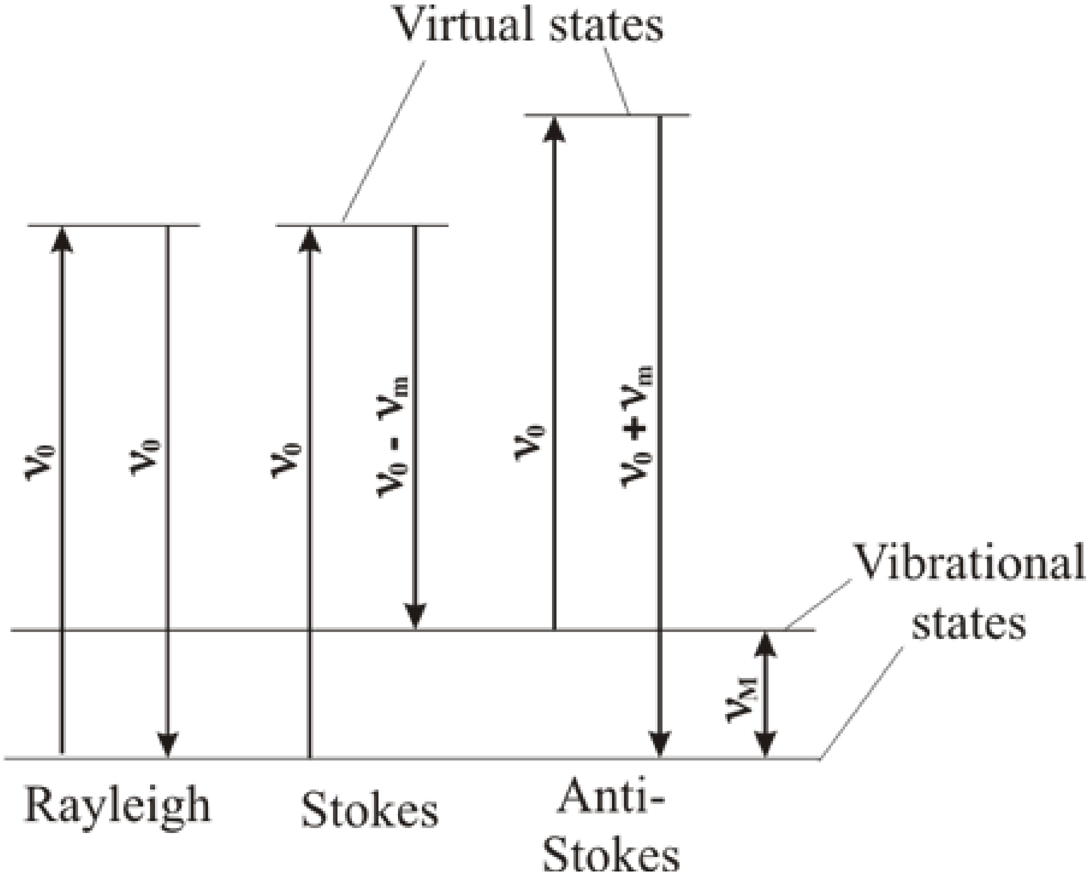

Figure 3.5 Raman transitional schemes.

Elastic Rayleigh scattering: A molecule with no Raman-active modes absorbs a photon with the frequency v_0. The excited molecule returns back to the same basic vibrational state and emits light with the same frequency v_0 as an excitation source.

Stokes frequency: A photon with frequency v_0 is absorbed by a Raman-active molecule which at the time of interaction is in the basic vibrational state. Part of the photon's energy is transferred to the Raman-active mode with frequency v_m and the resulting frequency of scattered light is reduced to $v_0 – v_m$.

Anti-Stokes frequency: A photon with frequency v_0 is absorbed by a Raman-active molecule which at the time of interaction is already in the excited vibrational state. The excessive energy of an excited Raman-active mode is released, molecule returns to the basic vibrational state and the resulting frequency of scattered light rises to $v_0 + v_m$.

About 99.999% of all incident photons in spontaneous Raman undergo elastic Rayleigh scattering. This type of signal is useless for practical purposes of molecular characterization. Only about 0.001% of the incident light produces inelastic Raman signal with frequencies $v_0 \pm v_{m.}$ Spontaneous Raman scattering is very weak and special measures should be taken to distinguish it from the predominant Rayleigh scattering. Instruments such as notch filters, tunable filters, laser stop apertures, and double and triple spectrometric systems are used to reduce Rayleigh scattering for obtaining high-quality Raman spectra.

Raman analysis was performed on the samples using a ThermoFisher Scientific DXR Raman in a backscattering mode with He-Ne laser at 633 nm excitation wavelength. Samples were prepared by depositing the nanoparticles dispersion on (1x1) inch glass substrates and drying the organic solvent in air. Raman spectroscopy, a molecular spectroscopy which is observed as inelastically scattered light, allows for the identification of vibrational (phonon) states of molecules. As a result, Raman spectroscopy provides an invaluable analytical tool for molecular finger printing as well as monitoring changes in molecular bond structure (e.g. state changes and stresses & strains).

3.4.2 Fourier transform infrared spectroscopy

Fourier transform infrared spectroscopy (FTIR) is one of the most common spectroscopic techniques to characterize molecular compounds. When the sample is irradiated with infrared frequencies, it absorbs radiation causing the chemical bonds in the sample to vibrate. Functional groups absorb infrared radiation at a specific wavenumber regardless of the structure of the molecule. The presence of different functional groups can be identified by looking at the different absorption peak in the infrared spectrum.

Michelson interferometer is the main component in FTIR spectroscopy as shown in Figure 3-6 [61]. The interferometer is composed of a moving mirror, a fixed mirror, and a beam splitter. The beam splitter can divide the incoming infrared radiation into two beams. The beam splitter transmits one-half of the beam and reflects the other half. The two split beams strike two mirrors; one of which is fixed and the other is movable, and then recombine at the beam splitter after a path difference has been produced. This beam then passes through the sample before reaching the detector. The function of moving mirror is to generate the interference between two reflected beams by changing the distance traveled by one beam. Because of the interference, the intensity of each beam passing to the detector and returning to the source depends on the difference in the path of the beams in the two arms of the interferometer. The variation in the intensity of the beams passing through the detector and returning to the source as a function of the optical path difference gives a spectrum called interferogram. An interferogram is the sum of sinusoidal waves with a range of wavelengths and is converted using Fourier transformation to infrared single spectrum [62].

Fourier transformation is a mathematical tool which transfers information between a function in the time (t) domain and its corresponding frequency (ω) domain and is given as

$$\mathrm{F}(\omega) = (1\sqrt{2\pi}) \int \mathrm{f}(\mathrm{t}) \exp(-\mathrm{i}\omega \mathrm{t})\, \mathrm{dt} \tag{3.4}$$

Fast Fourier transform (FFT) is used to converts the intensity versus path difference spectrum to the intensity versus wavenumber spectrum. It is the spectrum of absorbance or

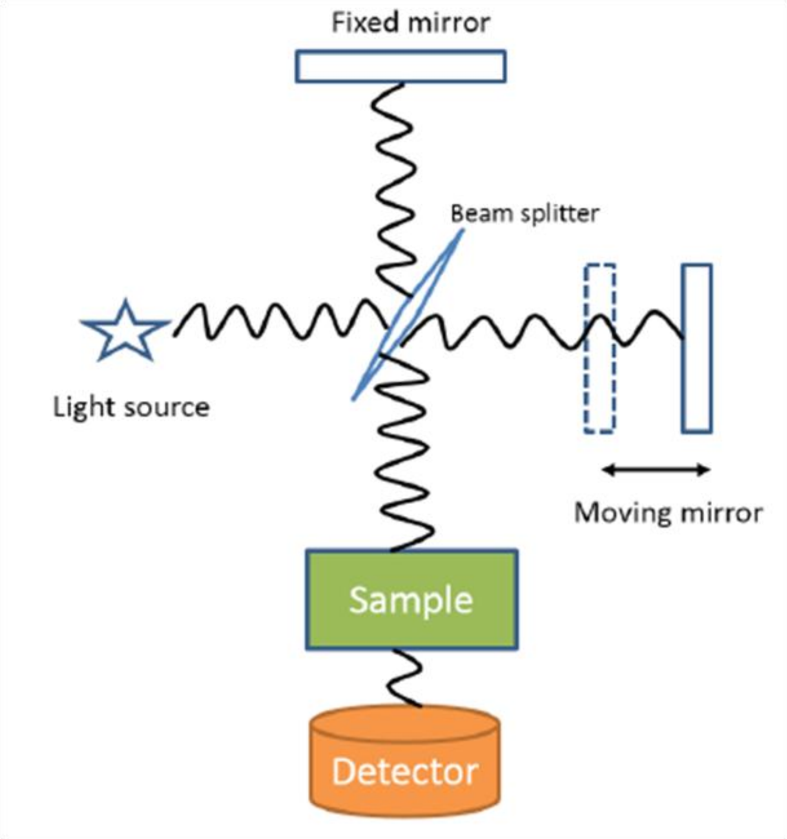

Figure 3.6 Schematic diagram of Michelson interferometer.

transmittance versus wavenumber. It includes both spectra from the sample and the background. The background spectrum is the spectrum obtained without having a sample in the sample holder. This spectrum is from the different parts of the instrument like source, detector, mirror and surrounding environment. To get rid of the signals from the instrument itself and different molecules like water, CO_2 present in the environment, this background spectrum is subtracted from the sample spectrum.

In this work, Thermo Nicolet 6700 FTIR spectrometer is used. This spectrometer is able to collect spectra in the mid-IR, far-IR and near-IR spectral ranges. In this frequency range, absorption peaks due to organic compounds are readily observable [63].

3.4.3 Laser ablation inductively coupled plasma mass spectroscopy

The graphitic sample in powder form can't be dissolved in nitric acid for liquid analyses by ICP-MS (inductively coupled plasma–mass spectrometry), hence the laser ablation (LA)-ICP-MS approach for solid sample analyses was adopted to analyze elements implicated in the magnetic characteristics. The powder was deposited onto a glass slide by droplets of dispersed powder into ethanol, which was subsequently analyzed by LA-ICP-MS.

A UP-213 laser ablation system (New Wave, Freemont, CA), interfaced with a PerkinElmer/SCIEX ELAN DRC II (Sheldon, CT) ICP-MS system, was employed in this study. A 100 µm-diameter laser spot to vaporize a hole in the solid sample at a sub-micron depth for each laser pulse, and the vaporized elements from the hole were entrained by helium gas and analyzed with ICP–MS. This LA–ICP–MS approach can generate 2-D and 3-D maps of chemical distribution on any solid material at a spatial resolution of microns, and a concentration limit of sub-mg/kg.

Chapter 4

Synthesis and characterization of Fe nanoparticles

4.1 Introduction

Magnetic metal nanoparticles exhibit unique properties leading to diverse applications in the areas of magnetic data storage, magnetic fluids, drug delivery, hyperthermia, photothermal therapy and magnetic resonance imaging [64-72]. Carbon-encapsulated magnetic metal nanoparticles, particularly Fe metal nanoparticles may offer novel properties arising from the core–shell structure due to the interfacial interaction between magnetic and dielectric layers [73]. The novel structure of encapsulated Fe phase inside carbon shells can immunize the Fe against environmental degradation effects while retaining their intrinsic magnetic properties [74, 75]. Carbon coatings can thus endow these magnetic nanoparticles with biocompatibility and stability in many organic and inorganic media [76]. It is worth noting that these core-shell nanoparticles are not prone to agglomeration due to the fact that carbon coating layers reduce magnetic interactions [77]. Chemical, magnetic and structural properties of the core-shell nanostructures are preserved for a long time in chemically aggressive surroundings [78]. Therefore, these materials are interesting from both the point of fundamentals of materials science and because of their possible applications.

Various techniques have been developed to synthesize carbon encapsulated metal nanoparticles, which includes standard carbon arc techniques [79], tungsten arc technique [74], combustion (detonation) [80], magnetron and ion-beam co-sputtering [81] and catalytic chemical vapor condensation [82]. However, these methods require expensive vacuum equipment and involve complex processes. High energy consumption and intensive hardware of these techniques are responsible for the high cost of manufacturing carbon-encapsulated nanoparticles and thus limit their practical applications. The main advantage of our new method is that plasma can be generated and maintained at a low voltage in toluene without expensive vacuum equipment and additional chemical process for synthesis. Hence it is cost effective and easy to synthesize nanoparticles using this method.

We present here our studies on the preparation and properties of carbon-coated Fe nanoparticles using a novel method. This work will exclusively discuss the formation of carbon-coated Fe nanoparticles. The effect of thermal annealing on the synthesized core-shell nanoparticles, which are in elemental but not in carbide form, and the structural, as well as magnetic properties of these metal nanoparticles, are discussed. In order to synthesize carbon-encapsulated Fe nanoparticles, toluene was chosen as a carbon source and Fe electrodes are used as a metal source.

4.2 Experimental method

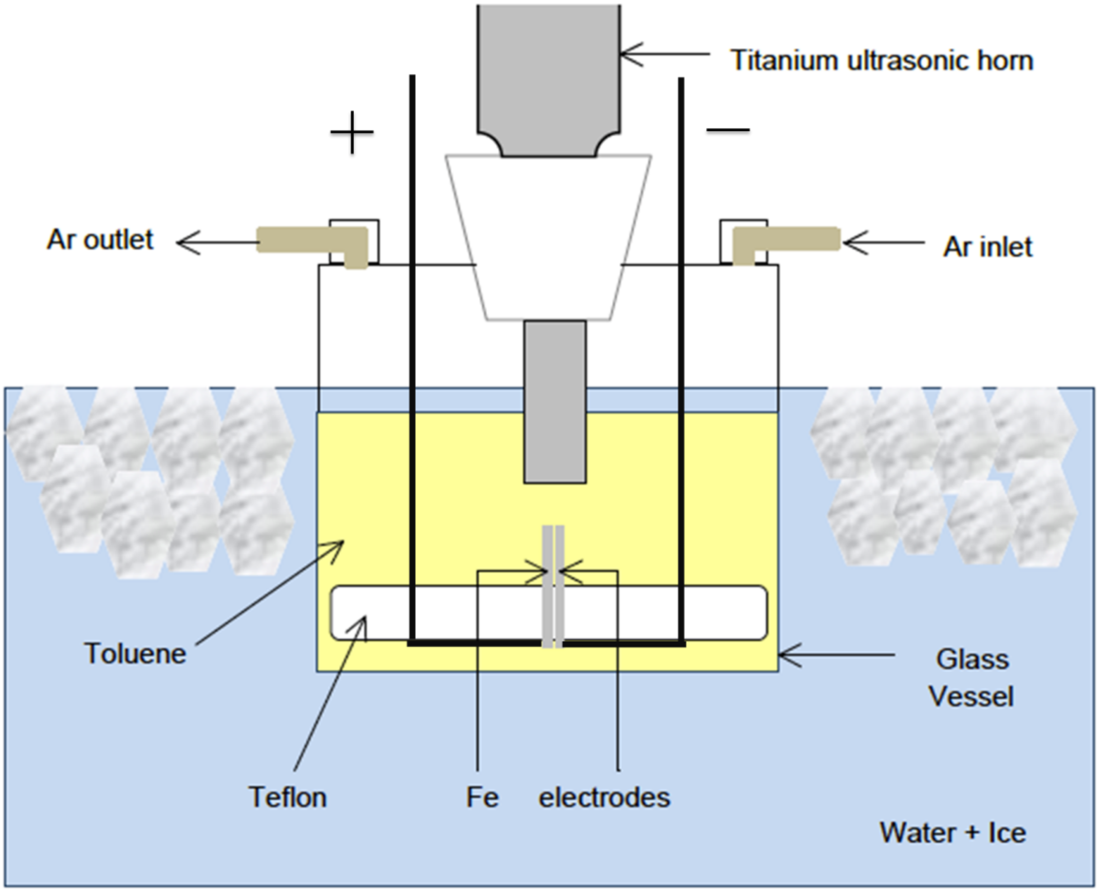

Figure 4.1 Schematic of the experimental set up that is used to synthesize core-shell nanoparticles.

The operational principle of the present method to synthesize nanoparticles using plasma due to ultrasonic cavitation in toluene has been previously demonstrated in detail previously [48]. Figure 4.1 shows a schematic diagram of the experimental apparatus. An ultrasonic processor (Sonics, VCX 750) with a titanium horn 19 mm in diameter was used in the experiment to irradiate 275 ml of toluene (Sigma Aldrich, anhydrous 99.8%) at 750 watts and 20 kHz. A glass vessel filled with ice water was underneath and an Argon gas flow was directed into the closed geometry containing toluene to maintain an inert atmosphere. As shown in Figure 4.1, two Fe electrodes (Alfa Aesar, 1 mm in diameter, 99.99%) were inserted 0.4 mm apart from each other beneath the bottom of the ultrasonic horn. The distance between the electrodes and the bottom of the horn was kept constant at 1 cm. During the ultrasonic irradiation, the voltage on the electrodes was kept at 3.5 kV using a constant voltage power supply.

Ultrasound in liquid media can generate acoustic cavitations, which is the formation and implosive collapse of bubbles. The collapse of such bubbles creates hot spots with temperatures as high as 5000 K and pressures up to 800 atmospheres [56, 83]. These cavitations can produce white noise, sonochemical reactions, erosion of hard materials and sonoluminescence [55]. When cavitations collapse between the Fe electrodes, plasma was generated due to the dissociation of toluene molecules (formation of free radicals and ions) under the applied electric field [84, 85]. Energetic plasma erodes or melts Fe electrodes and then after rapid quenching, stable nanoparticles are formed. However, without ultrasonic irradiation, no plasma was generated with currently used power supply. The plasma was stable during the experiment and hence the positions of the electrodes were fixed throughout the synthesis. During the experiment, which continued for about an hour, nanoparticles were formed and dispersed in the toluene. The liquid turned uniformly black and nanoparticles were condensed and precipitated in the liquid. After 1 hour, nanoparticles were separated by centrifugation from toluene, washed with ethanol and dried in an oven at 318 K. Nanoparticles were dispersed in ethanol, dropped onto a carbon-coated copper grid and dried for the TEM investigation.

The TEM **(**JEOL 1200 EX, operated at 120 kV**)** observations allowed us to determine the overall morphology of the specimen and the structure of the Fe nanoparticles. Fe nanoparticles were also investigated using HRTEM (Hitachi H-9500) operated at 300 kV. The crystal structure of nanoparticle powder was also determined using X-ray diffraction (XRD) with monochromatic Cu K_α radiation (Bruker D8 diffractometer). The chemical composition of the nanoparticles was analyzed using Energy-dispersive X-ray spectroscopy (EDX) linked with the TEM. The magnetic property measurements were carried out using a Vibrating Sample Magnetometer (VSM) by applying a magnetic field of 640 kA/m (Lakeshore, Model-7300). Annealed nanoparticles, which were treated thermally at 500 °C under inert Argon atmosphere for 1 hour, were characterized in the same manner as above.

4.3 Results and discussion

4.3.1 Morphology and structure of synthesized nanoparticles

Nanoparticles size, morphology, chemical composition and crystal structure were investigated using conventional TEM. Particle size and morphology of the synthesized Fe nanoparticles were observed in a bright-field image with low magnification mode. TEM image (Figure 4. 2(a)) shows a broad distribution of darker Fe nanoparticles with several nested layers of carbon encapsulation. The contrast between the Fe core and carbon shell is clearly visible. Selected area electron diffraction (SAED) analysis of Fe nanoparticles is shown in Figure 4. 2(b).The known characteristic lattice (d) spacings of Fe phase permit the unambiguous identification of the encapsulated material. The lattice spacings from the diffraction pattern are 0.203 nm, 0.143 nm, 0.117 nm and 0.101 nm, which corresponds to the reported values of 0.2027 nm (110), 0.1433 nm (200), 0.117 nm (211) and 0.1013 nm (220) for Fe crystal structure (PDF#06-0696). Thus encaged crystals are clearly identified as bcc phase of metallic Fe.

HRTEM (Figure 4. 2(c)) shows that the carbon shells tightly surround the core nanoparticles, no obvious voids can be observed between the core and the shell. The shells are uniform in thickness and consist of 20-22 layers (7-8 nm thick). The spacing of the lattice fringes of carbon shell is about 0.35 nm (Figure 2(d)), which is close to that of the graphite (002) planes.

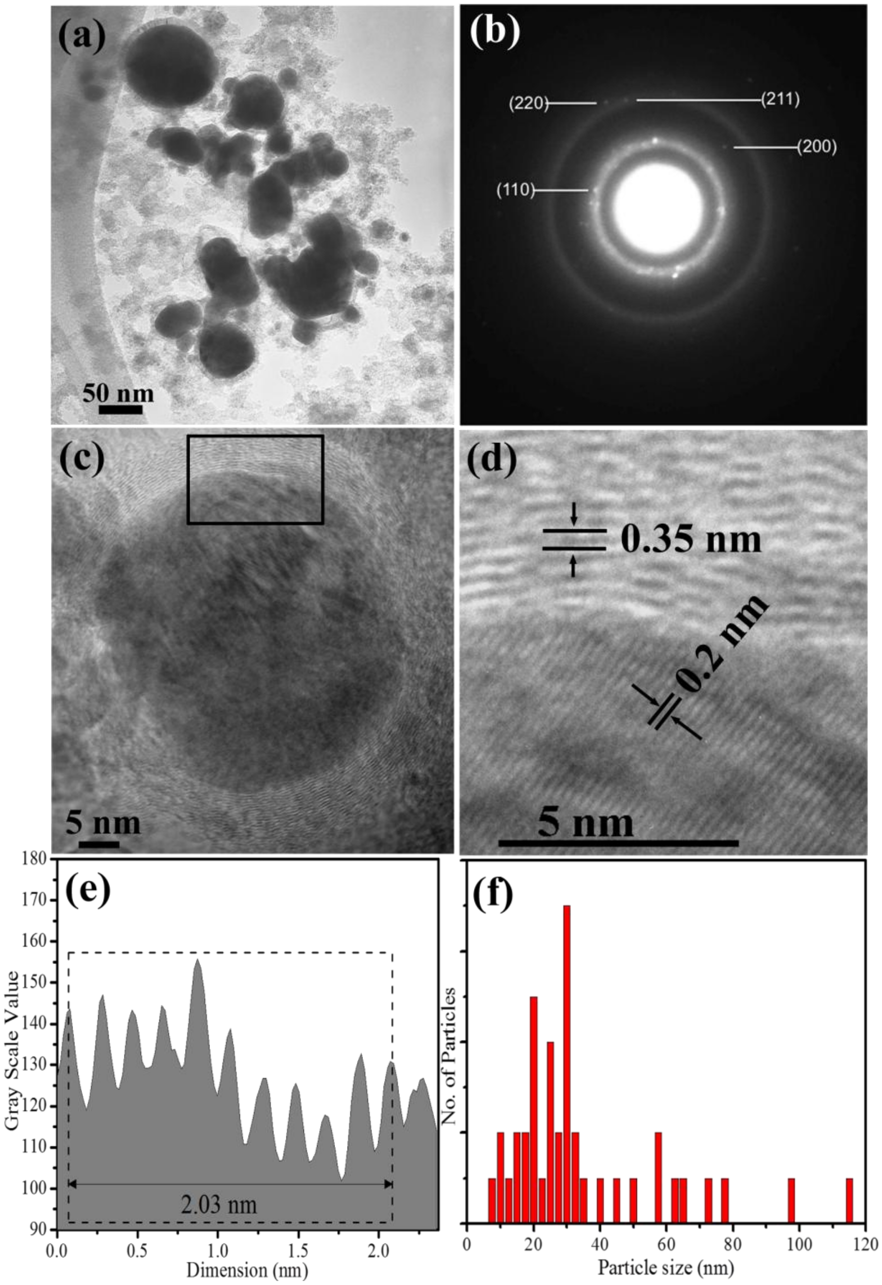

Figure 4.2 (a) TEM image of Fe-C nanoparticles, (b) SAED pattern of Fe-C nanoparticles, (c) HRTEM image of a single Fe-C nanoparticle, (d) Expanded view of the highlighted area in HRTEM image shown in (c). The lattice spacings of Fe core and C shell are clearly measured. (e) The interplanar spacing plot of 12 Fe lattices and (f) Size distribution of Fe-C nanoparticles.

The iron cores have lattice fringe spacing of 0.203nm (Figure 4. 2(d)) related to the (110) plane of the bcc-Fe (PDF#06-0696). Lattice image contrast was processed using ImageJ software.The interplanar spacing of 12 such Fe lattices is shown Figure 4.2(e). The lattice spacing of Fe core is 0.203 nm in agreement with d-spacing of (110) plane of bcc-Fe. The particle size distribution (Figure 4. 2(f)) for the as-prepared sample ranged from 7-115 nm. Elemental compositions of the nanoparticles were analyzed using EDX. The EDX spectra of as-synthesized and annealed nanoparticles are shown in Figure 4.3(a) and Figure 4.3(b) respectively. The EDX spectra (Figure 4.3(a)) exhibited the characteristic peaks associated with Fe and C for the as-synthesized nanoparticles. No characteristic peaks of oxygen were evident. The presence of Cu is due to the TEM grid.

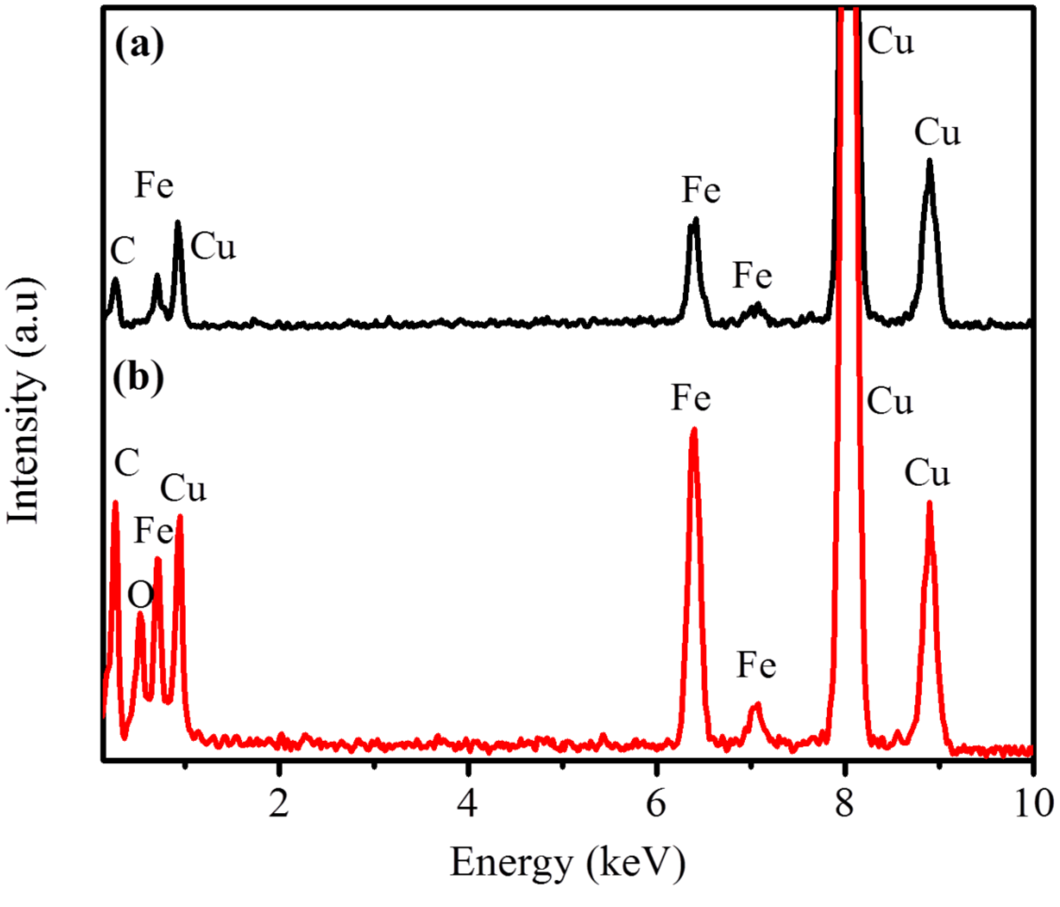

Figure 4.3 (a) EDX spectrum of the synthesized nanoparticles and (b) EDX spectrum of annealed nanoparticles.

XRD pattern of the synthesized nanoparticles is shown in Figure 4.4(a). The poorly crystalline nature of the core-shell nanoparticles is demonstrated by the presence of only one diffraction peak. The peak at a 2θ value of 44.56° corresponds to the (110) plane of Fe.

4.3.2 Morphology and structure of annealed nanoparticles

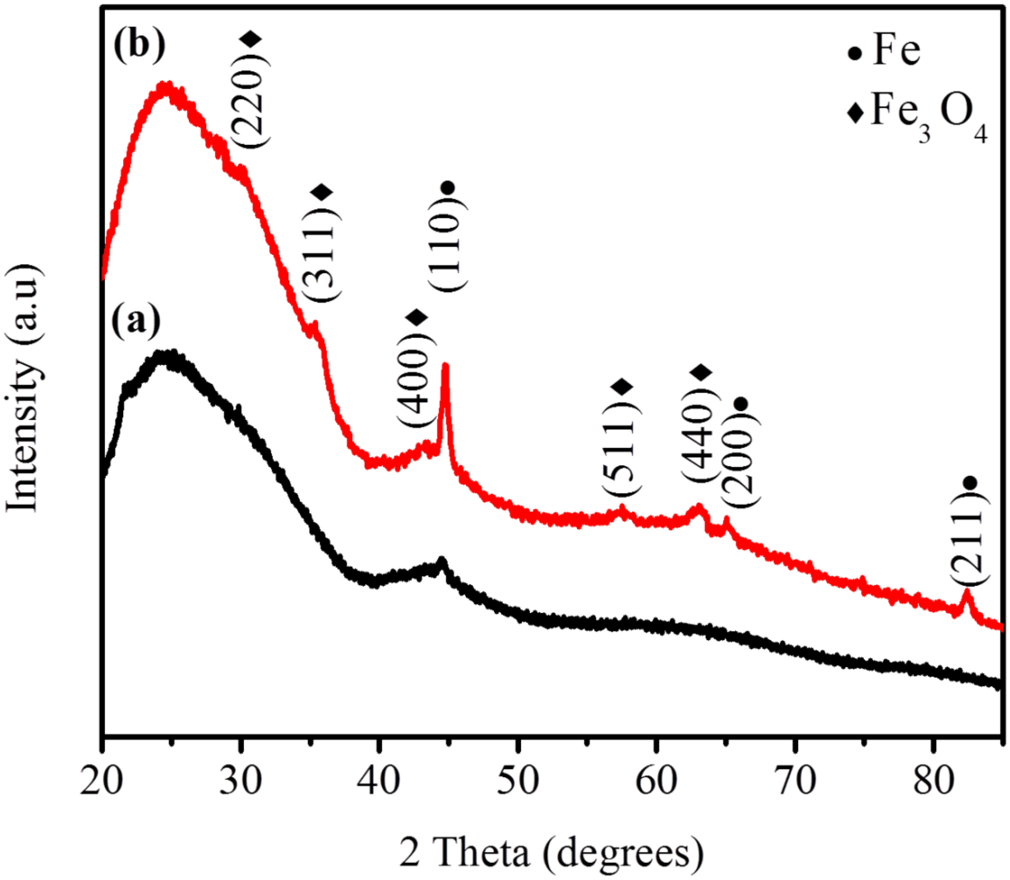

Figure 4.4 (a) XRD pattern of the synthesized nanoparticles and (b) XRD pattern of annealed nanoparticles.

The dark black powder is formed after annealing of the synthesized nanoparticles at 500 °C in an inert Ar atmosphere for 1 hour. The XRD pattern for the annealed nanoparticles shown in Figure 4.4 (b) has a bcc crystal structure of Fe phase (PDF: 06-696). The peaks at 2θ values of 44.7°, 65.01° and 82.41° are assigned as (110), (200) and (211) diffraction lines of bcc Fe phase. The effect of thermal treatment helped to improve the crystallinity of Fe phase as evident by the increase in number of Fe peaks compared to one peak in as-synthesized nanoparticles. In addition, small peaks were observed which corresponds to Fe_3O_4 phase. The peaks at 2θ values of 30.04°, 35.57°, 43.26°, 57.48° and 63.1° are assigned as (220), (311), (400), (511) and (440) diffraction lines of Fe_3O_4 phase (PDF#01-071-6337). The broad peak at a 2θ value of 24.47° is due to the glass substrate used for XRD measurement. The effect of annealing on the synthesized nanoparticles does not result in iron carbide formation but retains its elemental form [73, 86].

TEM image (Figure 4.5 (a)) of the annealed sample shows that Fe core nanoparticles are still encapsulated by carbon shells. The Fe crystal boundary lies to the interior of carbon shell, which confirms that the nanoparticles are completely enclosed within the carbon shells. Post-synthesis thermal treatment at 500 °C has lead to an increase in nanoparticles size. Several smaller nanoparticles may have heat-induced defects such as gaps and cracks that resulted from the shrinkage and rearrangement of carbon layers. These would possibly become the migration channel for Fe [87-89]. The nanoparticles became larger by coalescence of smaller nanoparticles due to the tendency of the system to decrease its surface energy. Such a decrease is possible only by reducing the total surface of the nanoparticles by sintering of small nanoparticles into larger ones [86]. These gaps and cracks resulted from the heat treatment due to annealing process would possibly become the migration channel for oxygen after annealing. Since Fe is very reactive to oxygen, Fe_3O_4 is formed. Fe nanoparticles with a diameter of 110-165 nm and shell thickness of 11-18 nm were formed (Figure 4.5(a) and Figure 4.5(b)). In addition to increasing particle size, we also observed the change in shape of particles. We observed nanocapsules with a diameter of 105-165 nm, length in the range of 215-435 nm and shell thickness of 30-50 nm (Figure 4.5(b)). Metal nanoparticles, particularly transition metal elements (Fe, Co, and Ni) are used as catalysts for graphitization. The increase in the size of Fe catalyst leads to increase in graphitization and hence the shell thickness increases after annealing [90-92].

SAED pattern of Fe nanoparticles is shown in Figure 4.5 (c). The lattice spacings from the diffraction pattern are 0.203 nm, 0.143 nm, and 0.117 nm, which correspond to the reported values of 0.2027 nm (110), 0.1433 nm (200), and 0.1170 nm (211) for Fe crystal structure. The

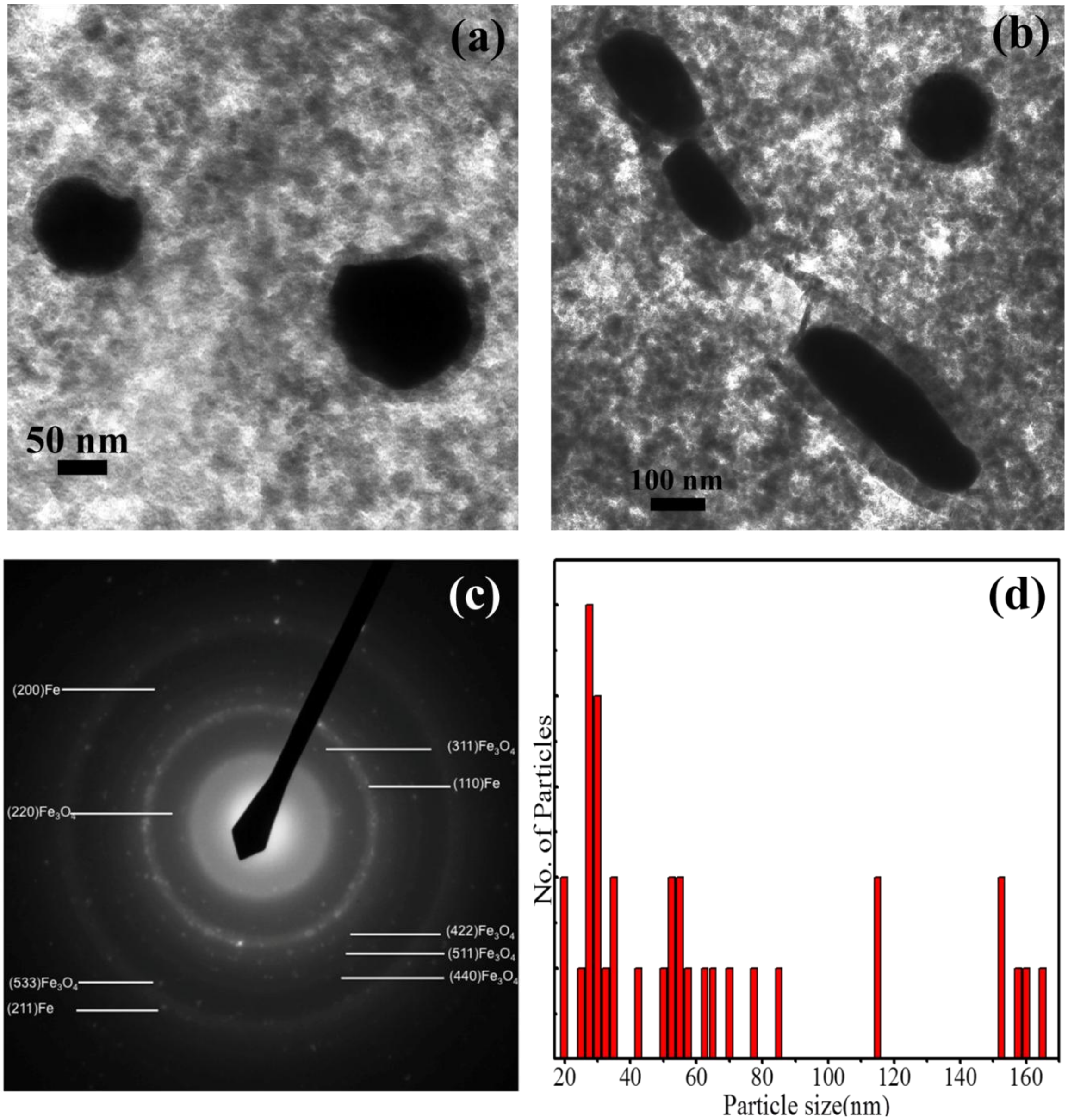

Figure 4.5 (a) TEM image of Fe-C annealed nanoparticles, (b) TEM image of Fe-C annealed nanoparticles and nanocapsules, (c) SAED pattern of annealed Fe-C nanoparticles and (d) Size distribution of annealed Fe-C nanoparticles.

other lattice spacings from the diffraction pattern 0.295 nm, 0.252 nm, 0.170 nm, 0.161 nm, 0.148 nm and 0.127 nm correspond to the reported values for (220), (311), (422), (511), (440) and (533) of Fe_3O_4 phase. Spherical nanoparticle size distribution (Figure 5(d)) for the annealed sample ranged from 20-165 nm. The EDX spectra (not shown) of core-shell nanoparticles (Figure 4.5(a)) exhibited the characteristic peaks associated with Fe and C. No characteristic peaks of oxygen were evident. However, EDX spectra (Figure 4.3(b)) of nanoparticles taken at some areas exhibited the characteristic peaks associated with Fe, C, and O. Nanoparticles only partially coated by carbon were not protected and hence the presence of O.

4.3.3 Magnetic properties

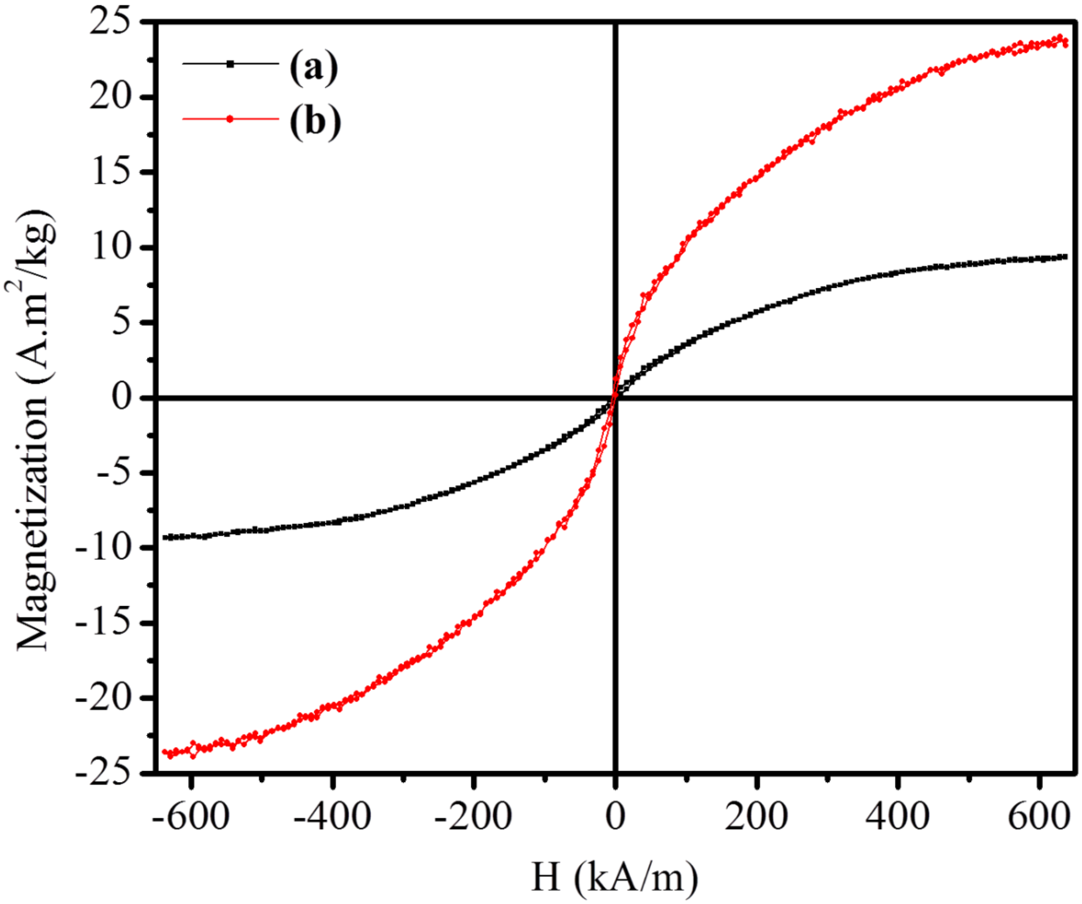

Figure 4.6 (a) Magnetic hysteresis loop of the synthesized nanoparticles and (b) Magnetic hysteresis loop of annealed nanoparticles.

Figure 4.6(a) and Figure 4.6(b) shows a magnetic hysteresis loop for the synthesized and annealed nanoparticles respectively. Magnetic properties were measured at room temperature using VSM by applying a magnetic field in the range from -640 to +640 kA/m. The nanoparticles were ferromagnetic with a low ratio of remanence to saturation magnetization (M_r/M_s) of 0.02 for the synthesized nanoparticles and 0.03 for the annealed nanoparticles. The saturation magnetization (M_s) for the synthesized and annealed nanoparticles is 9 and 24 $A.m^2/kg$ respectively. The coercive force (H_c) for the synthesized and annealed nanoparticles is 4.22 and 3.98 kA/m respectively. M_s and H_c of Fe_3O_4 nanoparticles are 85 $A.m^2/kg$ and 4.93 kA/m. M_s and H_c of bulk Fe is 218 $A.m^2/kg$ and 0.08 kA/m. Fe is a soft magnetic material and hence it is reasonable to compare M_s of synthesized and annealed nanoparticles to bulk Fe and Fe_3O_4. The deviation of the magnetic properties of the synthesized and annealed nanoparticles from those of the Fe_3O_4 and bulk Fe [93, 94] is due to the proportion of nonmagnetic phase (carbon). It has a detrimental effect on the saturation magnetization per unit mass of the synthesized and annealed nanoparticles.

4.4 Fe core – Carbon shell nanoparticles as MRI contrast agent

4.4.1 MRI introduction

Nanocrystals with enhanced magnetic properties have been actively pursued for potential biomedical applications such as drug delivery [95, 96], hyperthermia therapy [97], magnetic resonance imaging (MRI) contrast enhancement [98-106] as well as nanotechnology applications such as catalysis and permanent magnets [9, 14]. In order to use these nanoparticles for in vivo or in vitro biomedical applications such as MRI contrast enhancement, the combined properties of high magnetic saturation, stability, biocompatibility, and interactive functions at the surface are essentially required. Currently, Iron oxide nanoparticles (IONPs) with various microstructure and magnetic properties have been extensively studied for use in MRI [107, 108]. Preparation strategies of surface functionalized and core-shell IONPs are limited by the significant number of synthetic steps involved leading to multi-step complexity [109, 110].

In comparison to IONPs, Iron (Fe) has superior magnetic properties such as high saturation magnetization, roughly double than most of the iron oxides and lower coercivity than IONPs. Hence, Fe nanocrystals will have a much stronger shortening effect on spin-spin transverse relaxation time (T_2) than IONPs, suggesting that Fe nanoparticles may be a more effective contrast enhancer for MRI. The higher magnetization of Fe than IONPs will also ensure accurate dosage due to increase interactions with applied magnetic field [111]. However, it has yet to be explored owing to the problems of easy oxidation and potential toxicity. Although to date most studies have focused on the development of polymer or silica protective coatings, recently carbon-protected magnetic nanoparticles are receiving more attention [110, 112]. Carbon coating provides an effective oxidation barrier, prevents corrosion in magnetic core and mitigates particle attraction, thereby avoiding agglomeration [113]. Fe core coated C shell can thus endow these magnetic nanoparticles with biocompatibility, and higher chemical and thermal stability in many organic and inorganic media compared to bare Fe or IONPs [76, 112].

In this paper, we present a one-step versatile approach to synthesize Fe core coated C shell nanoparticles using plasma and its characterization. Biocompatible and stable multifunctional core-shell nanoparticles were explored by characterizing the magnetic properties of Fe core for contrast enhancement in MRI. Spin-spin transverse relaxation time (T_2) of hydrogen proton in aqueous solution (water) of C coated Fe nanoparticles were evaluated as a contrast agent in MRI. The experimental observations suggest that the C coated Fe nanoparticles are superior T_2 contrast agent with an enhanced relaxivity of 70 $mM^{-1}S^{-1}$.

4.4.2 MRI relaxometry

MRI was conducted using a 7-Tesla small animal MRI system (Varian Inc., Palo Alto, CA) with a 40 mm radio frequency coil and a 400 mT/m gradient coil set. Fe-C nanoparticles 1 mg/ml concentration was diluted in deionized water in a tube (10 mL). Phantoms of different Fe-C nanoparticle concentrations were prepared from stock solution. A multi-echo spin echo sequence was performed for T_2 measurements. Using a repetition time (TR) of 4000 msec, the echo time (TE) was increased in 15 equal steps from 8.45 msec to 135.2 msec.

4.4.3 MRI results and discussion

Nanoparticles size, morphology, chemical composition and crystal structure were investigated using conventional TEM. Bright field TEM image (Figure 7(a)) shows spherical dark

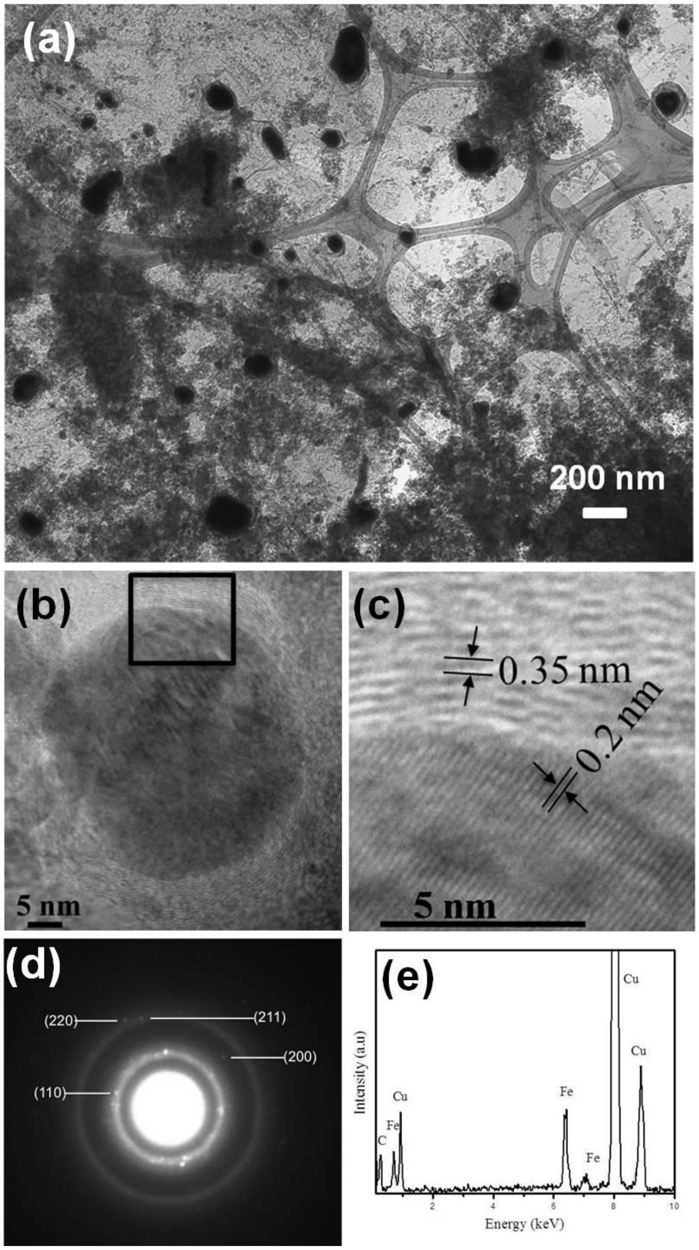

Figure 4.7 (a) TEM image of Fe-C nanoparticles, (b) HRTEM image of a single Fe-C nanoparticle, (c) Expanded view of the highlighted area in HRTEM image shown in (b), (d) SAED pattern of Fe-C nanoparticles, and (e) EDX spectrum of the nanoparticles.

Fe nanoparticles with several layers of C shell. Although the nanoparticle diameters ranged from 10 nm to as large as 85 nm, particles smaller than 25 nm occurred most frequently. In fact, nanoparticles smaller than 20 nm in diameter constituted by far the majority, about 95% of the total. It is clearly visible that core - shell nanoparticles endow better stability and dispersibility and hence it prevents agglomeration. HRTEM (Figure 4.7(b)) shows one such particle with Fe core encapsulated by C shells. The shells are uniform in thickness and consist of 20-22 layers (7-8 nm thick). The spacing of the lattice fringes of C shell is about 0.35 nm (Figure 4.7(c)), which is close to that of the graphite (002) planes. The Fe cores have lattice fringe spacing of 0.203nm (Figure 2(c)) related to the (110) plane of the bcc-Fe (PDF#06-0696). The number of covering layers depended on the particle size; small particles less than 20 nm in diameter were covered by three to four layers, whereas large particles 300 nm in diameter had about 40-60 layers of C encaging them.

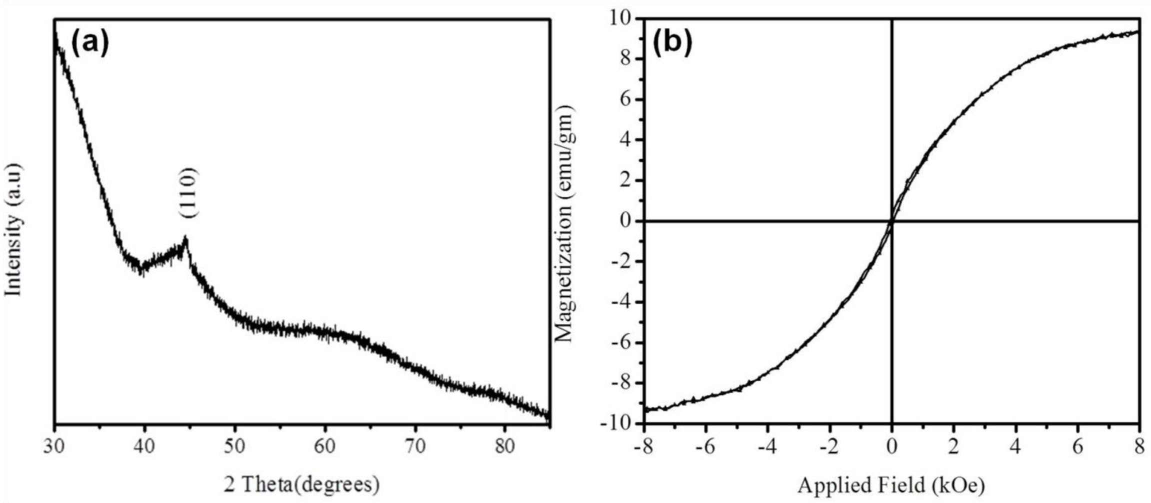

Figure 4.8 (a) XRD pattern of the nanoparticles and (b) Magnetic hysteresis loop of the nanoparticles.

We identified a crystalline Fe core by selected area electron diffraction (SAED) analysis shown in Figure 4.7(d). The known characteristic lattice (d) spacings of Fe phase permit the unambiguous identification of the encapsulated material. The lattice spacings from the SAED pattern are 0.203 nm, 0.143 nm, 0.117 nm and 0.101 nm, which corresponds to the reported values of 0.2027 nm (110), 0.1433 nm (200), 0.117 nm (211) and 0.1013 nm (220) for Fe crystal structure (PDF#06-0696) respectively. Thus encaged crystals are clearly identified as bcc phase of metallic Fe. Elemental compositions of the nanoparticles were analyzed using EDX. The EDX spectra of nanoparticles exhibited the characteristic peaks associated with Fe and C is shown in Figure 4.7(e). No characteristic peaks of oxygen were evident. The presence of Cu is due to the TEM grid.

XRD pattern of the nanoparticles is shown in Figure 4.8(a). The poorly crystalline nature of the core-shell nanoparticles is demonstrated by the presence of only one diffraction peak. The peak at a 2θ value of 44.56° corresponds to the (110) lattice planes of bcc Fe. Figure 4.8(b) shows a magnetic hysteresis loop for the synthesized nanoparticles. Magnetic properties were measured at room temperature using VSM by applying an external magnetic field in the -8 to +8 kOe range. The nanoparticles were ferromagnetic with a low ratio of remanence to saturation magnetization (M_r/M_s) of 0.02. The saturation magnetization (M_s) for the nanoparticle is 9 emu/gm. The coercive force (H_c) for the nanoparticles is 53 Oe, one order higher than bulk Fe. The deviation of the magnetic properties of the nanoparticles from those of the bulk Fe [94] is due to the proportion of nonmagnetic phase (carbon) and poor crystalline nature of nanoparticles.

The transverse *(T_2)* relaxation times of protons in water solutions of Fe-C nanoparticles were measured using a 7 T small animal MRI system. Phantoms of Fe-C nanoparticles of different concentration were prepared from stock solution. To measure T_2, a multi-echo spin echo sequence was used with repetition time (TR) of 4000 msec. The echo time (TE) was increased in 15 equal steps from 8.45 msec to 135.2 msec as shown in Figure 4.9 (a). MRI images (Figure 4.9(b)) shown here were recorded at different echo time 33.8, 67.6, 101.4 and 135.2 msec. A set of these T_2-weighted multi-echo spin echo images (Figure 4.9 (b)) showed the strong T_2 contrast from Fe-C nanoparticles (dark contrast) in comparison to the H_2O phantom. T_2 of Fe-C

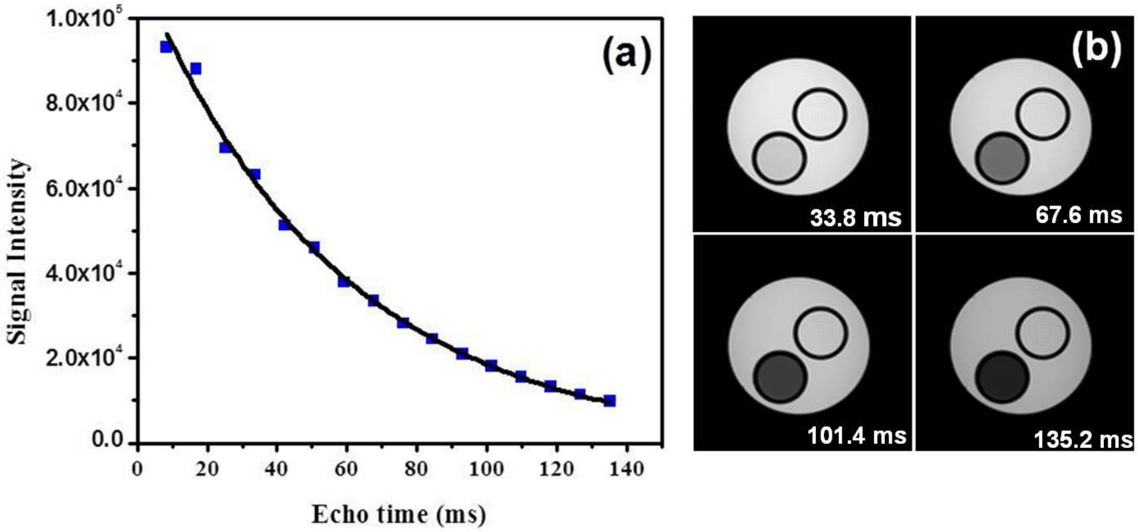

Figure 4.9 (a) MRI signal intensity at different echo times for 0.326 mM concentration, and (b) MR images (shown) are recorded at different echo times 33.8, 67.6, 101.4 and 135.2 msec.

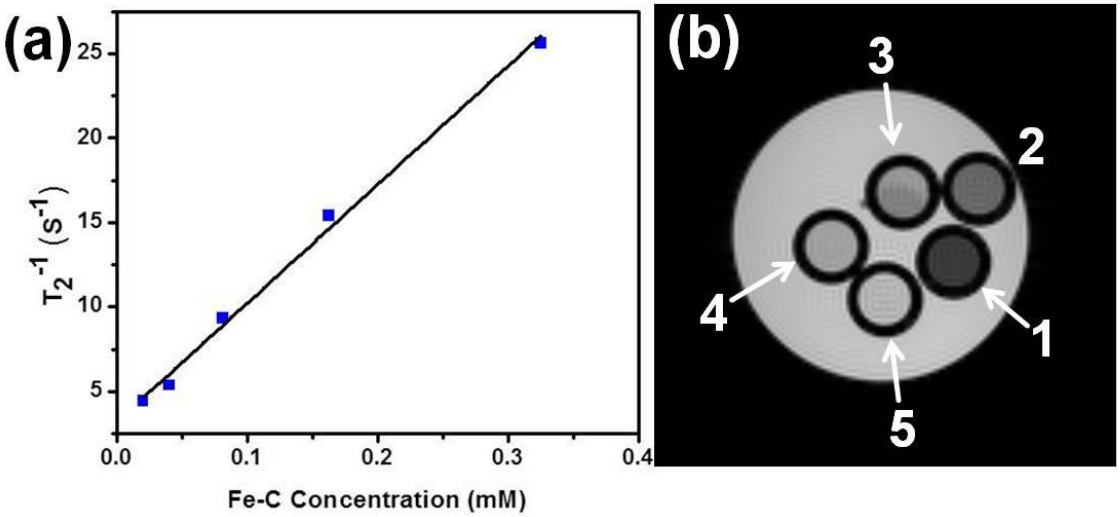

Figure 4.10 (a) T_2^{-1} vs Fe-C nanoparticles concentration, and (b) T_2 weighted spin echo MR images for five concentrations of same samples: 1) 0.326 mM , 2) 0.163 mM, 3) 0.081mm, 4) 0.040 mM , 5) 0.020 mM.

nanoparticles were determined by fitting MRI signal intensities at different echo times using an exponential relation $I = M_0 \, exp^{-TE/T_2}$ (Figure 4.9(a)).

The efficiency of a negative contrast agent in changing the transverse relaxivity of nuclear spins in aqueous solution of magnetic particles is expressed as $\frac{1}{T_2} = \frac{1}{T_{2,O}} + r_2[Fe]$, where $T_{2,0}$ is the relaxation time of the medium in the absence of contrast agent, [Fe] is the concentration of iron, and T_2 is the relaxation time of the medium with contrast agent. The transverse relaxivities (r_2) was calculated from the slope of linear correlation between relaxation rate ($1/T_2$) and concentration of Fe-C NPs (Figure 4.10(a)). The calculated r_2 was 70 $mM^{-1}S^{-1}$. Recent studies of C coated IONPs with average diameter of 90 nm reported a relaxivity of 1.14 $mM^{-1}S^{-1}$ [110]. The high relaxivity about 60 times in our results is attributed to the particle size and Ms of the Fe core. Shortening of the T_2 relaxation time leads to spin dephasing which generates dark contrast as seen in T_2 weighted MRI images (Figure 4.9(b)). Figure 4.10(b) shows the imaging contrast of the samples containing different concentrations. There is a decrease in MRI signal in T_2 weighted images (Figure 4.10(b)) with decrease in Fe concentration. Concentration dependent negative enhancement in contrast is clearly visible. This study demonstrates that biocompatible and stable Fe core - C shell nanoparticles are superior as contrast enhancer in MRI.

4.4 Conclusions

Carbon-encapsulated Fe nanoparticles were synthesized using a new advanced and cost effective method. Fe nanoparticles were synthesized by plasma due to ultrasonication in toluene. The structure and magnetic properties of the synthesized and annealed nanoparticles were studied. TEM and HRTEM images showed Fe as core and carbon as shell. The size of synthesized core-shell Fe nanoparticles could be changed by annealing. SAED and XRD results indicate that all carbon coated metal nanoparticles are elemental rather than metal carbides, which are usually produced by conventional arc or plasma discharge method. The preliminary measurement of the hysteresis loops indicates ferromagnetic properties of these materials. Our cost-effective new method for synthesis of carbon-coated Fe nanoparticles will be of potential interest in MRI and Photothermal cancer therapy applications. This method could also be extended for the synthesis of different carbon coated metal nanoparticles if appropriate electrodes and solvents are selected.

Ferromagnetic core – shell nanoparticles in aqueous dispersion was explored for biological application in MRI contrast enhancement. Fe core – C shell nanoparticles worked as a superior T_2 – weighted contrast agent for MRI with enhanced relaxivity of 70 $mM^{-1}S^{-1}$. In comparison to currently used iron oxides and other metal elements, Fe core nanoparticles can achieve substantially higher relaxivity and hence enhanced MRI contrast. We believe C shell on Fe core improve these magnetic nanoparticles with biocompatibility and stability compared to polymer or silica coating and will open up new possibilities of C coated magnetic nanoparticles for creating next generation MRI contrast agent. Since Fe core – C shell nanoparticles were found to be extremely non-reactive, and highly absorbing in near infrared regime, development of C-based MRI contrast enhancement will allow its simultaneous use in biomedical applications. We aim to localize these nanoparticles in targeted tissue regions by external DC magnetic field, followed by MRI imaging and subsequent photothermal therapy.

Chapter 5

Synthesis and characterization of Ni nanoparticles

5.1 Introduction

Nanoparticles of elemental nickel have been widely studied because of their important magnetic and catalytic properties [114, 115]. Bulk elemental nickel typically adopts the face-centered cubic (fcc) structure, but hexagonal close packed (hcp) and body centered cubic (bcc) allotropes have also been examined both theoretically [116, 117] and experimentally [118, 119]. Nanoparticles of fcc-Ni are common; many reports have described colloidal routes to fcc-Ni with a range of sizes and morphologies [120, 121]. A series of recent reports have suggested that colloidal nanoparticles of the metastable hcp-Ni allotrope are also accessible using the thin films, polyol process and other reactions carried out in high-boiling organic solvents [122-124].

In this chapter, a study on the preparation and properties of carbon-coated Ni nanoparticles using a novel method is presented. This study will exclusively discuss the morphology, structural as well as magnetic properties of these metal nanoparticles. The effect of electrode spacing and hence the change in electric field on above properties will be discussed. In order to synthesize carbon-encapsulated Ni nanoparticles, toluene was chosen as a carbon source and Ni electrodes are used as a metal source.

5.2 Results and discussion

5.2.1 Effect of electrode spacing on structure and magnetic properties

Experiment procedure is similar as used for Fe nanoparticles synthesis, with only changes made are electrode material and spacing between them. Two Ni electrodes (Alfa Aesar, 1 mm in diameter, 99.99%) were inserted 0.3 mm apart for first experiment and 0.6mm for the second experiment. During the ultrasonic irradiation, the voltage on the electrodes was kept at 3.0 kV using a constant voltage power supply.

XRD pattern of the nanoparticles synthesized at 3 kV with 0.3 mm spacing between the two Ni electrodes is shown in Figure 5.1. It has a mixture of hcp Ni and fcc Ni phase. The peaks at 2θ values of 38.68°, 40.50°, 45.76°, 59.86°, and 79.75° are assigned as (100), (002), (101),

(102) and (103) diffraction lines of hcp Ni phase. The peaks at 2θ values of 43.55°, 50.84°, and 74.62° are assigned as (111), (200) and (220) diffraction lines of fcc Ni phase.

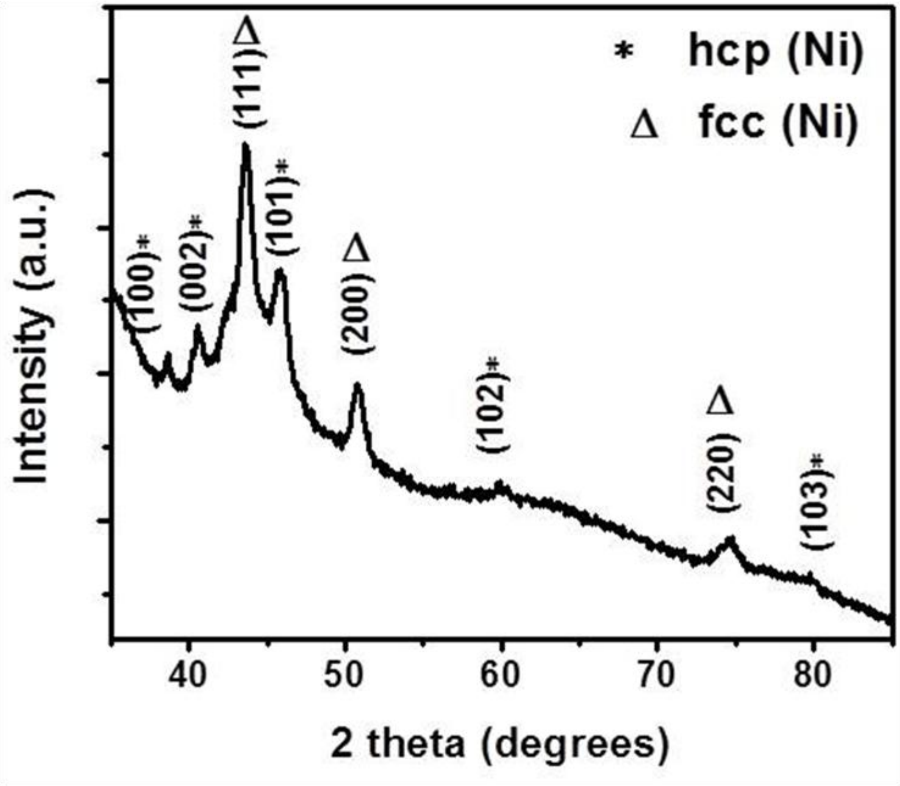

Figure 5.1 XRD pattern of nanoparticles synthesized at 3 kV with 0.3 mm electrode spacing.

XRD pattern of the nanoparticles synthesized at 3 kV with 0.6 mm spacing between the two Ni electrodes is shown in Figure 5.2. It has a predominant fcc Ni phase. The peaks at 2θ values of 43.55° and 50.75° are assigned as (111) and (200) diffraction lines of fcc Ni phase. There is a small minor peak of hcp Ni at 45.8° assigned to (101). The poorly crystalline nature of the nanoparticles is demonstrated by the presence of few diffraction peaks and their low intensity.

It can be understood that when the spacing between two electrodes is changed from 0.3 mm to 0.6 mm, the electric field decreases and hence the energetics of the experiment changes significantly. It appears that with an increase in electrode spacing, the phase changes from (hcp) plus (fcc) to (fcc). The crystallinity of the nanoparticles synthesized also changes from better quality towards amorphization.

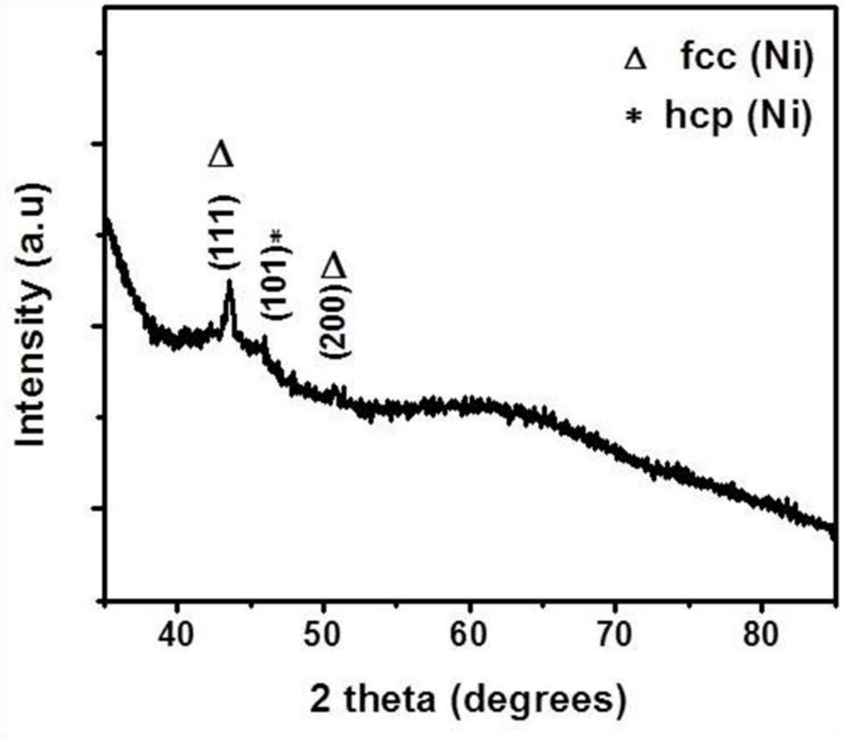

Figure 5.2 XRD pattern of nanoparticles synthesized at 3 kV with 0.6 mm electrode spacing.

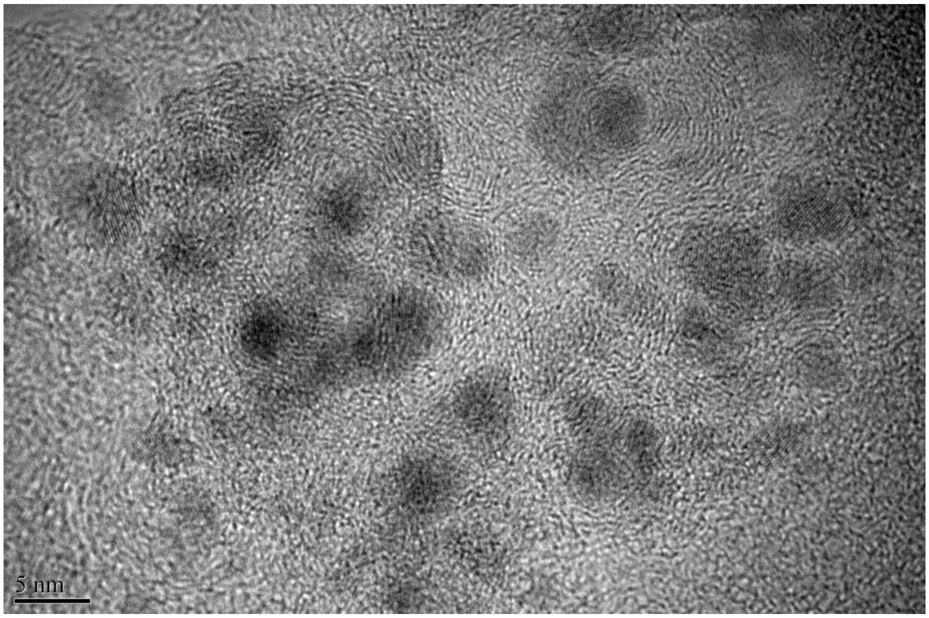

Figure 5.3 HRTEM image of Ni nanoparticles synthesized at 3 kV with electrodes spacing 0.3 mm.

HRTEM image of Ni nanoparticles synthesized at 3 kV with 0.3 mm spacing between the electrodes is shown in Figure 5.3. Narrow size distributions of darker Ni nanoparticles with several nested layers of carbon encapsulation are embedded in carbon matrix (Figure 5.3). The range of Ni nanoparticles is 2-25 nm in diameter, with 95% of particles are less than 10 nm.

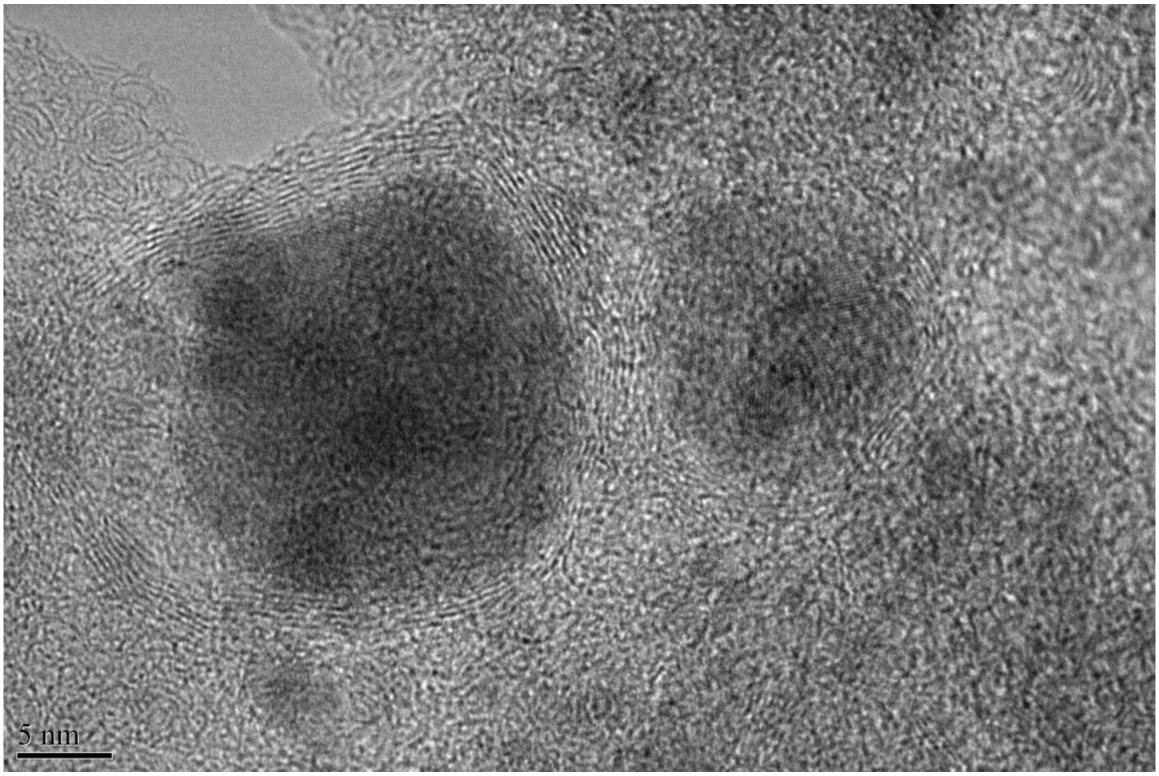

Figure 5.4 HRTEM image showing core-shell nanoparticles of Ni coated by carbon.

HRTEM (Figure 5.4) shows that the carbon shells tightly surround the Ni core nanoparticles. The contrast between the Ni core and carbon shell is clearly visible. The shells are uniform in thickness and consist of 7-8 layers (2.45-2.8 nm thick). The spacing of the lattice fringes of carbon shell is about 0.35 nm, which is close to that of the graphite (002) planes. The Ni cores have lattice fringe spacing of 0.206 nm related to the (111) plane of the fcc-Ni (PDF#071-5653). The known characteristic lattice (d) spacings of Ni phase permit the unambiguous identification of the encapsulated material.

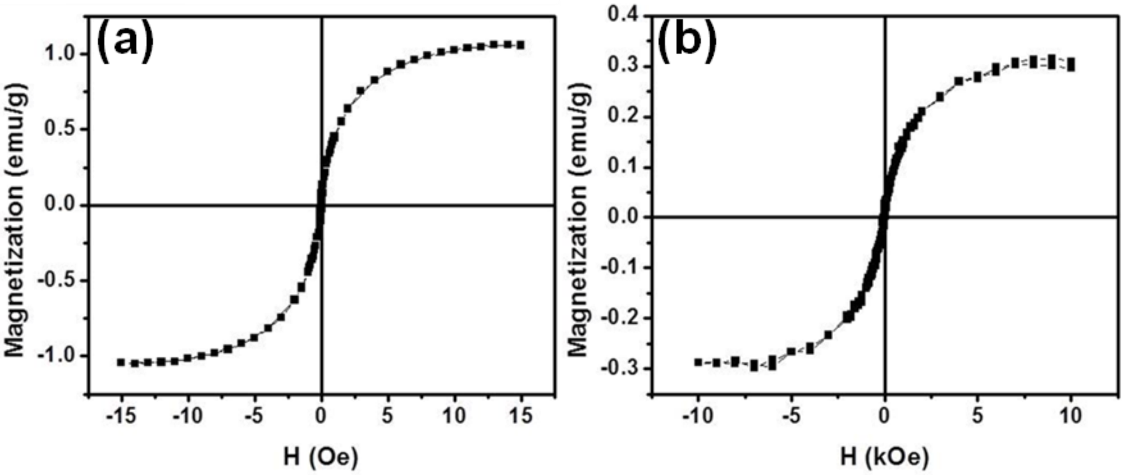

Figure 5.5 Hysteresis loops of nanoparticles synthesized at 3 kV with (a) 0.3 mm and (b) 0.6 mm electrode spacing.

Figure 5.5 (a) and Figure 5.5 (b) shows magnetic hysteresis loops for the synthesized nanoparticles at 3 kV with 0.3 mm and 0.6 mm electrode spacing respectively. Magnetic properties were measured at room temperature using VSM by applying a magnetic field of 15 kOe. The nanoparticles were superparamagnetic since the particle diameter is smaller than the single domain diameter (35 nm) limit of Ni. The saturation magnetization (M_s) for the synthesized nanoparticles at 0.3 mm and 0.6 mm electrode spacing is 1.1 and 0.3 emu/g respectively. Nonmagnetic phase (carbon) and crystalline quality of the material has a detrimental effect on the saturation magnetization per unit mass of the synthesized nanoparticles.

5.3 Conclusions

Carbon-encapsulated Ni nanoparticles were synthesized at different electrode spacing (0.3 mm and 0.6mm) at 3 kV. The structure and magnetic properties of the synthesized were investigated. The crystal structure and crystalline quality of nanoparticle change from hcp and good to fcc and amorphization. HRTEM images showed Ni as core and carbon as shell. The preliminary magnetic measurement of the hysteresis loops indicates superparamagnetic properties of these materials.

Chapter 6

Synthesis and characterization of FeNi nanoparticles

6.1. Introduction

Nickel-based alloys have attracted a great deal of interest because of their technologically important catalytic, optical, and magnetic properties [125-127]. Forming bimetallic solids is a way to tune the material's properties by varying chemical composition and to offer prospects for the design of new functionalities [37]. Among the magnetic material technologically relevant application of nickel-based alloys, nickel-cobalt (Ni-Co), and nickel-iron (Ni-Fe) find a wide range of applications in catalysis and bioscience [7, 13]. For instance, the nanoparticles of FeNi alloys that have been addressed in this work are of particular interest due to their high saturation magnetization, large permeability, low magnetostriction and high anisotropic magnetoresistance. The potential applicability of bimetallic alloys varies widely depending on its magnetic properties which can be tuned by chemical composition, size, and shape.

In this chapter, the structural, morphology and magnetic properties of two different compositions of FeNi nanoparticles is presented. $Fe_{50}Ni_{50}$ and $Fe_{20}Ni_{80}$ nanoparticles were synthesized using a versatile plasma discharge method. For $Fe_{20}Ni_{80}$ composition, the effect of morphology and magnetic property on the type of solvent will be discussed while keeping the same applied voltage. In addition, the effect of magnetic property with varying voltage will be discussed while keeping the same solvent. In order to synthesize carbon-encapsulated $Fe_{20}Ni_{80}$ nanoparticles, ethanol and toluene were chosen as a carbon source and FeNi electrodes with 20:80 composition was used as a metal source.

6.2. Results and discussion

Experiment procedure is similar as used for Fe nanoparticles synthesis. Electrode composition, solvents, and applied voltage between the electrodes are varied. Two FeNi electrodes (20:80 composition) plates 99.99%) were inserted 0.6 mm apart with sharp edges facing each other. During the ultrasonic irradiation, the voltage on the electrodes was set at 3. 5

kV for first set and 4.5kV for the second set of an experiment using a constant voltage power supply. The solvents chosen for experiments were toluene and ethanol.

6.2.1 Effect of solvent on Fe_{20} Ni_{80}

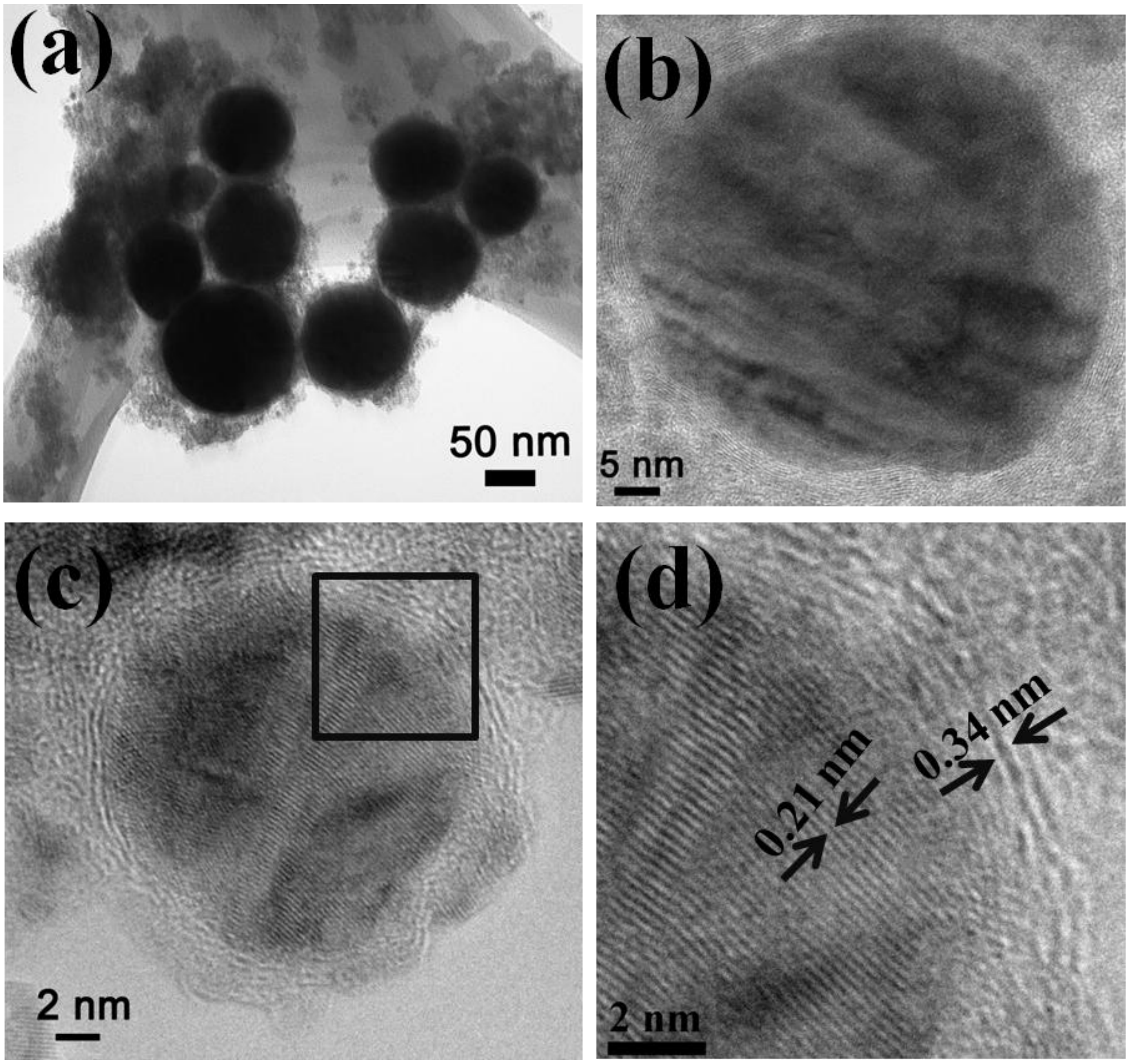

Figure 6.1 (a) TEM image of $Fe_{20}Ni_{80}$ core-C shell nanoparticles synthesized in ethanol at 3.5 kV, (b) HRTEM image of a single FeNi core-C shell nanoparticle with 54 nm diameter and 1 nm shell thickness, (c) HRTEM image of a single FeNi core-C shell nanoparticle with 16 nm diameter and 1 nm shell thickness (d) Expanded view of the highlighted area in HRTEM image shown in (c). The lattice spacings of FeNi core and C shell are clearly measured.

Electron microscopy images of FeNi nanoparticles synthesized in ethanol at 3.5 kV with 0.6 mm spacing between the electrodes is shown in Figure 6.1. Figure 6.1 (a) shows core-shell FeNi nanoparticles with several nested layers of carbon encapsulation. The contrast between the darker FeNi core and lighter carbon shell is clearly visible. The range of FeNi nanoparticles is 15-820 nm in diameter and C shell is 1-34 nm. HRTEM (Figure 6.1 (b)) shows a 54 nm FeNi core nanoparticle with carbon shells of uniform thickness of 2.5 nm tightly surrounding it. HRTEM (Figure 6.1 (c)) shows smaller 16 nm FeNi core nanoparticle with carbon shells of uniform thickness of 1 nm tightly surrounding it. The thickness of shell is dependent upon the particles size since it acts as a catalyst for graphitization. The spacing of the lattice fringes of carbon shells is about 0.35 nm, which is close to that of the graphite (002) planes. The FeNi cores have lattice fringe spacing of 0.208 nm related to the (111) plane of the fcc-FeNi (PDF#071-5653). The known characteristic lattice (d) spacings of FeNi phase permit the unambiguous identification of the encapsulated material.

TEM images of FeNi nanoparticles synthesized in toluene at 3.5 kV with 0.6 mm spacing between the electrodes are shown in Figure 6.2. Figure 6.2 (a) shows core-shell FeNi nanoparticles with several nested layers of carbon encapsulation. The contrast between the darker FeNi core and lighter carbon shell is clearly visible. The range of FeNi nanoparticles is 3-820 nm in diameter and C shell is 1-60 nm. TEM (Figure 6.2 (b)) shows smaller FeNi core - carbon shells nanoparticles. The thickness of shell is dependent upon the particles size since it acts as a catalyst for graphitization. Since toluene is a rich source of carbon in comparison to ethanol the shell thickness is larger for nanoparticles prepared in toluene in comparison to ethanol. The spacing of the lattice fringes of carbon shells is about 0.35 nm, which is close to that of the graphite (002) planes. Elemental compositions of the nanoparticles were analyzed using EDX. The EDX spectra of as-synthesized FeNi nanoparticles are shown in Figure 6.3 (c). The EDX spectra (Figure 6.3(a)) exhibited the characteristic peaks associated with Fe, Ni, and C for the as-synthesized nanoparticles. The presence of Cu is due to the TEM grid. It retains the weight composition of FeNi approximately 20:80.

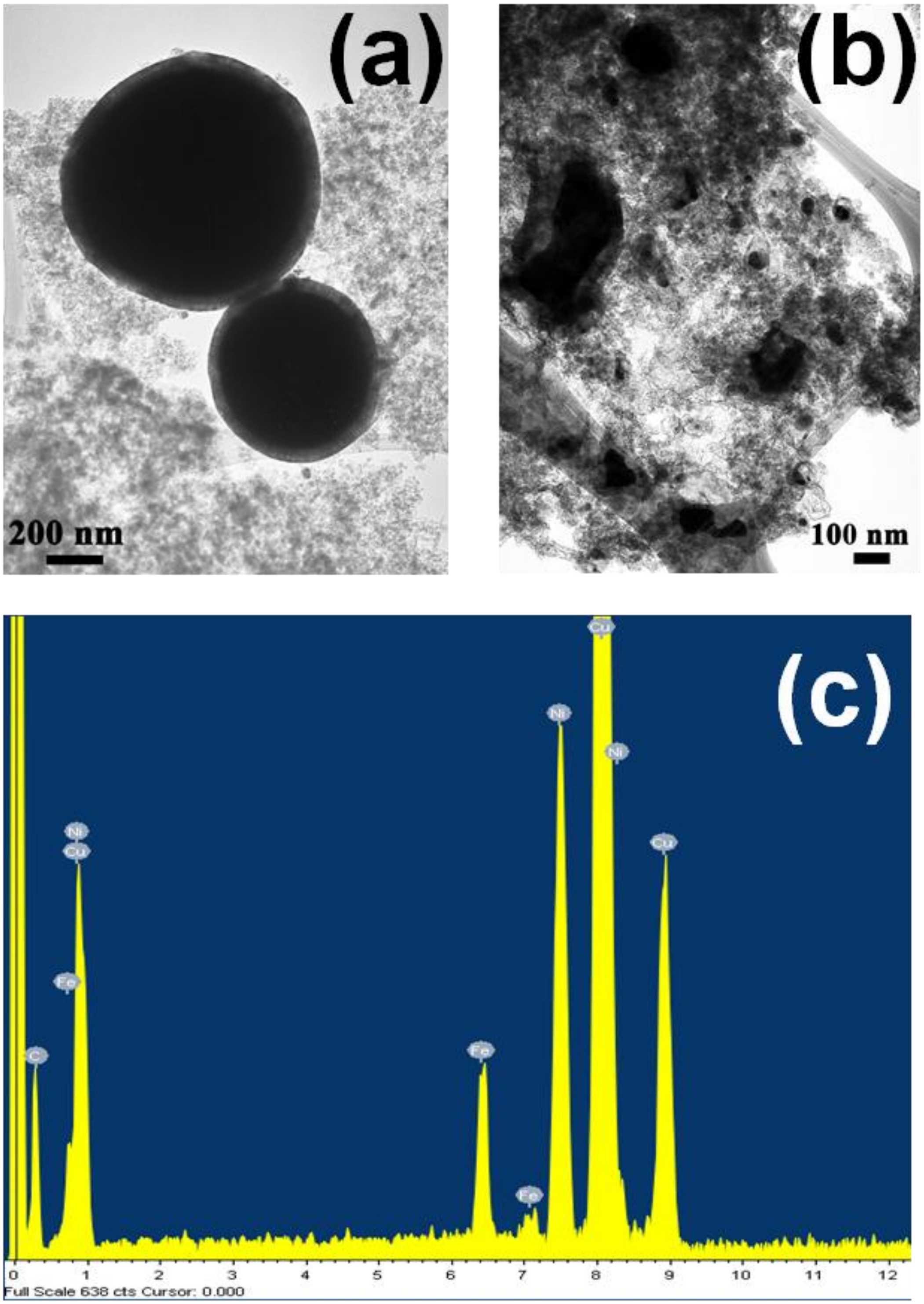

Figure 6.2 (a), (b) TEM image of $Fe_{20}Ni_{80}$ core-C shell nanoparticles synthesized in toluene at 3.5 kV, and (c) EDX spectrum of synthesized nanoparticles.

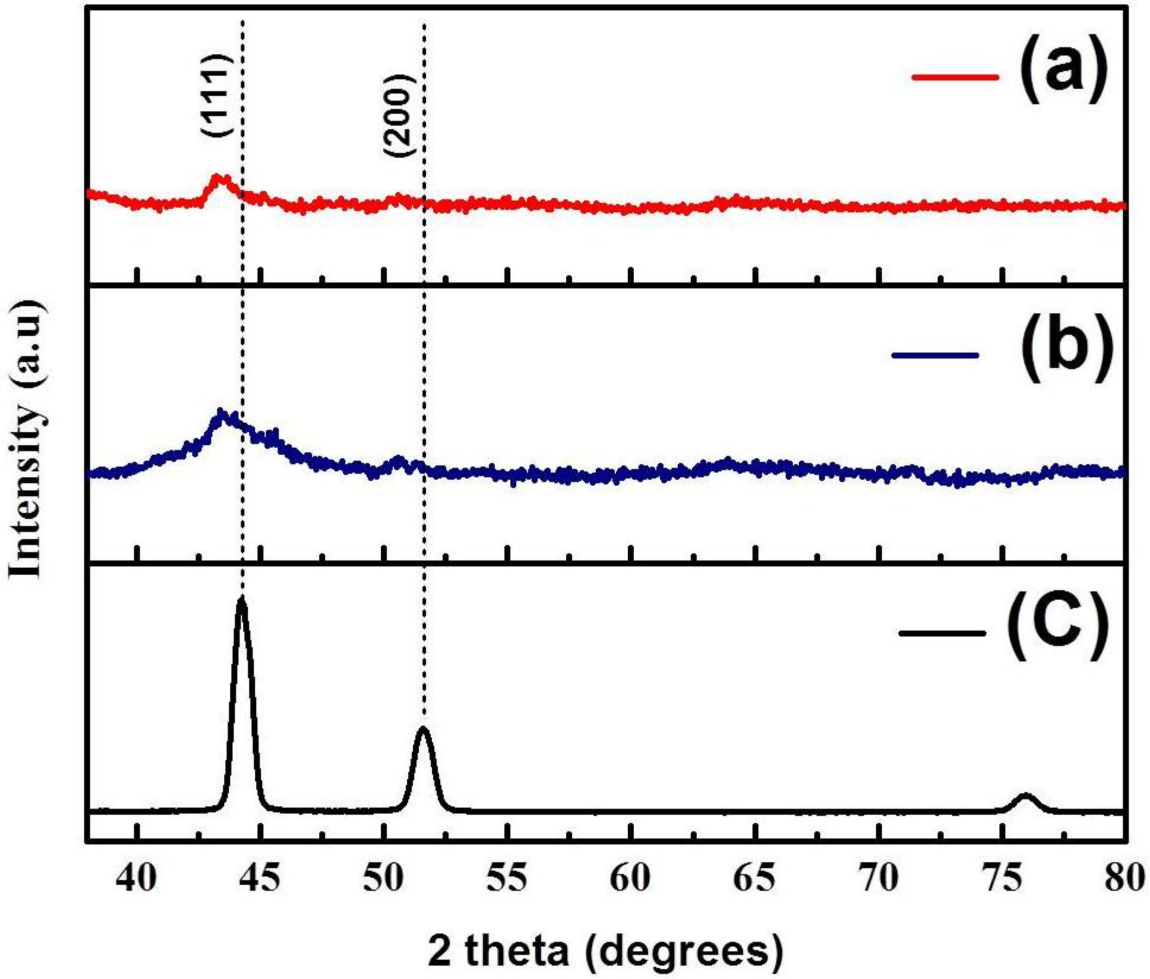

Figure 6.3 XRD pattern of (a) $Fe_{20}Ni_{80}$ particles synthesized in toluene, (b) $Fe_{20}Ni_{80}$ particles synthesized in ethanol and (c) reference $Fe_{20}Ni_{80}$ electrode.

XRD pattern of the nanoparticles synthesized in ethanol and toluene at 3.5 kV with 0.6 mm spacing between the FeNi electrodes is shown in Figure 6.3. XRD pattern of reference FeNi electrodes is shown in Figure 6.3 (c) for comparison. The peaks at 2θ values of 43.36° and 50.56° are assigned as (111) and (200) diffraction lines of fcc FeNi phase. The poorly crystalline nature of the nanoparticles is demonstrated by the presence of only two diffraction peaks and their low intensity. It is clearly visible that the XRD peaks are shifted towards lower angle in comparison to standard reference electrodes. This leads to dilation in lattice spacing in nanoparticles due to strain caused on them during the synthesis process. It also seems that solvent used namely toluene or ethanol does not change crystal structure.

XRD pattern of annealed particles at 450° C for 1 hour in forming gas and reference FeNi electrodes is shown in Figure 6.4. After annealing, the peak shifted back to its original position as that of reference electrodes which indicate particle are free of stress. The crystalline quality also improved.

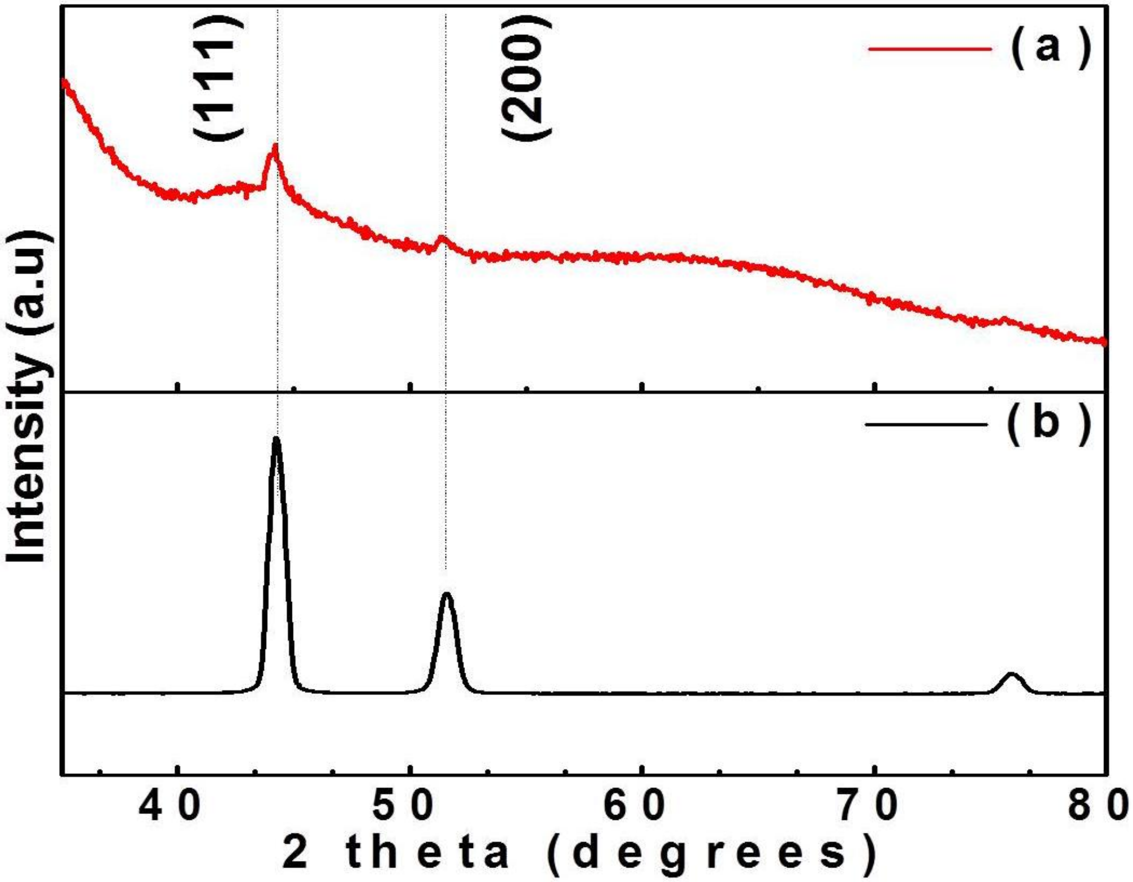

Figure 6.4 XRD patterns of (a) annealed $Fe_{20}Ni_{80}$ particles at 450° C for 1 hour in forming gas, and (b) reference $Fe_{20}Ni_{80}$ electrode.

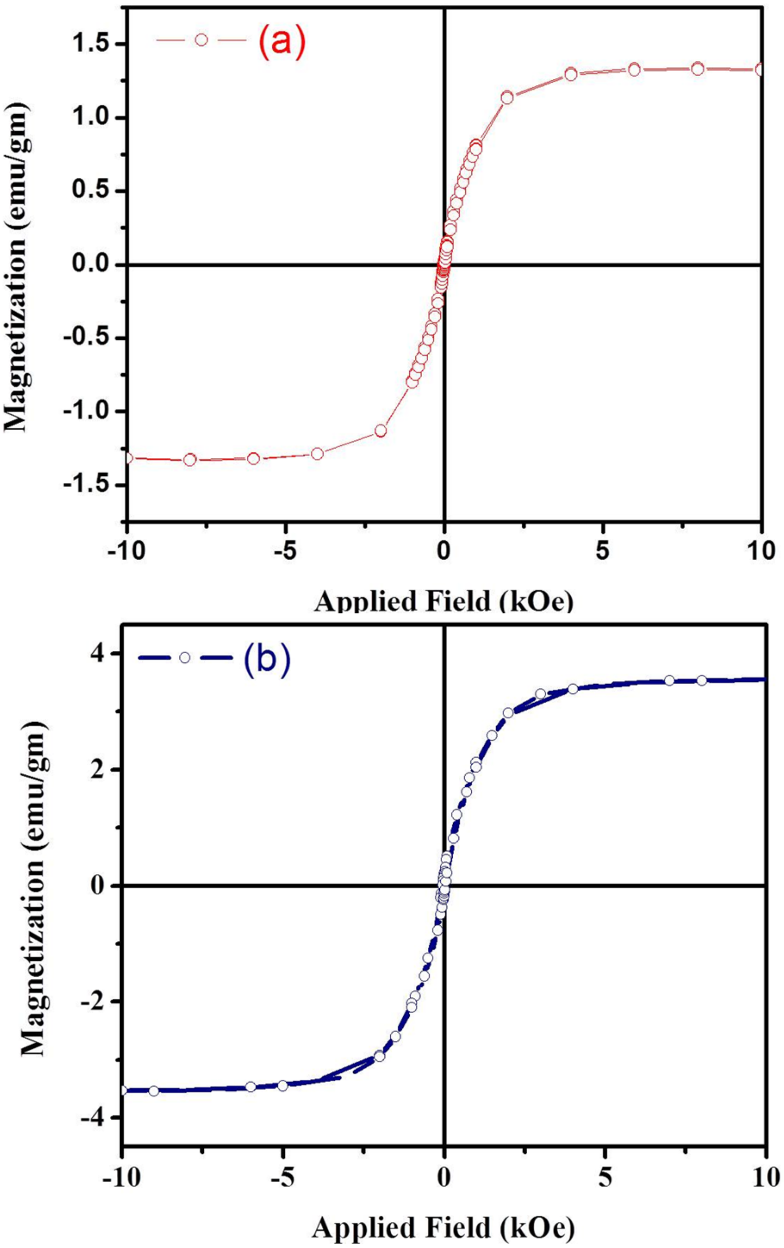

Figure 6.5 Magnetic hysteresis loops of (a) $Fe_{20}Ni_{80}$ particles synthesized in toluene, and (b) $Fe_{20}Ni_{80}$ particles synthesized in ethanol.

Figure 6.5 (a) and Figure 6.5 (b) shows magnetic hysteresis loops for the synthesized nanoparticles in toluene and ethanol at 3.5 kV with 0.6 mm electrode spacing respectively. Magnetic properties were measured at room temperature using VSM by applying a magnetic field of 10 kOe. Magnetic properties of the nanoparticles are size dependent. The nanoparticles have superparamagnetic like behavior. However, there are particles with a larger diameter and hence it leads to a narrow hysteresis. The saturation magnetization (Ms) and coercivity (Hc) for the synthesized nanoparticles in toluene are 1.34 emu/g and 10 Oe. The saturation magnetization (Ms) and coercivity (H_c) for the synthesized nanoparticles in ethanol are 3.6 emu/g and 40 Oe. Increase in Ms and Hc in nanoparticles synthesized in ethanol is larger due to carbon content and particle size. Overall, nonmagnetic phase (carbon) and crystalline quality of the material has a detrimental effect on the saturation magnetization per unit mass of the soft nanoparticles of FeNi.

6.2.2 Effect of applied voltage on Fe_{20} Ni_{80}

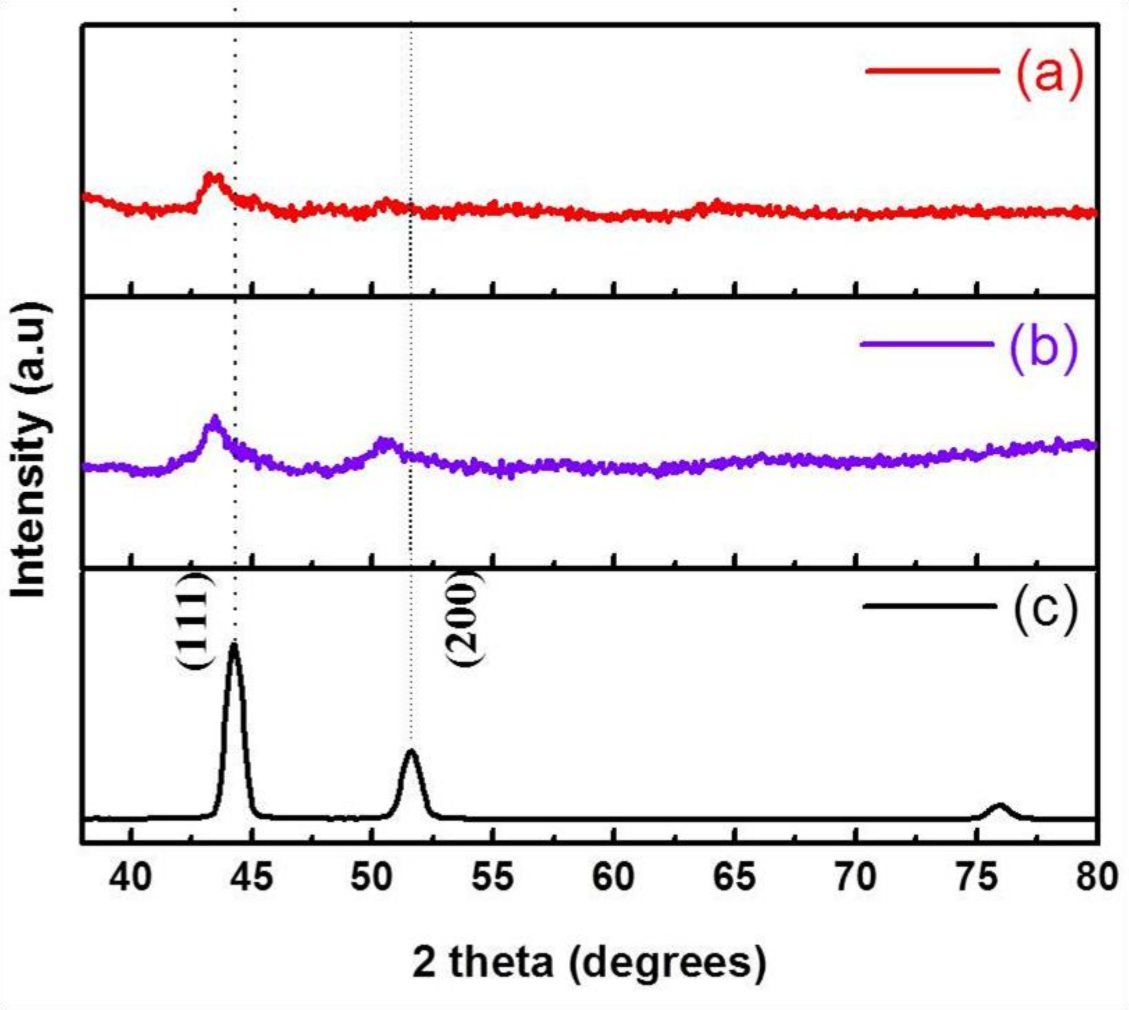

Figure 6.6 XRD pattern of $Fe_{20}Ni_{80}$ particles synthesized in toluene at (a) 3.5 kV, (b) 4.5 kV, and (c) reference $Fe_{20}Ni_{80}$ electrode.

The voltage on the electrodes was varied for two experiments at 3.5 kV and 4.5 kV using a constant voltage power supply. Toluene was used as a solvent for both experiments. XRD pattern of the nanoparticles synthesized in toluene at 3.5 kV and 4.5 kV with 0.6 mm spacing between the FeNi electrodes is shown in Figure 6.6. XRD pattern of reference FeNi electrodes is shown in Figure 6.6 (c) for comparison. The peaks at 2θ values of 43.36° and 50.56° are assigned as (111) and (200) diffraction lines of fcc FeNi phase. The poorly crystalline nature of the nanoparticles is demonstrated by the presence of only two diffraction peaks and their low intensity. It is clearly visible that the XRD peaks are shifted towards lower angle in comparison to standard reference electrodes. This leads to dilation in lattice spacing in nanoparticles due to strain caused on them during the synthesis process. It also seems that effect of voltage does not change crystal structure.

Magnetic properties were measured at room temperature using VSM by applying a magnetic field of 10 kOe. Figure 6.7 (a) and Figure 6.7 (b) shows magnetic hysteresis loops for the synthesized and annealed nanoparticles in toluene at 3.5 kV with 0.6 mm electrode spacing respectively. Magnetic properties of the nanoparticles have distinct voltage dependence. The nanoparticles have superparamagnetic behavior. However, there are particles with a larger diameter and hence it leads to a narrow hysteresis. The saturation magnetization (Ms) and coercivity (Hc) of the synthesized nanoparticles at 3.5 kV are 1.34 emu/g and 10 Oe. The saturation magnetization (Ms) and coercivity (H_c) of the annealed nanoparticles increased to 2 emu/g and 20 Oe. Increase in Ms and Hc in annealed nanoparticles is due to the improvement in the crystalline quality of the sample and increase in grain size.

Figure 6.7 (c) and Figure 6.7 (d) shows magnetic hysteresis loops for the synthesized and annealed nanoparticles in toluene at 4.5 kV with 0.6 mm electrode spacing respectively. The nanoparticles have superparamagnetic characteristics due to the smaller particle diameter. However, there are particles with a larger diameter and hence it leads to a narrow hysteresis.

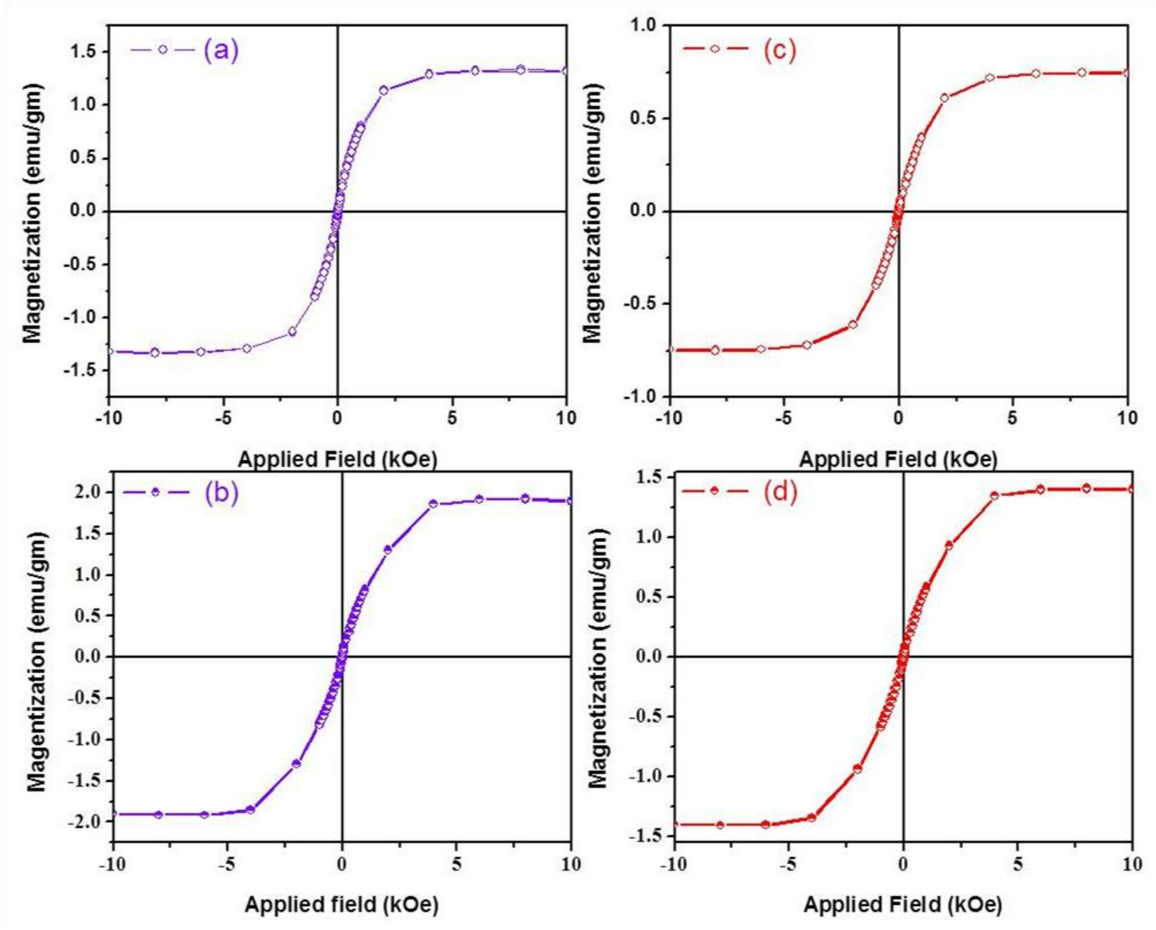

Figure 6.7 Magnetic hysteresis loops of $Fe_{20}Ni_{80}$ particles synthesized in toluene at (a) 3.5 kV, (b) 3.5 kV annealed, (c) 4.5 kV, and (d) 4.5kV annealed.

The saturation magnetization (Ms) and coercivity (Hc) for the synthesized nanoparticles at 4.5 kV are 0.75 emu/g and 20 Oe. The saturation magnetization (Ms) and coercivity (H_c) for the annealed nanoparticles increased 1.4 emu/g and 30 Oe. Increase in Ms and Hc in annealed nanoparticles is due to the improvement in the crystalline quality of the sample and an increase in grain size.

It can be seen that particles synthesized at 3.5 kV have higher magnetization and lower coercivity than at 4.5 kV. The reaction is much intense and loud at 4.5 kV leading amorphization and larger particles, which could be the reason for the change in magnetic properties leading to lower magnetization, and higher coercivity.

6.2.3 Effect of electrode spacing on Fe_{50} Ni_{50}

During the ultrasonic irradiation, the voltage on the electrodes was set at 2.5 kV using a constant voltage power supply. The solvents chosen for experiments were toluene. The spacing between the electrodes was set at 0.35 mm for the first set and 0.45 mm for the second set of experiment.

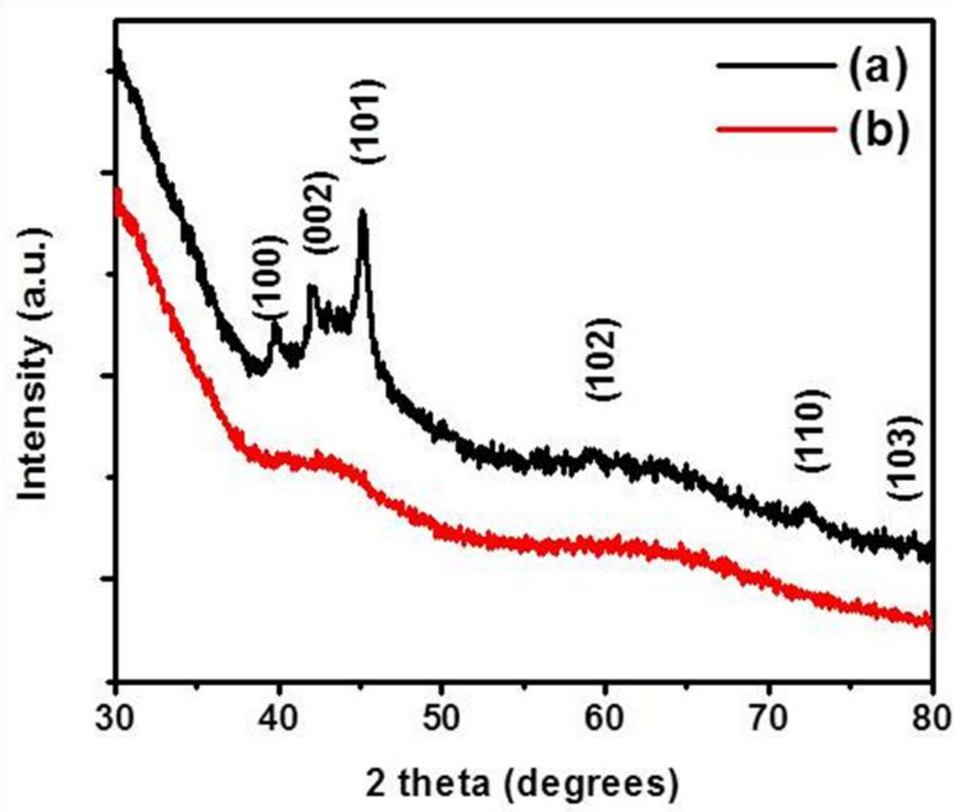

Figure 6.8 XRD patterns of $Fe_{50}Ni_{50}$ particles synthesized at 2.5 kV in toluene at (a) 0.35 nm and (b) 0.7 nm electrode spacing.

XRD pattern of the nanoparticles synthesized in toluene at 2.5 kV with 0.35 mm and 0.7 mm spacing between the FeNi electrodes is shown in Figure 6.8. The peaks at 2θ values of 39.83°, 42.17°, 45.12°, 59.15°, 72.58°, and 78.66° are assigned as (100), (002), (101), (102), (110), and (103) diffraction lines of hcp FeNi phase. The amorphous nature of the nanoparticles synthesized at 0.7mm is demonstrated by the absence of any diffraction peaks. It seems that spacing between electrodes changes the strength of electric field which affects the crystallinity of the nanoparticles synthesized.

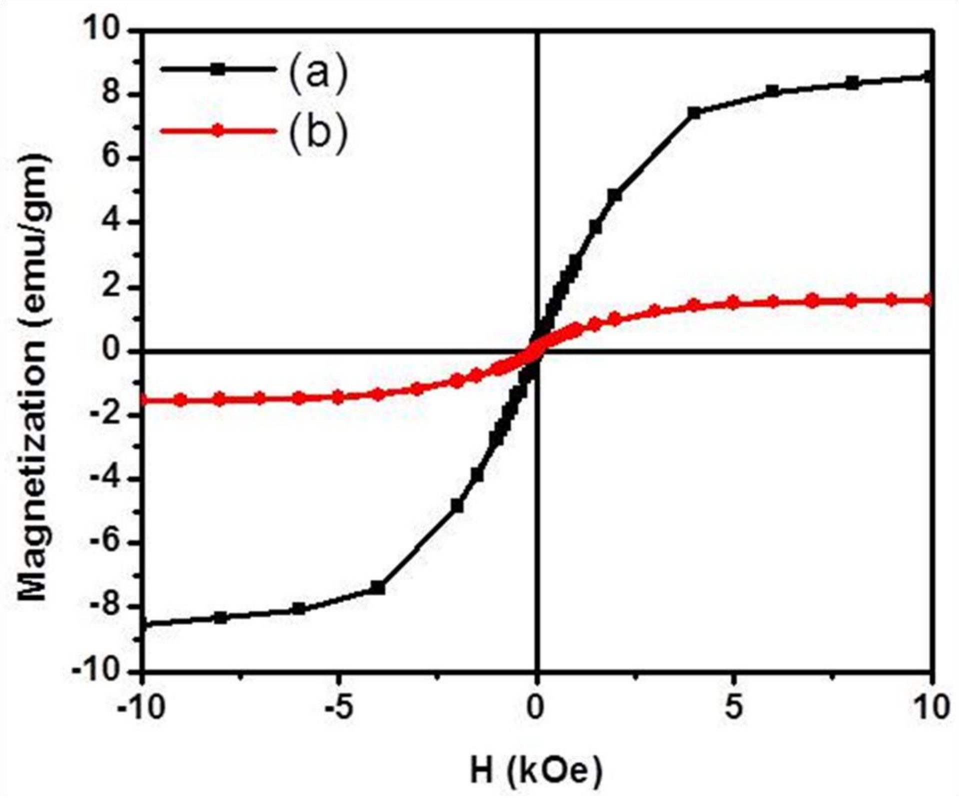

Figure 6.9 Hysteresis loops of $Fe_{50}Ni_{50}$ particles synthesized at 2.5 kV in toluene at (a) 0.35 nm and (b) 0.7 nm electrode spacing.

Figure 6.9 (a) and Figure 6.9 (b) shows magnetic hysteresis loops for the synthesized nanoparticles in toluene at 3.5 kV with 0.35 mm and 0.7 mm electrode spacing respectively. Magnetic properties were measured at room temperature using VSM by applying a magnetic field of 10 kOe. The sample was collected by attracting a magnet to the powder placed in a vial. Magnetic properties of the nanoparticles are highly dependent on electrode spacing. The nanoparticles have superparamagnetic characteristics since the particle diameter is smaller. However, there are particles with a larger diameter and hence it lead to a narrow hysteresis. The saturation magnetization (Ms) and coercivity (Hc) for the synthesized nanoparticles at 0.35 mm electrode spacing are 8.6 emu/g and 30 Oe. The saturation magnetization (Ms) and coercivity (Hc) for the synthesized nanoparticles at 0.7 mm electrode spacing are 1.65 emu/g and 20 Oe. The increase in Ms of the nanoparticles synthesized at 0.35mm is larger than at 0.7mm due to the crystalline character of the powder. Overall, nonmagnetic phase (carbon) has a detrimental effect on the saturation magnetization per unit mass of the soft nanoparticles of FeNi.

Electron microscopy images of FeNi nanoparticles synthesized in toluene 2.5 kV with 0.35 mm spacing between the electrodes is shown in Figure 6.10. Figure 6.10 (a) shows core-shell FeNi nanoparticles with several nested layers of carbon encapsulation. The contrast between the darker FeNi core and lighter carbon shell is clearly visible. The range of FeNi nanoparticles is 5-60 nm in diameter and C shell is 1-8 nm. TEM (Figure 6.10 (b)) shows a uniform distribution of smaller nanoparticles with few larger particles. 90 % of the particles are smaller than 10 nm and are core-shell with shell thickness varying with particles size since it acts as a catalyst for graphitization.

Figure 6.11 shows TEM images of FeNi nanoparticles synthesized above showing how smaller nanoparticles aggregate into a big particle. Figure 6.11 (a) shows TEM image of FeNi nanoparticles with a diameter in the range of 5-33 nm. Careful observation shows that there are two sets of nanoparticle distribution enfolded in carbon sheet. Very small particles are in the range of 5 nm and larger particles are in the average range of 25 nm in diameter. These particles appear to be on carbon sheet surrounded by a thick boundary of 20-25 nm. Figure 6.11 (b) shows TEM images of two larger FeNi nanoparticles. The smaller nanoparticles aggregate may have engulfed in carbon sheet to into a large core particle with thick carbon shell. The larger particle among the two is of diameter 700 nm with a shell of uniform thickness 38 nm. The smaller particle among the two is of diameter 400 nm with a shell of uniform thickness 30 nm. The shell thickness is clearly particle size dependent.

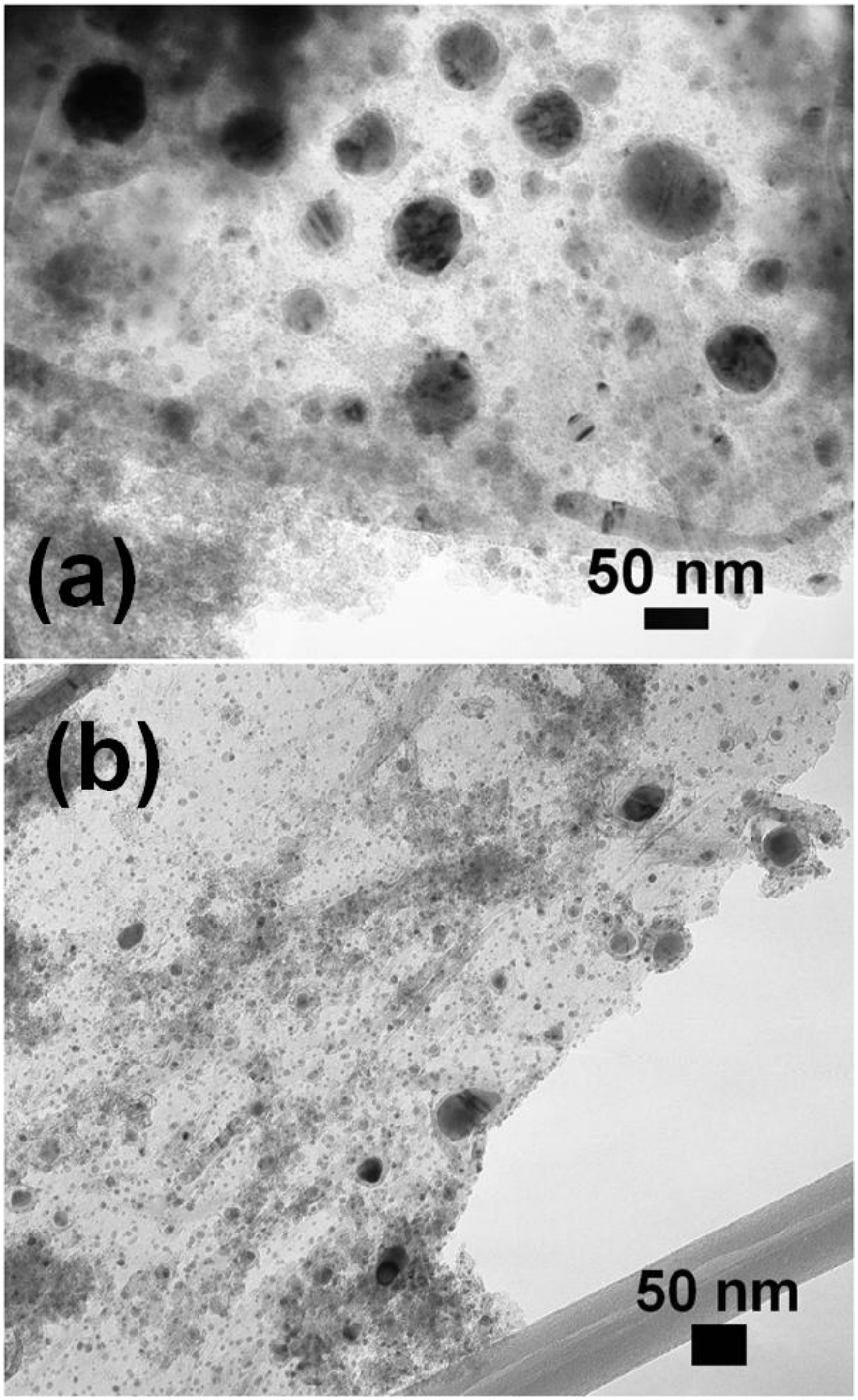

Figure 6.10 (a) TEM image of $Fe_{50}Ni_{50}$ core-C shell nanoparticles synthesized in toluene at 2.5 kV with 0.35 nm electrode spacings and (b) TEM image of smaller FeNi core-C shell nanoparticles synthesized in toluene at 2.5 kV with 0.35 nm electrode spacings.

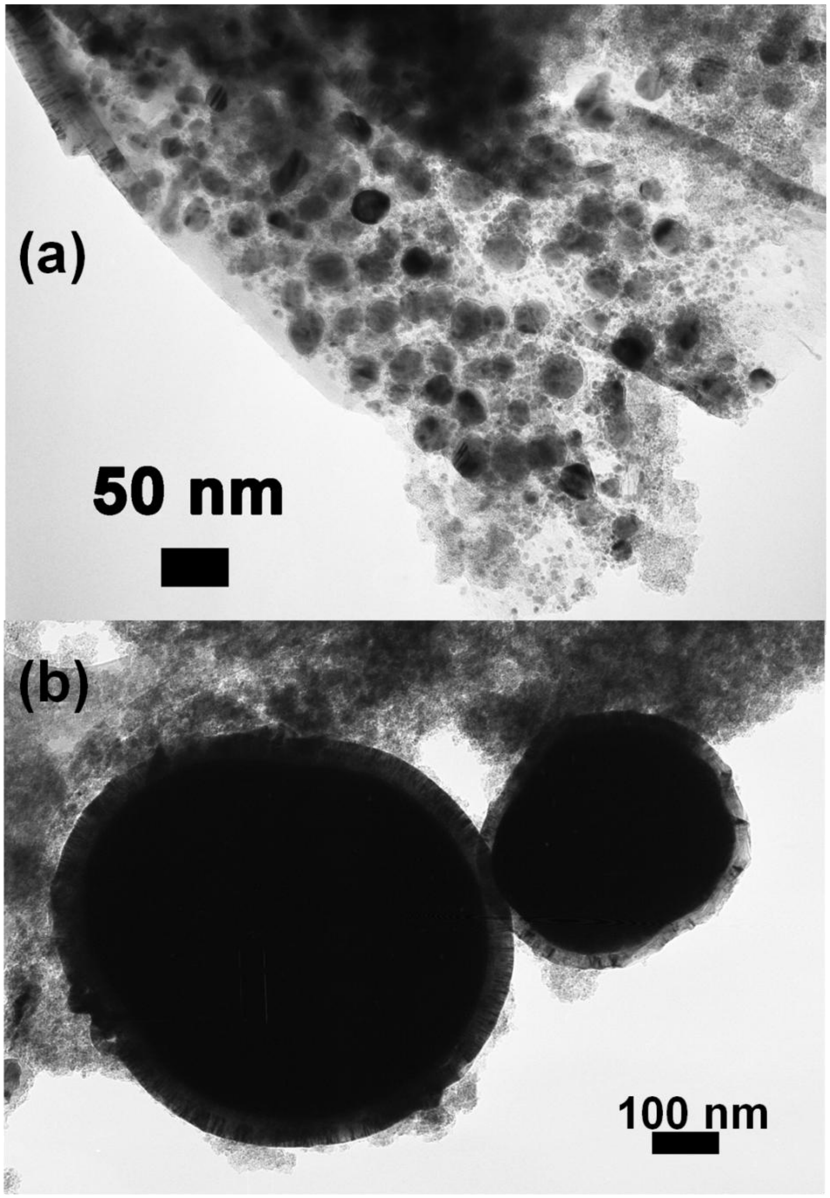

Figure 6.11 a) TEM image of $Fe_{50}Ni_{50}$ core-C shell nanoparticles synthesized in toluene at 2.5 kV with 0.35 nm electrode spacings surrounded graphite sheet and (b) smaller particles engulfed to form larger particles.

6.2.4 Effect of applied voltage on Fe_{50} Ni_{50}

XRD pattern of the nanoparticles synthesized in toluene with 0.35 mm spacing between the FeNi electrodes at varying voltages (a) 2.5 kV, (b) 4.0 kV, and (c) 4.8 kV is shown in Figure 6.12. The peaks at 2θ values of 39.83°, 42.17°, and 45.12° are assigned as (100), (002), and (101) diffraction lines of hcp FeNi phase (Figure 6.12 (a)). With the increase in voltage from 2.5 kV to 4.0 kV it appears that phase change from hcp to fcc takes place. Again with further increase in the voltage from 4.0 kV to 4.8 kV it appears that poorly crystalline nanoparticle is transformed to amorphous. The amorphous nature of the nanoparticles synthesized at 0.7mm is demonstrated by the absence of any diffraction peaks. It seems that voltage change leads to change in the

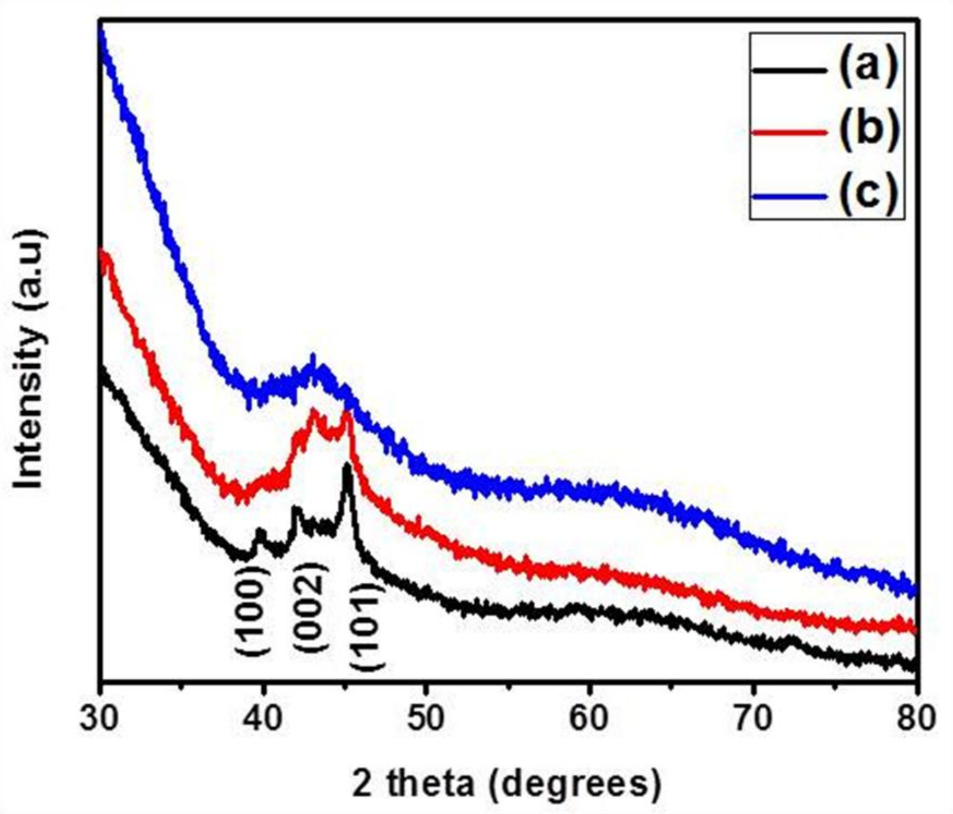

Figure 6.12 XRD patterns of $Fe_{50}Ni_{50}$ particles synthesized in toluene at 0.35 nm electrode spacing at different voltages (a) 2.5 kV, (b) 4.0 kV, and (c) 4.8 kV.

strength of electric field which affects the crystallinity and the phase of the nanoparticles synthesized.

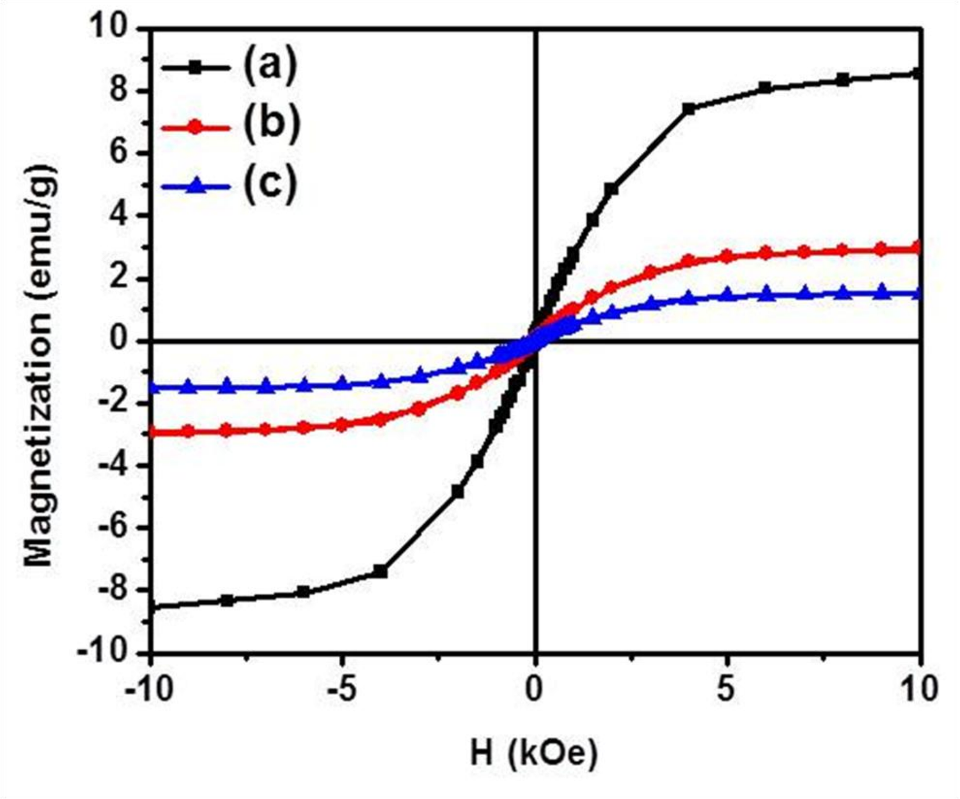

Figure 6.13 Hysteresis loops of $Fe_{50}Ni_{50}$ particles synthesized in toluene at 0.35 nm electrode spacing at different voltages (a) 2.5 kV, (b) 4.0 kV, and (c) 4.8 kV.

Figure 6.13 (a), (b), and (c) shows magnetic hysteresis loops for the nanoparticles synthesized in toluene at 0.35 mm electrode spacing with different voltages (a) 2.5 kV, (b) 4.0 kV, and (c) 4.8 kV respectively. Magnetic properties were measured at room temperature using VSM by applying a magnetic field of 10 kOe. The sample was collected by attracting a magnet to the powder placed in a vial. Magnetic properties of the nanoparticles are highly dependent on varying voltage. The nanoparticles have superparamagnetic characteristics since the particle diameter is smaller. The saturation magnetization (Ms) for the synthesized nanoparticles at 0.35 mm electrode spacing at 2.5 kV, 4.0 kV, and 4.8 kV are 8.6 emu/g, 2.95 emu/g, and 1.54 emu/g. The decrease in Ms of the nanoparticles with an increase in applied voltage is due to change in phase and crystalline nature of the powder.

6.3 Conclusions

$Fe_{20}Ni_{80}$ were synthesized using a versatile plasma discharge method. For $Fe_{20}Ni_{80}$ composition, the effect of morphology and magnetic property on the type of solvent was investigated. FeNi core of 15-820 in diameter were covered by 1-34 C shell in ethanol. FeNi core of 3-820 in diameter were covered by 1-60 C shell in toluene. The shell thickness is lower in particle synthesized by ethanol in comparison to toluene. Magnetization also decreases from 3.6 emu/g when prepared in ethanol to 1.34 emu/g when prepared in toluene. The effect of applied voltage on magnetic property of nanoparticles was also investigated. The saturation magnetization decreases with increase in voltage from 1.34 emu/g to 0.75 emu/g.

For $Fe_{50}Ni_{50}$ composition, the effect of electrode spacing on the structure and the magnetic property was investigated while keeping the voltage constant. When the spacing of electrode was increased from 0.35 mm to 0.7 mm, hcp Ni transformed to fcc FeNi. The crystalline nature of hcp phase was transformed to amorphous. Magnetization also decreased from 8.6 emu/g to 1.65 emu/g.

In the second part, the effect of varying voltage on the structure and the magnetic property was investigated while keeping constant electrode spacing. When the voltage was increased from 2.5 kV to 4.0 kV to 4.8 kV, hcp FeNi transformed to a mixture of fcc plus hcp FeNi to fcc FeNi at the cost of crystallinity. The powder transforms from crystalline to amorphous. Magnetization also decreases with increase in voltage. The saturation magnetization at 2.5 kV, 4.0 kV and 4.8 kV is 9.7 emu/g, 2.95 emu/g, and 1.54 emu/g.

Chapter 7

Synthesis and characterization of Pd nanoparticles

7.1 Introduction

Noble metal nanoparticles are of great technological interest due to their relevance in the areas of catalysis, fuel cells, and storage or detection of hydrogen [48, 128, 129]. Palladium (Pd) is one of the best-known hydrogen storage metals for its unique ability to absorb large volumetric capacity of hydrogen from gas and electrolyte [130-132]. Pd nanoparticles have been intensively researched in hydrogen storage and catalytic reactions. The diffusion of hydrogen into the Pd nanoparticles causes a phase transformation, thereby changing electronic and structural properties, and affecting the overall properties [133]. Recently it has been shown that hydrogen diffusion into the subsurface of Pd nanoparticles has been facilitated by carbon (C) through atomically flexible low-coordinated surface sites. Composite materials of Pd and C can thus exhibit better absorption properties and enhancement of hydrogen storage than single counterparts [134, 135].

Notable efforts have been devoted to the critical aspect of developing nanoparticles with narrow size and spatial distribution that enables the optimization of properties over a broad range of applications. Therefore, preparations, structural determination, and study of the properties are of paramount importance to design high-performance materials. Pd based nanomaterials are synthesized in the multistep process by a broad range of experimental techniques including sputtering, ion or electron beam deposition, laser ablation, hydrothermal methods, electrochemical deposition and chemical reduction methods [47, 136-140]. These methods differ in degree of complexity (multi-step), production, purity, safety, and economics.

In the frame of finding a one-step method to synthesize Pd nanoparticles, here we report a unique unconventional top-down synthesis approach. Pd nanoparticles were synthesized using plasma discharge in the cavitation field of toluene caused from ultrasonication. This method offers a unique advantage, which includes a rapid reaction rate with the ability to form very small nanoparticles with narrow size distribution. Well-dispersed Pd nanoparticles with narrow size distribution embedded in C matrix were synthesized for 1 hour (h) and 2 h synthesis time. The influence of experiment time shows a distinct expansion in the Pd lattice spacings due to the hydrogen diffusion from the broken bonds in toluene. The role of hydrogen induced lattice expansion of Pd is also addressed using the density functional theory (DFT) studies. This paper demonstrates a novel way of hydrogen production from toluene and direct storage in plasma generated nanoparticles.

7.2 Experimental and computation methodology

7.2.1 Experimental method

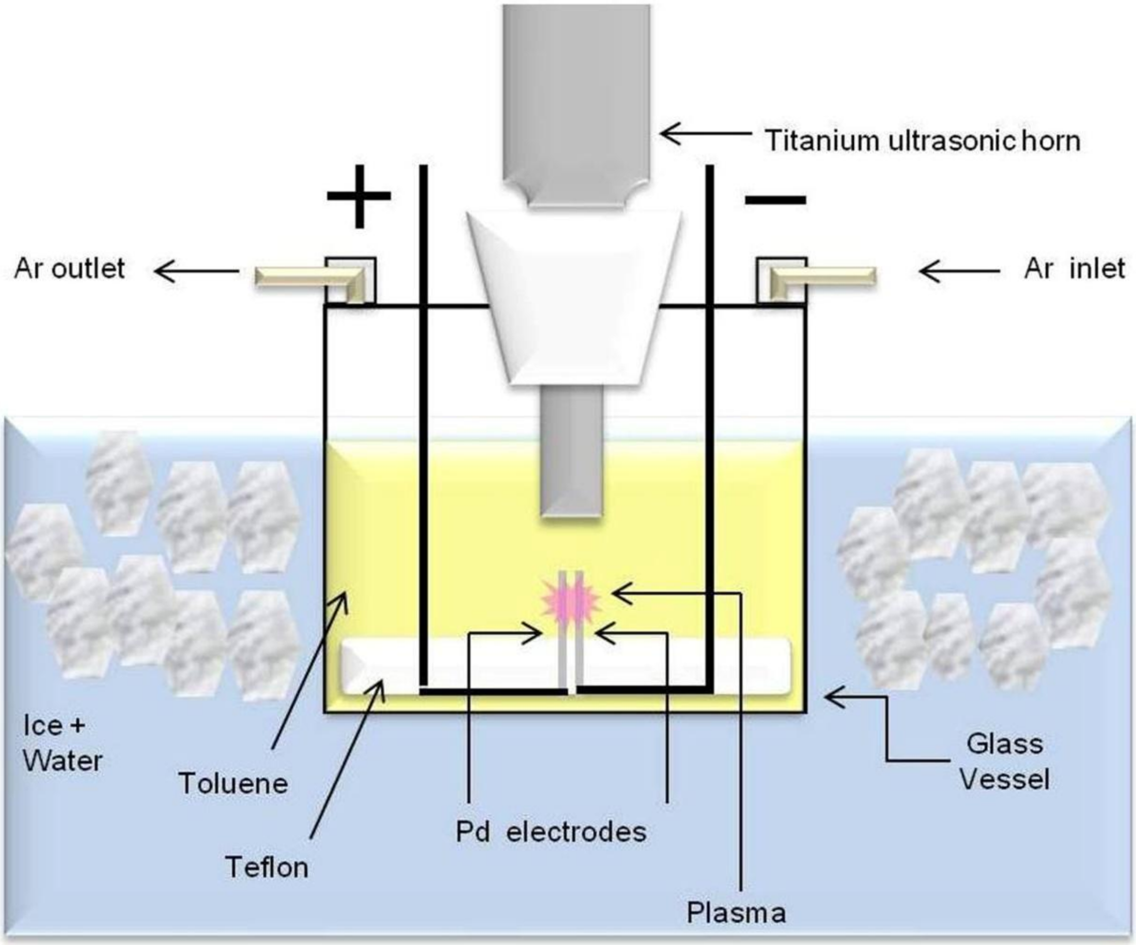

Figure 7.1 Schematic of the experimental set up that is used to synthesize core-shell nanoparticles.

Figure 7.1 shows a schematic diagram of the experimental apparatus used for Pd nanoparticle synthesis. An ultrasonic processor (Sonics, VCX 750) with a titanium horn 19 mm in diameter was used to irradiate 275 ml of toluene (Sigma-Aldrich, anhydrous 99.8%) at 750 watts and 20 kHz. A glass vessel filled with ice water was underneath and Argon gas flow was directed into the closed geometry containing toluene to maintain an inert atmosphere. As shown in Figure 1, two Pd electrodes (Alfa Aesar, 1 mm in diameter, 99.99%) were inserted 0.5 mm apart from each other beneath the bottom of the ultrasonic horn. The distance between the electrodes and the bottom of the horn was kept constant at 10 mm. During the ultrasonic irradiation, the voltage between the electrodes was kept at 3.5 kV using a constant voltage power supply.

Ultrasound in toluene generates acoustic cavitations, which is the formation and implosive collapse of bubbles [141]. The collapse of cavitation between Pd electrodes in a strong electric field polarizes the π-electrons in toluene and thus creates a plasma. The dissociation of hydrogen and carbon in toluene due to the breaking of chemical bonds leads to a unique way of hydrogen production. Quasi-stable nanoparticles are formed when energetic plasma encounters electrodes either by nucleation in the vapor or molten Pd and then after the rapid quenching, stable nanoparticles are formed [6, 49].

Pd powder was dispersed in ethanol, dropped onto a carbon-coated copper grid and dried for the high-resolution transmission electron microscopy (HRTEM) investigation. HRTEM (Hitachi H-9500, operated at 300kV) observations allowed us to determine the overall morphology and the crystal structure of the sample. The chemical composition of the nanoparticles was analyzed using Energy Dispersive X-ray spectroscopy (EDX) linked with the HRTEM. The crystal structure of nanoparticles was also determined using X-ray diffraction (XRD) with monochromatic Cu K_α radiation (Bruker D8 diffractometer).

7.2.2 Computational methodology

The density functional theory (DFT) was used as the theoretical framework for the computational part of this work, as implemented in Vienna ab-initio simulation package (VASP) [142-145]. The projector augmented wave (PAW) method was used with generalized gradient approximation (GGA) through Perdew-Burke-Ernserhof (PBE) exchange-correlation functional [146-148]. The total energies of the test structures were calculated after all the structures were relaxed fully. Each ion was relaxed until the force is equal or less than 0.01eV/Å while the kinetic energy cut-off for the plane wave basis set was 400 eV. The fcc Pd structures with hydrogen (H) atom in different octahedral and tetrahedral sites was relaxed with 11x11x11 k-points using Methfessel-Paxton method of order 1 and the integrations were calculated using linear tetrahedron method [149, 150].

To study the lattice changes and hence the volume expansions, we have taken a set of fcc Pd structures with H atoms in different octahedral (O) and tetrahedral (T) sites in different numbers and arrangements. We calculated their lattice parameters along with their energetics to find the most stable structures. For those structures, we calculated the volume expansion and compared that with the pristine Pd crystal structure. After that, we matched our computational results with the experimental findings. Figure 7.2 shows the octahedral and tetrahedral sites in fcc Pd crystals. We have placed one, two, three and four H atoms in four octahedral sites separately and calculated the formation energy for each H insertion in those sites. For eight tetrahedral sites, we have placed up to four H atoms in different combinations in these sites.

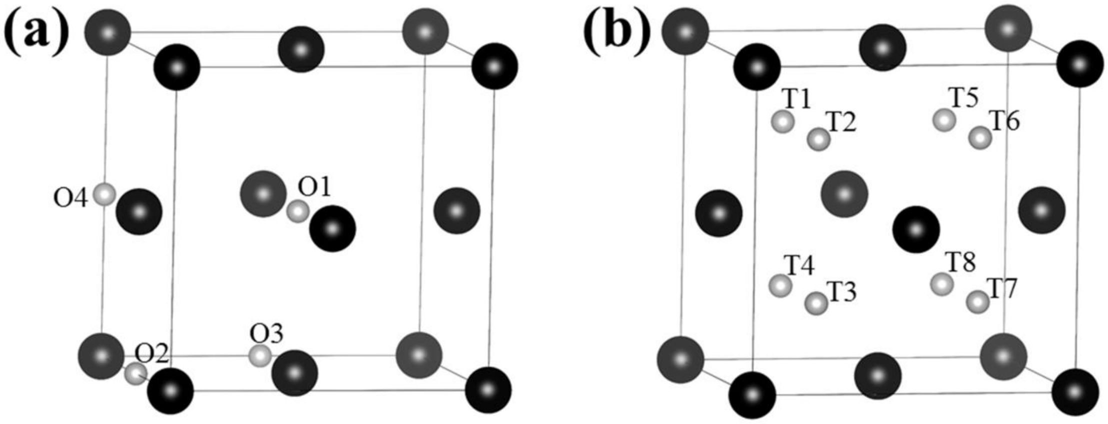

Figure 7.2 FCC palladium structures with (a) four octahedral sites (O1-O4) and (b) eight tetrahedral sites (T1-T8) in the crystal.

The energy of formation of a Pd-H system per H atom at H-rich condition was calculated using the following formula:

$$E_f = \frac{1}{y}\left(E(Pd_xH_y) - xE(Pd) - \frac{y}{2}E(H_2)\right) \qquad (7.1)$$

where E (Pd_xH_y) is the total energy of a Pd-H system, E (Pd) is the total energy of a palladium atom in bulk and E (H_2) is the free energy of a hydrogen dimer in a cubic box where the length of each side of the box is 10Å.

7.3 Results and discussion

7.3.1 Effect of experiment time on morphology and structure of nanoparticles

Nanoparticles size, morphology, chemical composition and crystal structure were investigated using HRTEM. Figure 7.3(a) shows spherical, solid Pd nanoparticles synthesized for 1 h experiment time. Nanoparticles with the narrow size distribution of 2-7 nm are homogeneously distributed and embedded in an amorphous carbon matrix. Their size distribution histogram (Figure 7.3(b)) is described quite well by a lognormal function with a median diameter of 3.4 nm and a standard deviation of 1.1 nm. The synthesis of smaller nanoparticles is challenging since they have a tendency to aggregate and reduce surface tension, however, carbon matrix interrupts and hinders such aggregation and hence it preserves small particle sizes. It can be seen from high magnification HRTEM image (Figure 7.3(c)) that these nanoparticles are single crystalline. The spacing of lattice fringes from both insets in HRTEM image is 0.228 nm corresponding to (111) plane of fcc Pd [151]. EDX spectra (Figure 7.3(d)) of nanoparticles in carbon matrix exhibited the characteristic peaks associated with Pd and C. EDX spectra suggest that nanoparticles exposed to air undergo a surface oxidation. The presence of Cu is due to the TEM grid.

TEM image of Pd nanoparticles synthesized in 2 h experiment time is shown in Figure 7.4. Their size distribution histogram (Figure 7.4(b)) is again described quite well by a lognormal function. However, there is an increase in nanoparticle size with a median diameter of 4.7 nm and a standard deviation of 1.9 nm. Nanoparticles are well dispersed with the relatively narrow size distribution of 2-11 nm and are embedded in an amorphous carbon matrix. At the microscopic level, the spacing between the electrodes could have changed due to the constant blitz of plasma on the Pd electrodes. Hence, the effect of cavitations, which creates the plasma in the high electric field between the electrodes might alter, which can lead to an increase in particle size with longer experiment time. It can be seen from high magnification HRTEM image (Figure

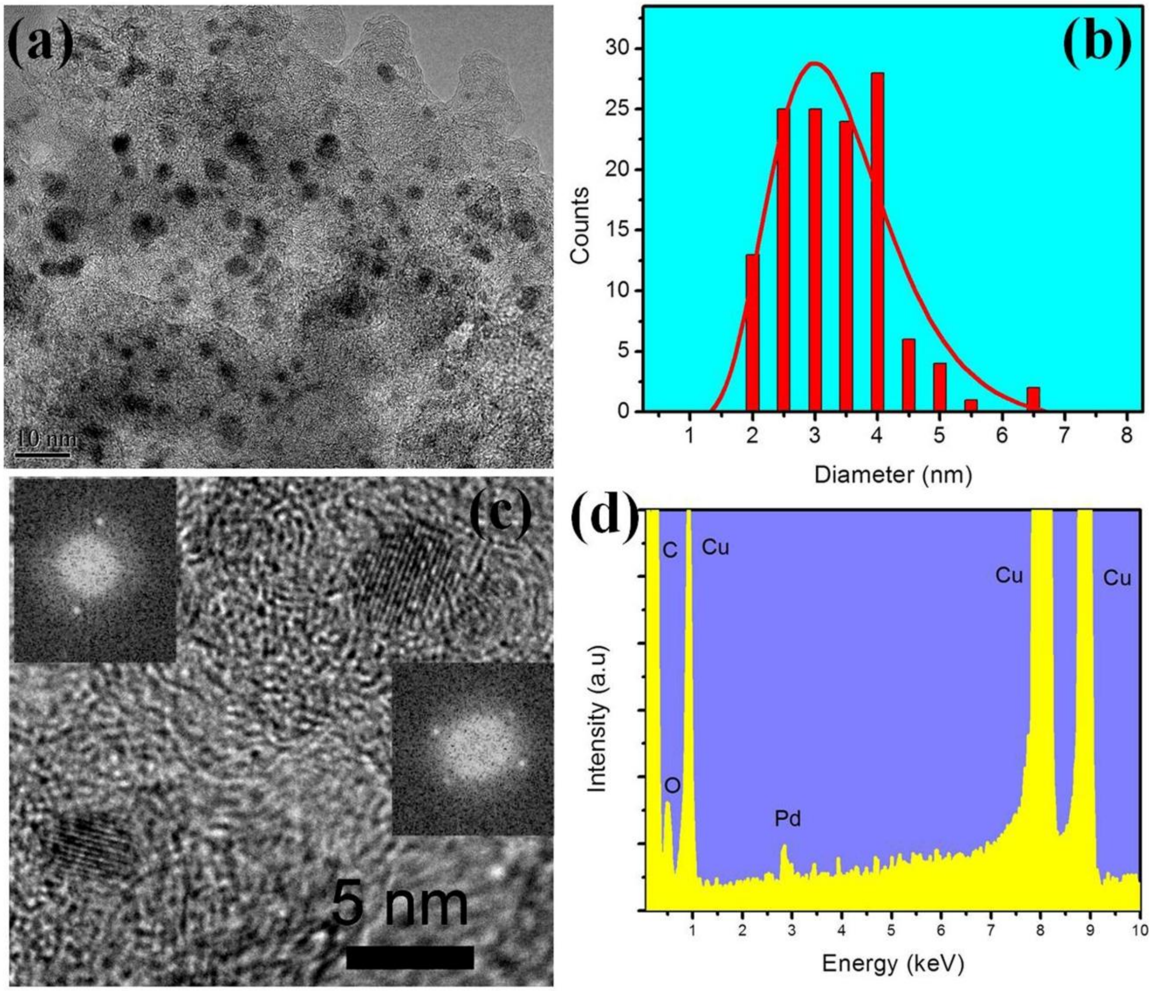

Figure 7.3 (a) HRTEM image of Pd nanoparticles synthesized for 1h, (b) Size distribution histogram of Pd nanoparticles (c) High magnification HRTEM image of single crystalline Pd nanoparticles. Insets show FFT of the corresponding particle with (111) plane (d) EDX spectrum of the synthesized nanoparticles.

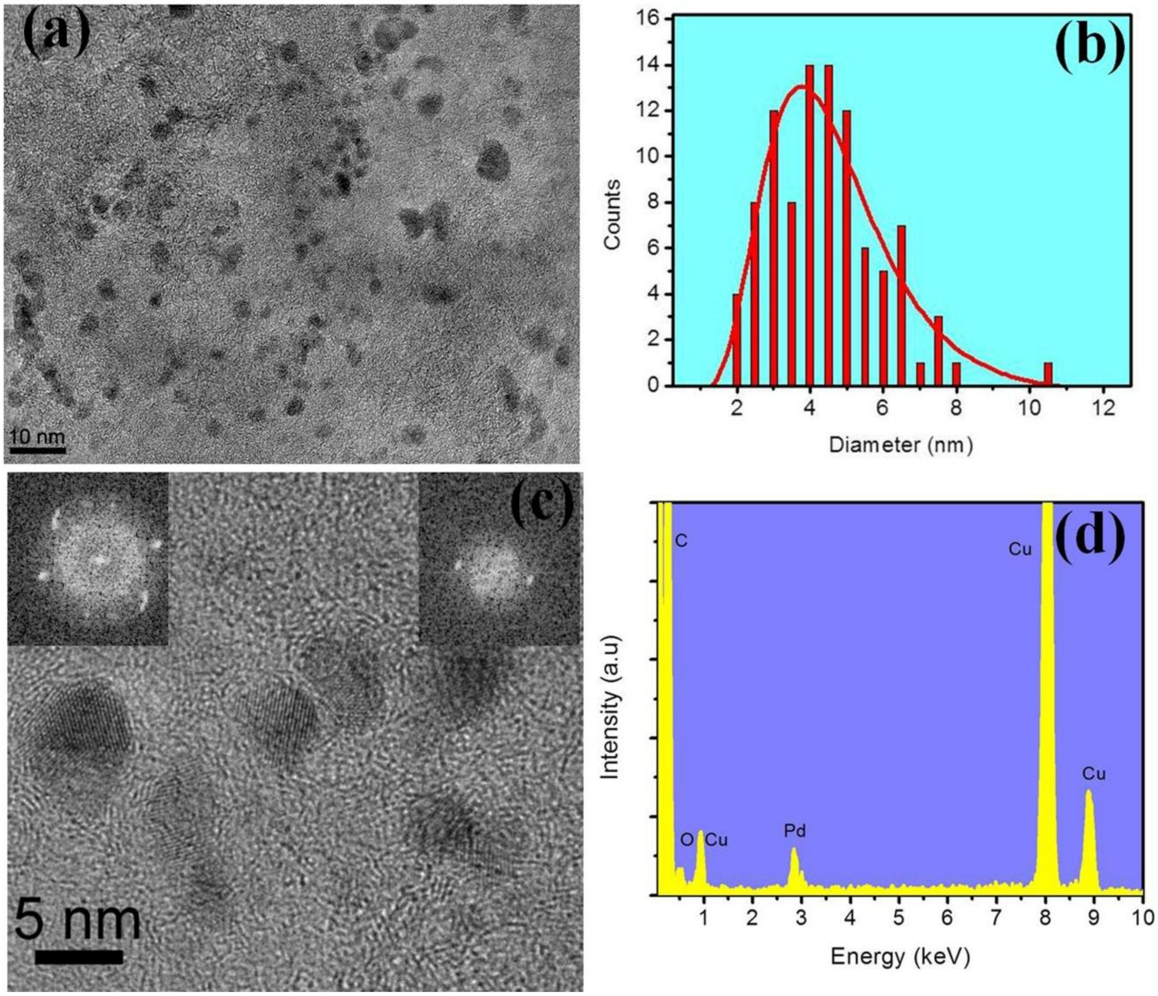

Figure 7.4 (a) HRTEM image of Pd nanoparticles synthesized for 2 h, (b) Size distribution histogram of Pd nanoparticles (c) High magnification HRTEM image of Pd nanoparticles. Insets show FFT of the corresponding particle with (111) plane (d) EDX spectrum of the synthesized nanoparticles.

7.4(c)) that these nanoparticles have good crystalline structure. The lattice spacing from both insets in HRTEM image of single crystalline nanoparticles is 0.233 nm corresponding to (111) plane of fcc Pd [151]. The EDX spectra of nanoparticles exposed to air (Figure 7.4(d)) exhibited the characteristic peaks associated with Pd and C. It can be concluded from HRTEM investigation that this experimental method ensures important advantages namely Pd nanoparticles prepared in toluene shows better particle size distribution, smaller average size, and negligible agglomeration.

The structural change with experiment time is elucidated in XRD spectra (Figure 7.5). Although the peaks in the spectra, as well as the relative intensities of the peaks from the nanoparticles synthesized in toluene, are matched to the

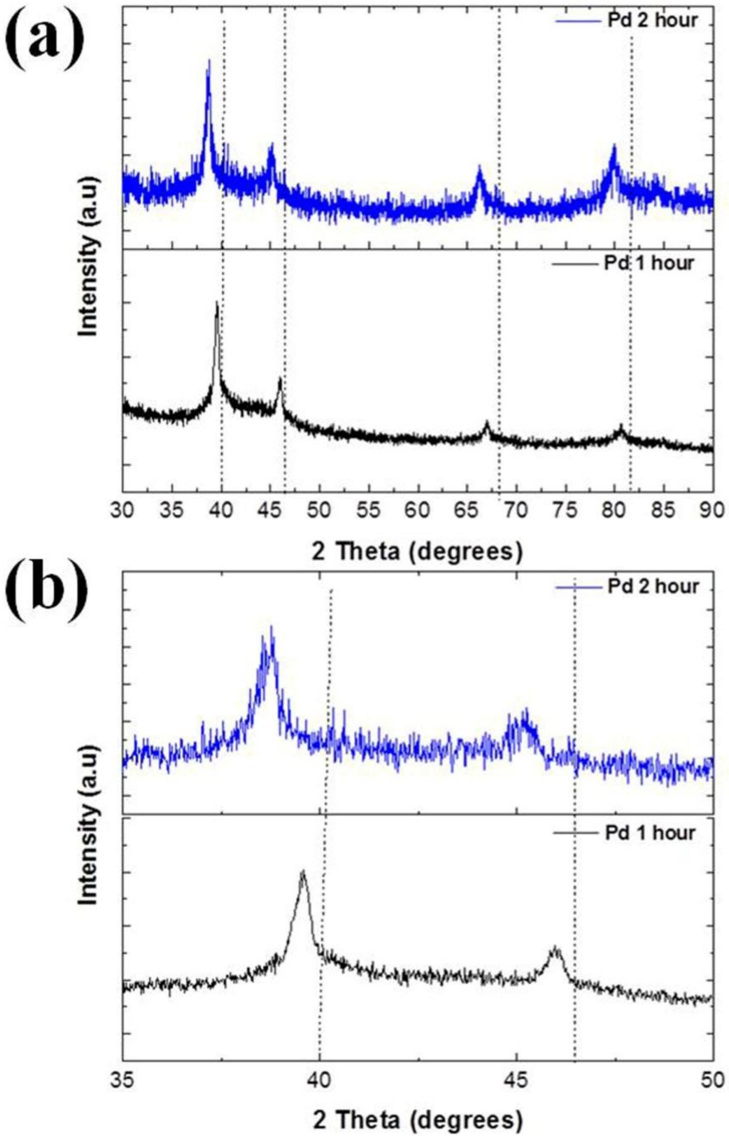

Figure 7.5 (a) XRD pattern of the nanoparticles synthesized for 1 h and 2 h experiment time (b) Expanded view of figure 5(a) for 2θ in the range from 35°-50°.

the spectrum of Pd, however, they exhibit a distinct shift towards lower angles as compared to the spectrum from standard Pd [151]. This indicates a lattice expansion of the nanoparticles. For 1 hour experiment time, the peaks at 2θ values of 39.58°, 46°, 67.05°, 80.64° and 84.99° are assigned as (111), (200), (220), (311) and (222) diffraction lines as for fcc Pd [151]. The d-spacings from the spectra are 0.228 nm, 0.197 nm, 0.140 nm, 0.119nm, and 0.114 nm, which shows an expansion from the reported values of 0.225 nm (111), 0.195 nm (200), 0.138 nm (220), 0.117 nm (311), and 0.112 nm (222) for Pd crystal structure [151]. Similarly, for 2 h experiment time, the peaks at 2θ values of 38.67°, 45.15°, 66.26°, 79.94° and 84.19° are assigned as (111), (200), (220), (311) and (222) diffraction lines as for fcc Pd [151]. The d-spacings from the spectra are 0.233 nm, 0.201 nm, 0.141 nm, 0.120 nm, and 0.115 nm, which shows an expansion from the reported values of 0.225 nm (111), 0.195 nm (200), 0.138 nm (220), 0.117 nm (311), and 0.112 nm (222) for Pd crystal structure [151].

The lattice constant corresponding to fcc Pd calculated synthesized for 1 h and 2 h experiment times are 0.395 nm and 0.403 nm respectively. The lattice constant for pristine Pd is 0.389 nm. The increase in lattice constant for 1 h and 2 h experiment time are 0.0056 nm and 0.014 nm respectively. The lattice expansion is 1.44% and 3.60% respectively. Dilated lattices result in a volume expansion of 4.4 % and 11.15 % for 1 h and 2 h experiment time respectively. Such lattice expansion of Pd is well known due to the hydrogen incorporation into the Pd lattice i.e. diffusion of hydrogen in the fcc lattice of Pd where the hydrogen atoms partially fill the octahedral sites in the lattice [152]. The diffusion of hydrogen atoms into Pd nanoparticles could originate from thermochemical reactions, which take place in the toluene (and result in the release of hydrogen) at the plasma/liquid-electrode interface, induced at the high temperature. The result suggests that the hydrogen atoms are strongly confined and stabilized into Pd nanoparticles. It has been shown that compared to bulk Pd, hydrogen atoms are strongly trapped inside Pd nanoparticles because of the formation of stable Pd−H bonds [153]. It can be concluded from XRD investigation that the lattice expansion and hence hydrogen storage depends on experiment time which clearly shows distinct particle size dependence.

7.3.2 Effect of hydrogen in Pd lattice dilation by DFT

To verify these experimental findings, here we show our computational results as presented in Table 3. Based on energetics, the table shows that the most probable occupation sites by H atoms are tetrahedral sites, which agrees with another computational work as in ref. [154]. The energy of formation a Pd-H system at H-rich condition per H atom is the lowest for H atoms occupying tetrahedral sites, which is -2.49 eV per H atom when T1, T6, and T8 sites are occupied by three hydrogen atoms. The second lowest structure has the formation energy of -2.48 eV when T1 and T3 sites are occupied by two hydrogen atoms. The sites are defined in Figure 7.2. Since the experiment was carried out for one and two hours, and the nanoparticles are found to have different lattice parameters and volume expansions compared to pristine palladium structures. In that case, along with the consideration of energetics from the calculation, we need to match the lattice parameter and volume expansion with that from the experiment. Out of all the possible arrangements of H in different interstitial sites in palladium crystal, Table 7.3 shows that, when H atom occupies an octahedral site (any of the four sites O1, O2, O3, and O4), the volume and the lattice constant expansions become very close to that from the 1h experiment. The calculated values for lattice expansion, in this case, are 1.35-1.38 % while the calculated volume expansions are 4.10-4.18%. The best match is found when one H atom is in site O2 or O4. Either in sites O2 or O4, the lattice and volume expansions are 1.38% and 4.18% while the corresponding values from the 1h experiment are 1.44% and 4.4% respectively. The formation energy per H atom at any of the four octahedral sites is -2.41eV, which shows that this occupation is energetically possible. To match the expansion from the 2h experiment, we see that the closest structure is found with three H atoms occupied three octahedral sites O1, O2, and O3. For this structure, the lattice and volume expansions are 3.63% and 11.29% while that from the 2h experiment are 3.60% and 11.15% respectively. The formation energy per H atom for this structure is -2.42eV that indicates this structure is thermodynamically possible to form. Although the table shows that tetrahedral sites are energetically more favorable to be occupied than octahedral sites, our best match for the expansions with the experiment is found for octahedral

Table 3 Calculated lattice parameters and energetics of H inserted in different octahedral and tetrahedral sites in Pd crystal.

Number of H atoms in Pd crystal	Palladium crystal structures with H atoms inserted in sites	Volume of fully relaxed structures (Å³)	Volume expansion after H insertion, ΔV%	Lattice parameter of fully relaxed structures, a (Å)	Lattice expansion after H insertion, Δa% = 100×(a-a∘)/a∘	Energy of formation per H atom at H-rich condition (eV)
0	A pristine fcc Pd crystal	61.74		3.95		
1	O1	64.28	4.11	4.01	1.36	-2.41
	O2	64.32	4.18	4.01	1.38	-2.41
	O3	64.27	4.1	4.01	1.35	-2.41
	O4	64.32	4.18	4.01	1.38	-2.41
2	O1, O2	66.64	7.94	4.06	2.59	-2.43
3	O1, O2, O3	68.71	11.29	4.1	3.63	-2.42
4	O1, O2, O3, O4	70.61	14.37	4.13	4.58	-2.4
1	T1	65.43	5.98	4.03	1.96	-2.39
2	T1, T2	68.73	11.32	4.2	6.34	-2.43
	T1, T3	69.02	11.79	4.07	2.85	-2.48
	T1, T7	69.9	13.22	4.12	4.23	-2.42
3	T1, T2, T4	71.99	16.6	4.23	7.01	-2.42
	T1, T3, T7	72.9	18.08	4.11	4.01	-2.45
	T1, T6, T8	72.48	17.4	4.17	5.49	-2.49
4	T1, T2, T3, T4	75.2	21.8	4.4	11.43	-2.37
	T1, T2, T4, T5	75.3	21.96	4.22	6.84	-2.38
	T1, T3, T5, T7	76.56	24	4.5	13.93	-2.44
	T1, T3, T5, T8	76.12	23.29	4.35	10.09	-2.43
	T1, T3, T6, T8	76.18	23.39	4.24	7.26	-2.47

sites only. However, Table 7.3 shows that a structure having two H atoms occupying two tetrahedral sites T1 and T3 has even lower formation energy of -2.48 eV, which is one of the lowest of all the test structures. Even though the lattice expansion of this structure is 2.85% which is less than the experimental value, the volume expansion is very close to the experimental one. In this case, the volume expansion is 11.79% while the experiment shows 11.15%. Hence, it can be thought of that any of the two structures may be possible to exist. The reason is that the experiment was done for limited time and the maximum time was 2h only. Based on the energetics, it can be inferred that if more time was given, tetrahedral sites might be occupied and these phases of Pd-H systems could be detected. So far, our search based on the formation energy, the lattice constant, and the volume expansion, it shows that an octahedral site was occupied by H atom in the 1h experiment and three octahedral sites was occupied in the 2h experiment.

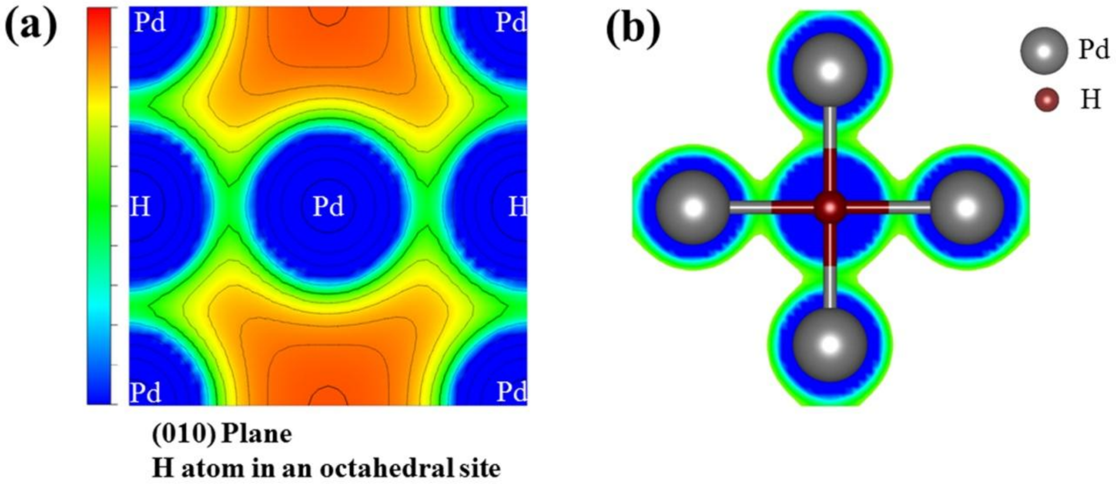

Figure 7.6 (a) 2D data display (color scale B-G-R) along (010) plane from charge density difference showing the bond between Pd and H atom in a Pd-H system and (b) a schematic of Pd-H-Pd bond in the crystal, where a H atom occupying an octahedral interstitial site.

Figure 7.6(a) shows a charge density difference plot in 2D for a hydrogen atom placed in an octahedral site O2. We see that the H atom makes a bond with neighbor Pd atoms and the

Pd-H-Pd bond is linear. From the corresponding dos plot for this structure as in Figure 7.7, it is seen that H s and p hybridize with Pd s, p and d. It is possible that H $1s^1$ may contribute making a covalent-like bond by sharing with Pd $5s^0$. From the contour lines of the 2D charge density difference plot, it may be realized that the Pd-H bond is partially covalent-like. The octahedral position occupied by H and hence the Pd-H-Pd linear bond in the structure contribute to the lattice and volume expansion. This structure is possible to form in 1h experiment time.

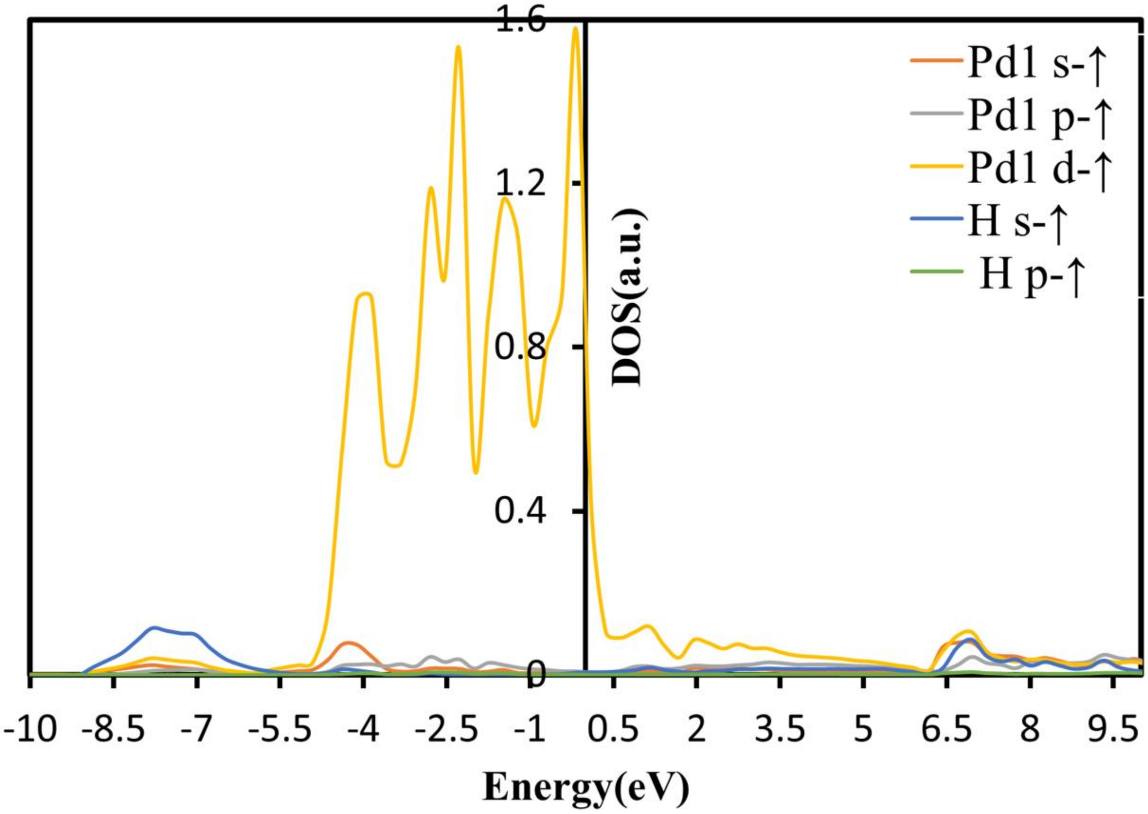

Figure 7.7 DOS plot for a Pd-H system with a H atom placed in an octahedral site O2.

For experiment time, longer than 1h, in the case of 2h, we have sorted out two possible occupations, which are three H atoms in three octahedral sites and two H atoms in two tetrahedral sites. The charge density difference plots in 2D for these two structures are displayed in figure 7.8 and 7.10 respectively. The figure 7.8 shows that three H atoms in three octahedral sites make linear bonds with Pd atoms while figure 7.10 shows that both H atoms in tetrahedral sites make non-linear bonds. From the dos plot in figure 7.9 we see that, all three H atoms have the same density of states and H s and p hybridize with the Pd s, p and d orbitals to make linear bonds in the structure. In figure 7.11, similar hybridization between H s, p and Pd s, p and d are also seen. The Pd-H-Pd bond angle, in this case, is 105°. In addition, the Pd-H bond length for the tetrahedral case is 1.81Å while that for three H atoms in octahedral sites is 2.05Å. This might be the reason that the overall lattice constant is less for the structure with H atoms in tetrahedral sites. Both of these structures can be candidates as a possible structure that forms in 2h experiment time. However, note that based on the formation energy, thermodynamically the tetrahedral sites T1 and T3 are more probable to be occupied by two H atoms than O1, O2 and O3 sites by three H atoms. There is a possibility that a phase transformation takes place from octahedral to tetrahedral sites. It is possible that due to the experimental time limitation, the transformation was not observed. However, it indicated that the any of the two choices is probable for H atoms to be absorbed by palladium crystal structure in 2h experiment time.

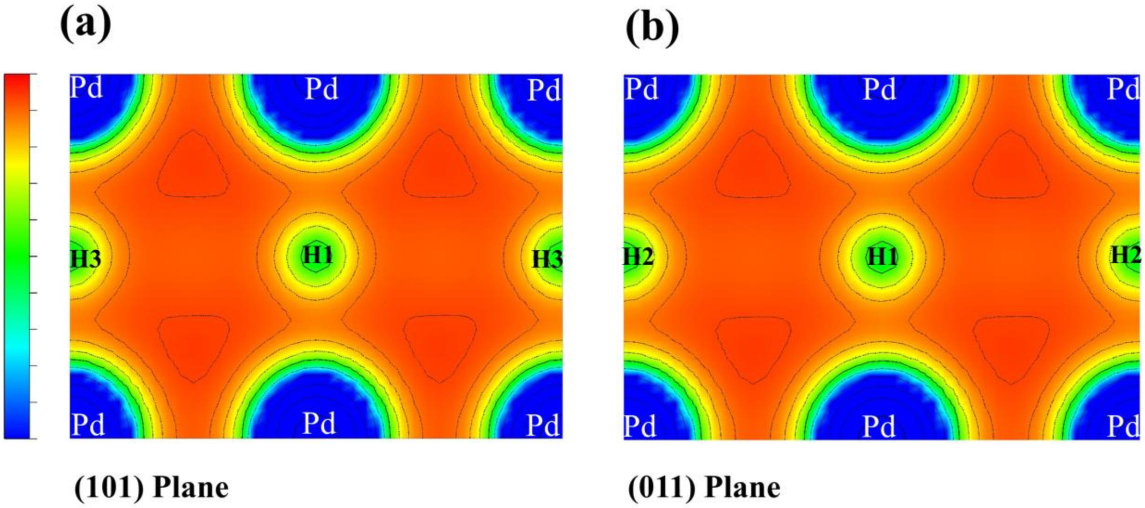

Three H atoms in three octahedral sites

Figure 7.8 Charge density difference plots in 2D (color scale B-G-R) for (a) H atoms labeled as H1 and H3 in two octahedral sites labeled as O1 and O3 in the plane (100) and, (b) H atoms H1 and H2 in sites O1 and O2 in the plane (011) as in figure 1 making bonds with neighboring Pd atoms.

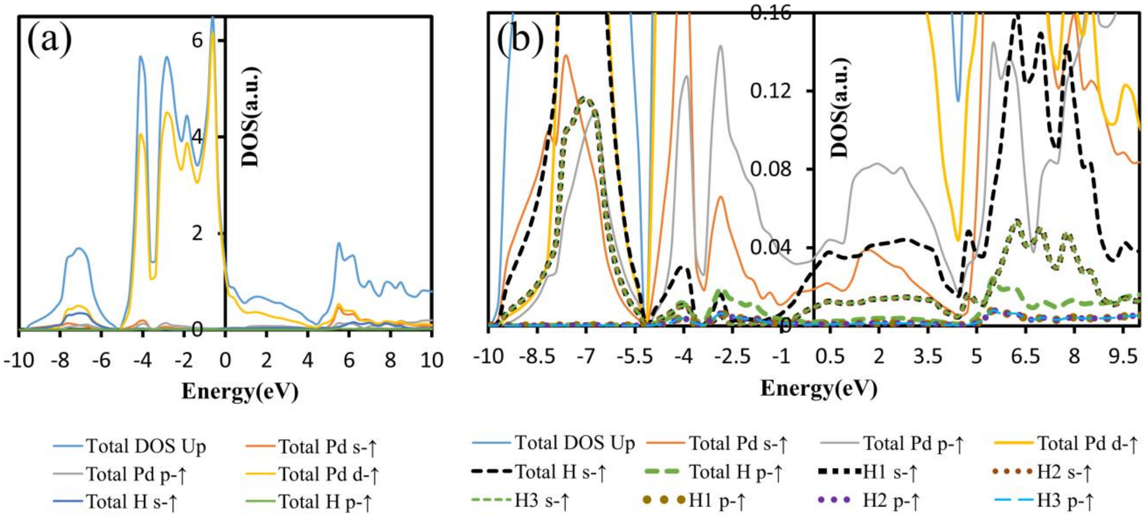

Figure 7.9 (a) DOS plot for a Pd-H system where three H atoms are placed in three octahedral sites O1, O2 and O3 and (b) total and partial dos of three H atoms in the system.

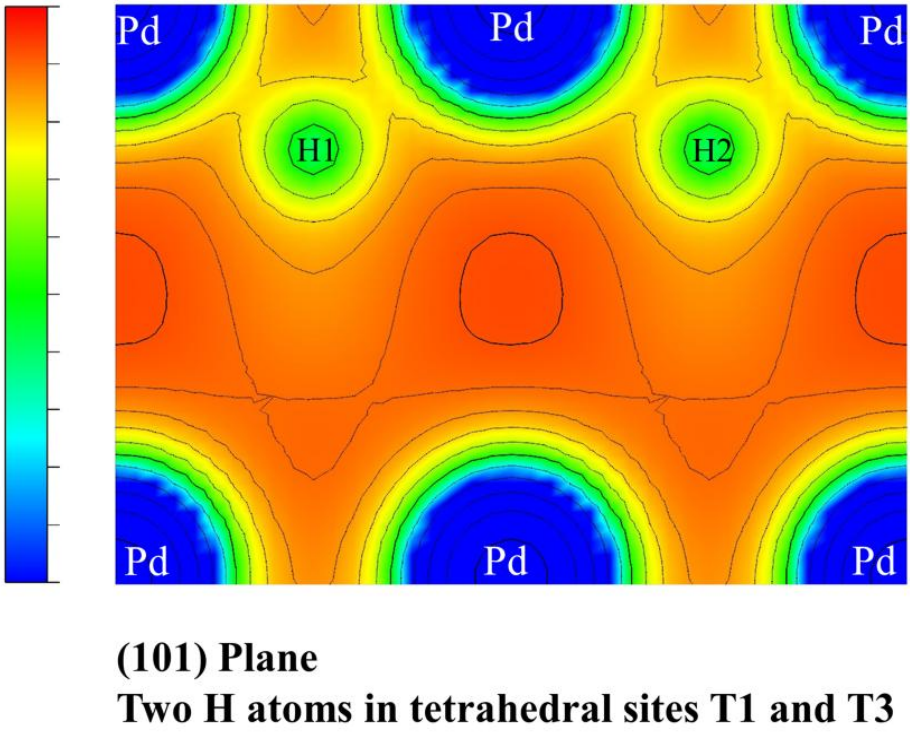

Figure 7.10 A charge density difference plot in 2D (color scale B-G-R) in (101) plane displaying two H atoms in two tetrahedral sites T1 and T3 as in figure 1(b) making bonds with Pd atoms.

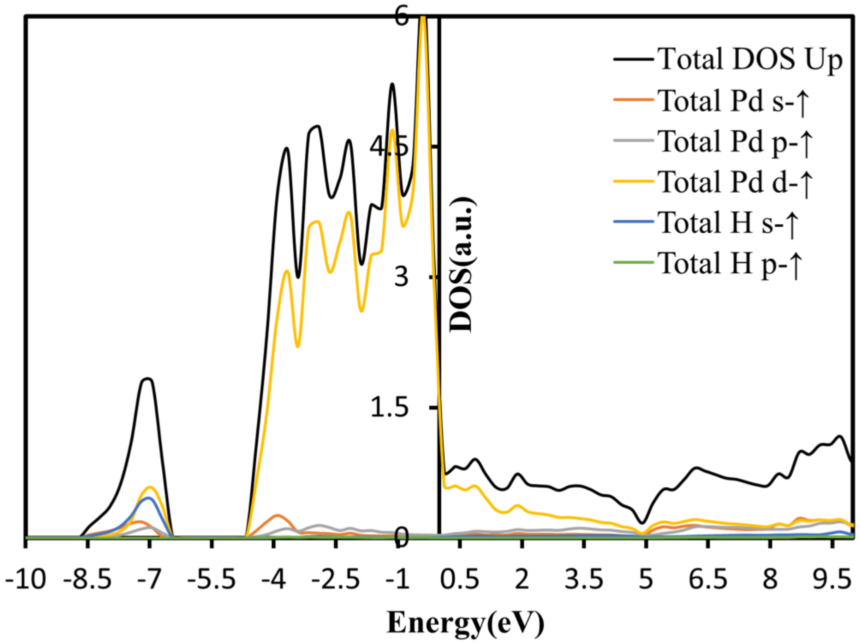

Figure 7.11 DOS plot for a Pd-H system where two H atoms are placed in T1 and T3 sites. Inset is the magnified view of a portion of the DOS plot.

7.4 Conclusions

We have developed a one-step method to synthesize Pd nanoparticles by an unconventional top-down synthesis approach. This paper demonstrates a novel way of hydrogen production from toluene and direct storage in plasma generated nanoparticles. Monodispersed Pd nanoparticles with a narrow particle size distribution were successfully synthesized by a plasma discharge between Pd electrodes in the cavitation field of toluene. The resulting Pd nanoparticles embedded in carbon are stabilized against agglomeration. With X-ray diffraction and high-resolution transmission electron microscopy measurements, it was found that particle size and lattice expansion increases with experiment time. The role of hydrogen induced lattice expansion of Pd is also addressed using the computational studies. Synthesis of nanoparticles using plasma discharge in appropriate solvent emphasizes the importance of adopting this methodology, which offers advantages, which include a rapid reaction rate and the ability to form very small nanoparticles with narrow size distribution.

Chapter 8

Ferromagnetism in graphene-like graphite nanosheets

8.1 Introduction

Rare-earth and transition metal free, environmental friendly magnets are desired for future magnetic applications. Synthesis of room temperature ferromagnets with only s and p electrons is of fundamental importance in research and may offer ample scope for new technological applications. Ferromagnetism in carbon-based materials is thus important but controversial since only s, p electrons are present and the magnetic signals are very small. It is also important for magnetic applications that the ferromagnetism (magnetic state) is stable at room temperature. There are several reports that confirm the existence of ferromagnetic order in impurity-free carbon materials [155-158]. Observed plausible ferromagnetism in graphene and graphitic materials is explained by lattice imperfection [155, 159] or spin ordering at graphene zigzag edges due to hydrogen termination [160-162]. Ferromagnetism is also observed in other forms of carbon, namely carbon nanofoam [163], polymerized fullerenes [164] and proton irradiated carbon films [165]. These observations suggest an inherent ferromagnetic behavior in carbon-based materials.

Here we present the studies on the preparation of graphene-like graphite nanosheets and its ferromagnetic properties. This paper will discuss the uncommon top-down synthesis route to produce multilayer graphene nanosheets. Experimental observation of ferromagnetic signal in bulk magnetizationn measurement was performed using a VSM at room temperature. To understand and explain the intrinsic origin of ferromagnetism in carbon-based materials, a systematic study of the magnetic impurity concentration in the sample is of primary importance and absolutely necessary. We have studied in detail different potential sources of impurities in our sample. The results appear to rule out the possible influence of ferromagnetic impurities in the observed ferromagnetism. Carbon-based magnetic materials can pave the way for the realization of rare-earth and transition metal-free magnets which could have potential applications in devices where traditional magnets are used.

8.2 Experimental method

In the present study, graphite nanosheets were synthesized by a top-down approach using plasma in toluene (Supplementary information I). Ultrasonication in toluene forms cavitations. The voltage between graphite electrodes (99%, metal basis) was kept at 3.5 kV. The collapse of cavitation between graphite electrodes in a strong electric field polarizes the π-electrons in toluene, and thus creates plasma by breaking chemical bonds. An intense strike of plasma on bulk graphite electrodes forms graphite nanosheets. This method has been previously discussed as a new route to synthesize various nanoparticles [6, 166].

Graphite nanosheets powder was dispersed in ethanol, dropped onto a carbon-coated copper grid and dried for the TEM investigation. The TEM (JEOL 1200 EX, operated at 120kV) observations allowed us to determine the overall morphology of the sample. HRTEM (Hitachi H-9500, operated at 300kV) was used to determine the crystal structure of the nanosheets. The crystal structure of nanosheets was also determined using XRD with monochromatic Cu K_α radiation (Bruker D8 diffractometer). The chemical composition of the nanosheets was analyzed using Energy Dispersive X-ray spectroscopy (EDX) linked with the TEM. Magnetic measurements of the sample were performed using a VSM (Micro sense-Model 10) at room temperature. Raman spectra were measured using a Raman spectrometer (LabRAM ARAMIS, Horiba scientific) equipped with He-Ne laser with a 633 nm excitation wavelength at an intensity of 5 mW. FTIR spectra were recorded by Thermo Nicolet 6700 FTIR Spectrometer using attenuated total reflectance (ATR) device.

8.2.1 Laser ablation-inductively coupled plasma-mass spectrometry analyses of potential ferromagnetic elements

The graphitic sample in powder form can’t be dissolved in nitric acid for liquid analyses by ICP-MS (inductively coupled plasma–mass spectrometry), hence the laser ablation (LA)-ICP-MS approach for solid sample analyses was adopted to analyze elements implicated in the magnetic characteristics [167-170]. The powder was deposited onto a glass slide by droplets of dispersed powder into ethanol, which was subsequently analyzed by LA-ICP-MS.

A UP-213 laser ablation system (New Wave, Freemont, CA), interfaced with a PerkinElmer/SCIEX ELAN DRC II (Sheldon, CT) ICP-MS system, was employed in this study. We used a 100 µm-diameter laser spot to vaporize a hole in the solid sample at a sub-micron depth for each laser pulse, and the vaporized elements from the hole were entrained by helium gas and analyzed with ICP–MS. This LA–ICP–MS approach can generate 2-D and 3-D maps of chemical distribution on any solid material at a spatial resolution of microns, and a concentration limit of sub-mg/kg [167-169]. Before laser ablation, the ICP-MS sensitivity was tuned to keep the ^{115}In signal response high, while maintaining the oxide ratio (^{156}CeO/^{140}Ce) and doubly-charged Ba^{2+}/Ba^{+} (70/140) less than 3%.

Helium was used as the carrier gas to transfer the laser-generated aerosol through a glass tee into the ICP-MS. At the same flow rate as helium (about 0.6 L/min), argon was used as the make-up gas to maintain the plasma for ICP-MS analyses. With the tee configuration, in addition to the solid signals from laser ablation swept into the ICP-MS by helium gas, the argon flow also took in liquid standards (2 µg/L each of ^{6}Li, ^{45}Sc, ^{115}In, and ^{209}Bi), which were continuously introduced into the ICP-MS and their responses were monitored, whether or not laser was fired and solid signals collected. Any potential signal-response change of solid signals, caused from ICP-MS sensitivity drift, was captured from the use of this liquid standard solution at constant concentrations; in this work, ^{45}Sc intensity was used for time-drift correction considering its mass proximity to the transition elements of interest.

During data acquisition, signal intensities (counts per second, CPS) were recorded for elements with a range of atomic mass, which include 9 major elements (^{23}Na, ^{24}Mg, ^{27}Al, ^{28}Si, ^{39}K, ^{43}Ca, ^{47}Ti, ^{55}Mn, and ^{57}Fe) used for concentration quantification [171] and transition elements of interest (^{51}V, ^{53}Cr, ^{59}Co, ^{60}Ni, ^{63}Cu, ^{66}Zn, and ^{69}Ga). Note that although it is the isotope that is measured by ICP-MS, the resultant concentration is for the element. This is because the concentration of each element, instead of isotope, is used for the reference materials, and the same isotope is monitored in both samples and reference materials (Fig. 8.1).

To assess the background response of monitored elements to better quantify the trace amount of transition metals of graphitic powder on the glass slide, we first collected signals, without and with firing the laser, onto the air inside the sample chamber of laser ablation. Then we collected the signal response of monitored elements on the glass slide on which the graphitic powder would be deposited; laser ablation was conducted at 6 spots, with a spot size of 100 µm and a spacing of 1,000 µm.

For NIST SRM (Standard Reference Material) glass samples, a combination of laser spot and pulse was used to consider their different concentrations of trace elements: 100 µm spot size and 10 pulse (100 µm/10 p), 100 µm /20 p, 150 µm /100 p, and 250 µm /100 p for SRM 610, 612, 614, and 616, respectively. For the graphitic and glass slide samples, 20 laser pulses were fired in each sampling spot. The sampling spots were spaced 1 mm apart to better account for statistical measurements.

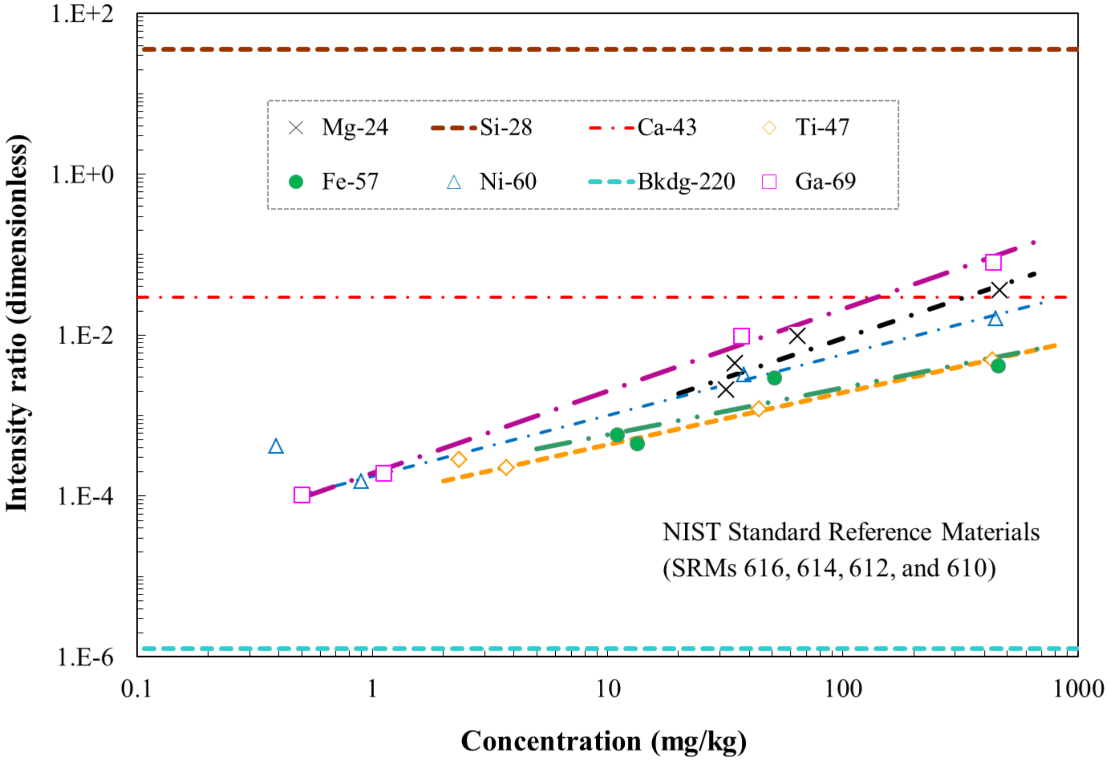

Figure 8.1 Intensity ratio of monitored element normalized on Al-27 to show the linearity, as well as the detection limit, of the four NIST SRMs with different concentrations.

Concentrations of Na, Al, Si, and Ca are basically the same for the four reference materials (NIST SRM 610, 612, 614, and 616), which additionally contain sixty-one trace elements in a glass matrix, in concentrations reported by Kurosawa et al [172]. Figure 8.1 shows the standard curves for some elements of interest. Linearity can be observed for most of the elements.

For the elemental analyses of graphitic powder, initially five spots were collected by laser firing at 100 µm laser spot size and 20 pulses, and then 10 spots were measured at100 µm laser spot size and 40 pulses; an increased laser pulse (and hence sampled mass) was to optimize the detection limit of trace amount of ferromagnetic elements. Then in an area not sampled before, a 4 mm × 4 mm grid-of-spot mapping routine was performed, with 100 µm laser spot size and 500 µm spacing between spots, resulting in a total of 81 spots for this grid size; each spot was fired with 80 laser pulses for sampling.

The constant-sum calibration method was used to quantify the concentration of transitional elements in both glass slide and graphitic samples [171]. The constant-sum method uses the sum of 100% of nine major sample constituents (oxides) as a normalization standard and therefore does not require the choice of an internal standard.

Table 4 Concentration of elements in graphite powder.

Fe mg/kg	**Co mg/kg**	**Ni mg/kg**	**Ti mg/kg**	**Cr mg/kg**	**Cu mg/kg**	**Zn mg/kg**	**Va mg/kg**	**Ga mg/kg**
2.0	0.1	0.5	1.0	1.0	1.0	1.0	0.5	0.1

We collected the two background signals by firing the laser into the air and present the elemental composition data by subtracting this averaged background. It is found that iron concentration in the graphitic sample is around 2 mg/kg, which is the detection limit of the analytical approach for low-mass elements. Such no detection of iron on the graphitic sample is also shown in Fig. 8.2, with the overlapping signal responses between a glass slide and graphitic sample on a glass slide.

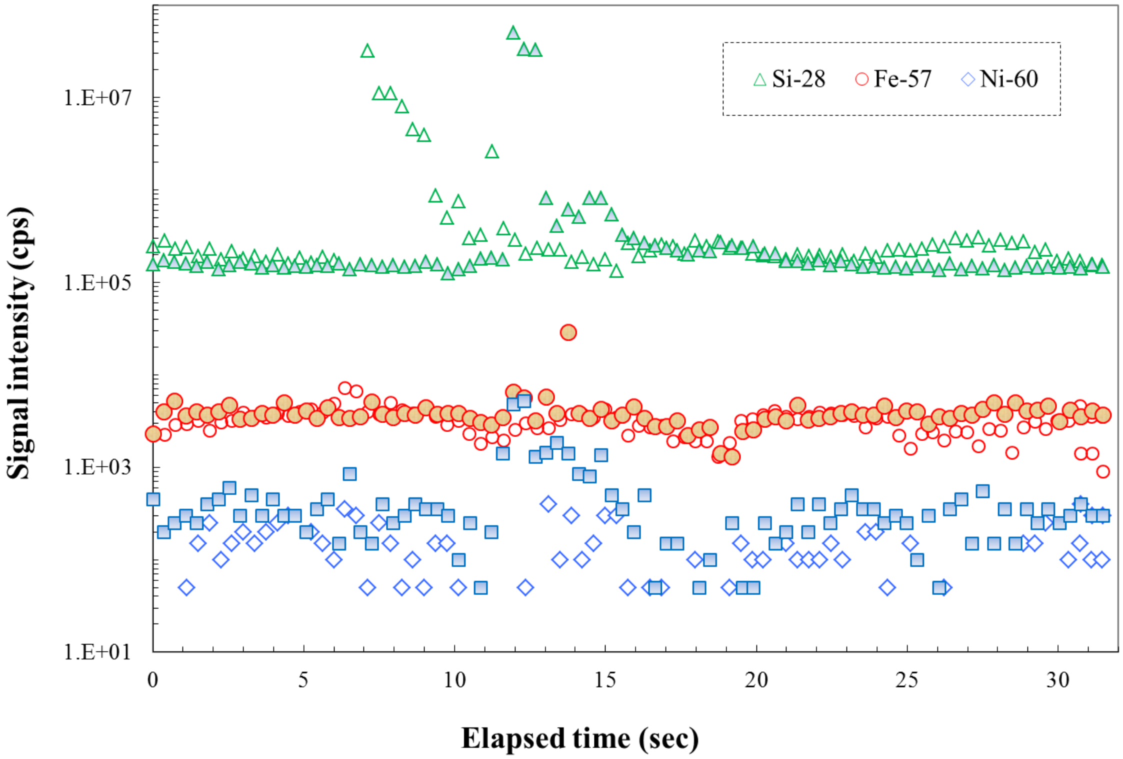

Figure 8.2 Signal intensity of representative elements for glass slide (non-filled symbol) and graphitic particles on glass slide (partially-filled symbol) samples; both samples were fired for 20 pulses at 100 µm. Note that different solid-signal appearance between glass slide (at about 8 sec) and graphitic powder on a glass slide (at about 11 sec) is just from different laser firing time.

That fairly low amount (at about 20 mg/kg), before background correction, of iron is from the glass slide, because of the following reasons: (1) a total of 80 laser pulses for the graphitic sample was used, which is expected to dig a hole at about 40 µm; (2) we used 100 µm laser spot size for all the measurement of graphitic samples. Both the sampling depth and area are almost as large as the graphitic particles (Fig. 8.3); therefore, our analytical approach is sampling the glass area, as confirmed from microscopic pictures.

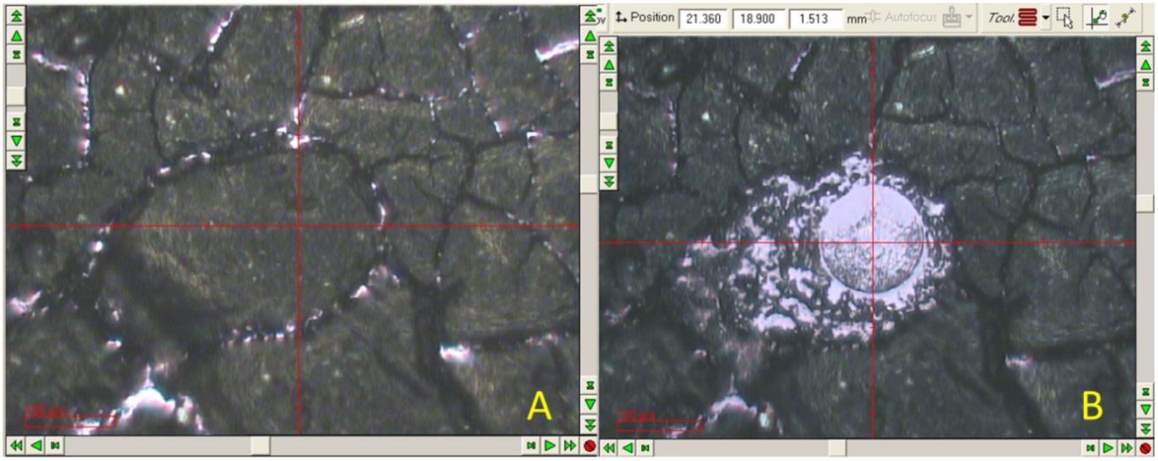

Figure 8.3 Images of graphitic particles before (A) and after (B) laser ablation at 100 µm and 20 pulses.

8.3 Results and discussion

8.3.1 Morphology of multilayer graphene nanosheets

Figure 8.4(a) shows the bright field TEM image of a suspended graphite nanosheet on a lacey carbon grid. The central part of the nanosheet looks uniform, featureless, and almost flat. There is a variation in thickness at the edges, and the nanosheet appears to have several folds. These nanosheets tend to bend and their edges tend to roll easily [173, 174]. Irregularly shaped nanosheets of lateral sizes up to 5000 nm are transparent to an electron beam. Figure 8.4(b) shows electron diffraction pattern of the nanosheet. The pattern appears as typical six-fold symmetry expected for graphite/graphene [173, 175, 176]. Diffraction spots are indexed using Miller – Bravais indices along the [001] zone axis.

Edges provide a clear high-resolution transmission electron microscopy (HRTEM) signature for the number of graphene layers since it is locally parallel to an electron beam [173]. Figure 8.4(c) and 8.4(d) shows a HRTEM image of edges of two multilayer graphene nanosheets. The numbers of graphene layers in the two sheets are 10 and 34, respectively. The lattice spacing of graphene layers as measured from Figure 8.4(c) and Figure 8.4(d) is 0.34 nm. The known characteristic interplanar spacing of (002) graphite is 0.34 nm which permits the unambiguous identification of the material [177]. Hence the thickness of these nanosheets due to interplanar spacing of 0.34 nm is 3.40 nm and 11.56 nm, respectively.

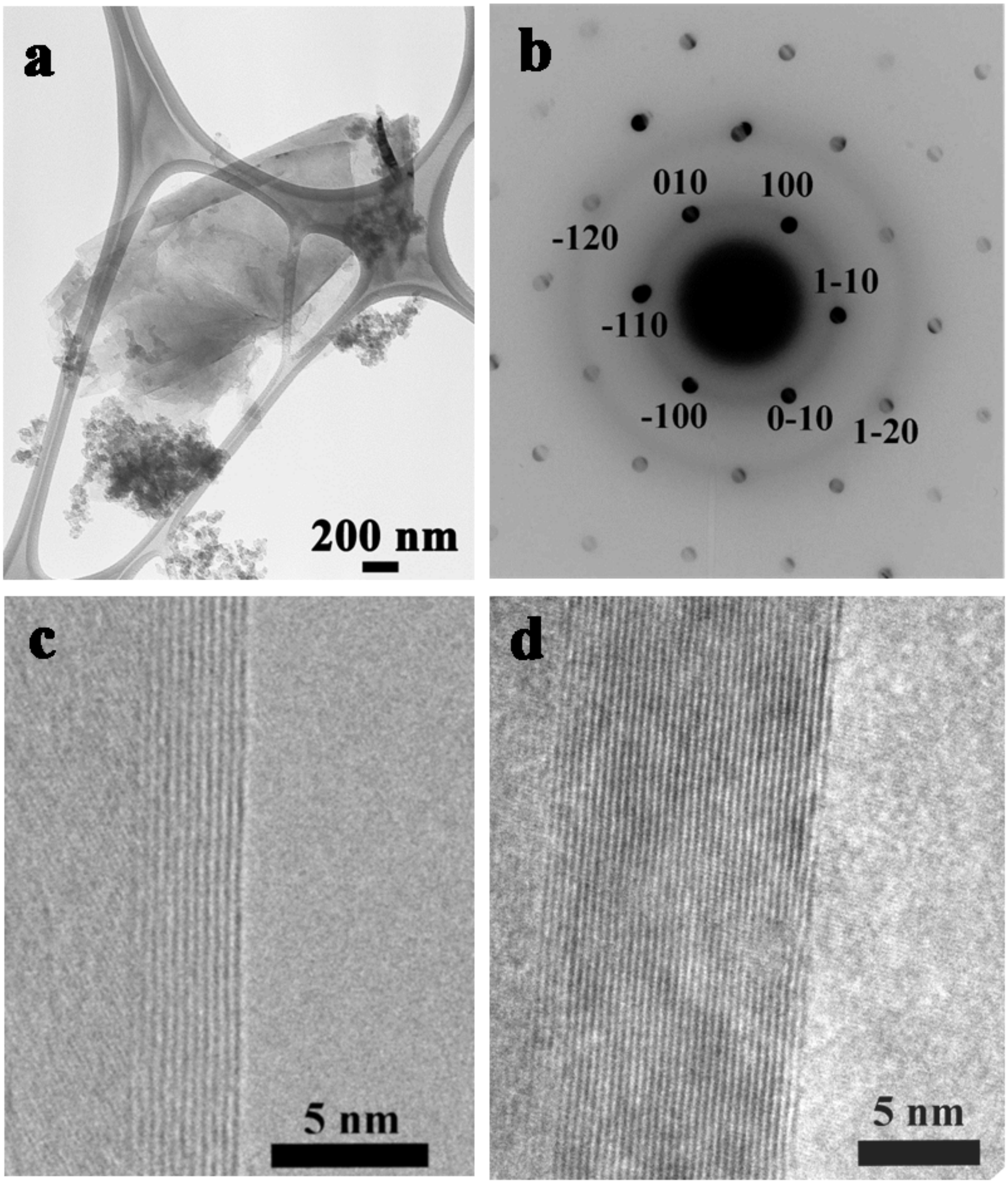

Figure 8.4 Electron microscopy of graphite nanosheets (a) Bright field TEM image of a graphite nanosheet, (b) electron diffraction image shows that the graphite nanosheet is a single crystal and (c),(d) HRTEM images of graphene layers of folded edges of graphite nanosheet. The number of graphene layers is 10 (Figure 1(c)) and 34 (Figure 1(d)).

8.3.2 Structure and magnetic properties of multilayer graphene nanosheets

The XRD pattern of the synthesized sample along with pristine graphite electrode powder is shown in Figure 8.5. The peak at a 2θ value of 26.48° is assigned as (002) diffraction line of hexagonal closed packed (hcp) graphite [177]. By comparing XRD pattern of pristine graphite to synthesized powder, it appears that only one peak corresponding to (002) remains after synthesis. The relative intensity of (002) of pristine graphite is very high as compared to synthesized powder. Therefore, it suggests that there must be cleavage or exfoliation happening along (002) in the crystal structure.

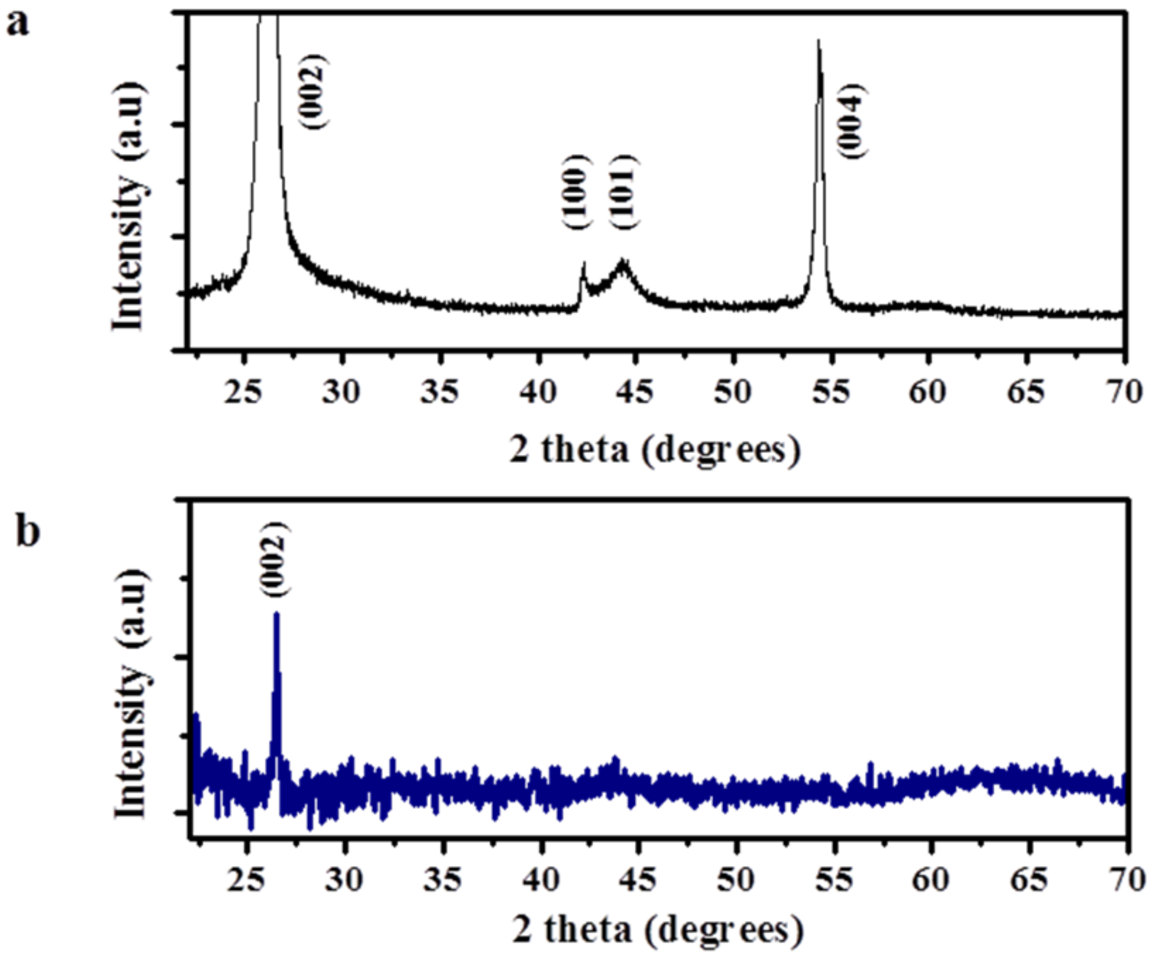

Figure 8.5 XRD pattern of (a) the pristine graphite electrode in powder form and (b) the synthesized graphite nanosheets after 1 hour of reaction time.

Figure 8.6(a) shows the magnetization hysteresis loop of graphite nanosheets at room temperature after subtraction of the diamagnetic background of the sample holder. Ferromagnetic like hysteresis loops are observed at room temperature. The magnetization of the synthesized sample is 5×10^{-2} A m ^{2} kg^{-1}. The remanence magnetization and coercivity is and 5.5×10^{-3} A m ^{2} kg^{-1} and 5.97 kA m^{-1}, respectively (Figure 6(a) inset). Since the observed magnetism in the sample can be due to different origins, the most important point will be to eliminate any ferromagnetic contribution from magnetic impurities in the synthesized powder, particularly Fe. Therefore we analyzed our sample by LA-ICP-MS [178]. We like to note that in our samples Fe is the main magnetic impurity with a concentration of 2 mg kg^{-1}, which is the detection limit of LA-ICP-MS for Fe on a solid sample. All other magnetic metallic impurities are much below 2 mg kg^{-1} (Supplementary information II). The magnetization at 318 kA m^{-1} as shown in Figure 8.6(a) does not show a correlation with the measured Fe concentration. The bulk magnetization of Fe is 220 A m ^{2} kg^{-1}. Assuming all the measured Fe impurity in the sample is ferromagnetic, a simple estimate would give a magnetization of 4.4×10^{-4} A m ^{2} kg^{-1} [179]. The magnetization of the synthesized sample is 5×10^{-2} A m ^{2} kg^{-1}, which is two orders of magnitude higher than an impurity of Fe would give. This magnitude might also be the lower limit due to the proportion of nonmagnetic phase (carbon matrix). It is also the reason for a slight diamagnetic signal in Figure 8.6. The diamagnetic carbon phase has a detrimental effect on the saturation magnetization per unit mass of the synthesized sample. Figure 8.6(b) shows the magnetization hysteresis loop of graphite nanosheets at room temperature after 135 days from synthesis. Ferromagnetism appears to be stable at room temperature. Thereby carbon-based environment-friendly magnets could be considered as potential candidates for magnetic application such as devices with spintronic properties [159, 180, 181].

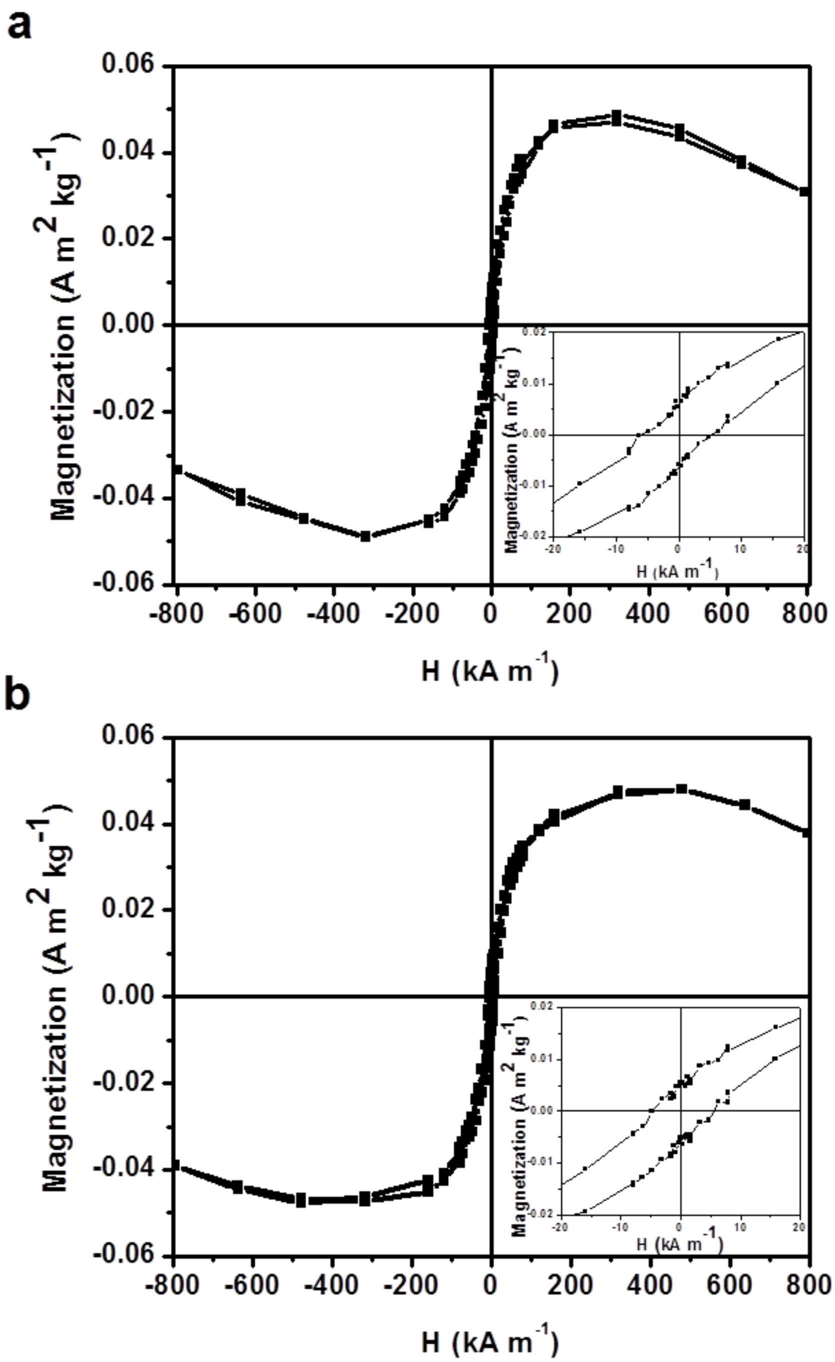

Figure 8.6 Magnetic hysteresis loops. Magnetization hysteresis loops at 300 K in the range of -796 kA m^{-1} < H < 796 kA m^{-1} after the background correction of (a) as-synthesized sample, M_s = 0.05 A m^2 kg^{-1} and (b) after 135 days, M_s = 0.05 A m^2 kg^{-1}. The inset at the bottom right of both figures shows the expanded view of the magnetic hysteresis curves in the low field region.

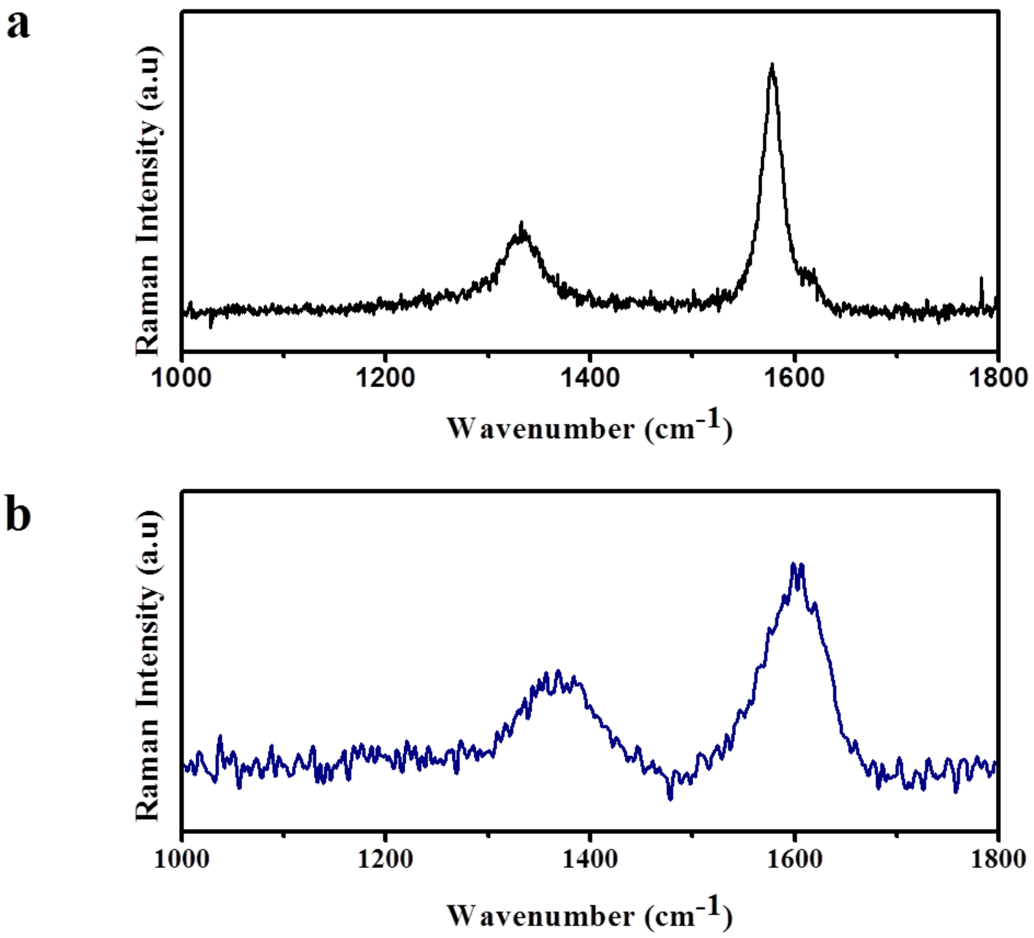

Figure 8.7 Raman spectra of (a) pristine graphite powder and (b) synthesized graphite nanosheet.

One possible source of ferromagnetic ordering might be due to lattice disorder. We believe the source of magnetic ordering in our samples might be lattice disorder caused by intense plasma striking on bulk graphite electrodes which lead to the formation of graphitic nanosheets. This plasma strike may cleave or exfoliate along (002) in the crystal which might introduce defects. The measurements with the VSM indeed show clear signs of ferromagnetic ordering after cavitation plasma synthesis of graphite nanosheets. This result further validates the claims that magnetic ordering exists in carbon structure without the influence of magnetic impurities.

To measure the degree of disorder in synthesized sample, Raman spectroscopy was performed on pristine graphite powder and synthesized sample. Figures 8.7(a) and 8.7(b) show Raman spectra of pristine graphite and synthesized sample. The Raman spectra of pristine graphite show two peaks, the G peak around 1580 cm^{-1} and the D peak around 1350 cm^{-1}. Ideally, perfect graphite without a disorder would only have the G peak [182, 183]. The Raman spectrum of synthesized sample has two peaks, the G peak around 1602 cm^{-1} and the D peak around 1370 cm^{-1}. The G and D mode of synthesized sample appears to be broader compared to the pristine graphite after an hour of synthesis. In comparison to the pristine graphite, I (D) / I (G) ratio of synthesized sample also increased from 0.27 to 0.43. The high-intensity ratio and broad peaks suggest an increase in the degree of disorder in the sample [184]. The peak shift of G band from 1580 cm^{-1} to 1602 cm^{-1} suggests an evolution of phase from graphite to nanographite [183].

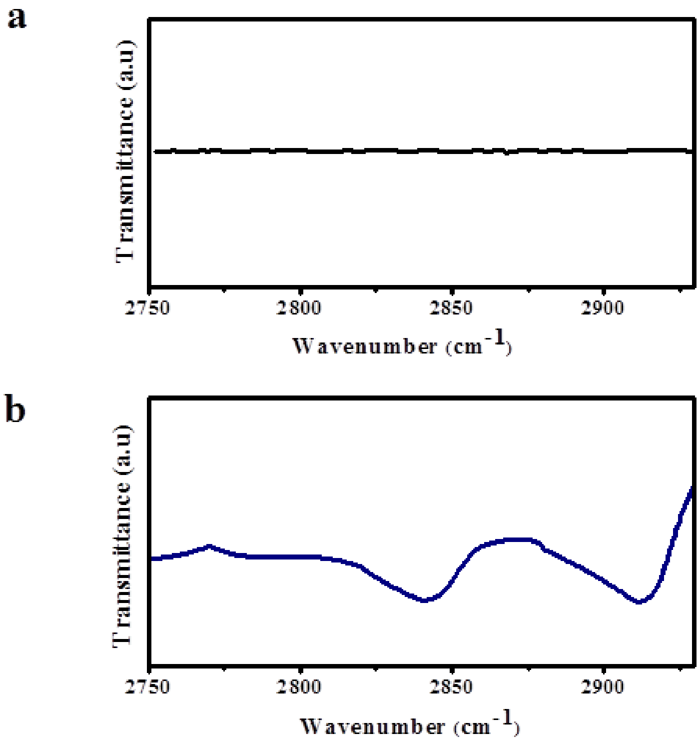

Figure 8.8 Hydrogenation of graphite nanosheets. FTIR spectra of (a) pristine graphite powder and (b) synthesized graphite nanosheets showing C-H bonding.

Another possible source of ferromagnetic ordering can be due to spin ordering at graphite edges because of hydrogen termination. An IR spectrum of the synthesized sample in Figure 8.8(b) clearly shows aliphatic C-H stretching bands in the 2850 cm^{-1} – 2950 cm^{-1} region [185, 186]. In pristine graphite powder, C-H stretching bands were not observed as shown in Figure 8.8(a). Several observations predict that the origin of magnetic ordering to different sources, such as the mixture of sp^2 and sp^3 bonds[187], defects [159, 180, 188, 189], spontaneous magnetization due to zigzag edges [181, 190, 191] and spontaneous magnetization in hydrogenated graphite due to mono and dehydrogenated carbon atoms [192]. We believe that ferromagnetic ordering in our sample can be a cumulative effect of the lattice disorder and hydrogenation of graphite nanosheets at the edges.

8.4 Conclusions

In conclusion, we report cost-effective synthesis and observation of ferromagnetic order in graphite nanosheets. Graphite nanosheets approximately 3-12 nm thick and up to approximately 5000 nm in lateral size were synthesized by plasma in ultrasonically cavitated toluene. The preliminary measurement of hysteresis loops using VSM indicates the ferromagnetic ordering in graphite nanosheets at room temperature. The magnetization and coercivity of the synthesized sample is 5×10^{-2} A m^{2} kg^{-1} and 5.97 kA m^{-1}, respectively. We have consistently observed the strong ferromagnetic signal from several batches of graphite nanosheet samples. Thus, it does commend that the source of ferromagnetic order is of intrinsic origin rather than due to ferromagnetic impurities, as confirmed by LA-ICP-MS analyses for potential ferromagnetic elements. Room temperature ferromagnetism in graphite nanosheets is likely due to lattice disorder and hydrogenation at edges of nanosheets.

Chapter 9

Synthesis and characterization of GdC_2 nanoparticles

9.1 Introduction

Gadolinium (Gd) and its compounds are widely used in technological applications ranging from phosphors [193], contrast agents in magnetic resonance imaging (MRI) [194], room temperature refrigeration [195], neutron detection [196], radioactive shielding and control rods in the nuclear industry [197]. Among all these applications, Gd is a promising candidate as neutron capture therapy (NCT) agent and has been receiving wide attention due to its highest neutron cross-section (255,000 barns), which is around 65 times larger compared to boron thermal neutron cross-section [198-200]. Gd is already used as MRI contrast enhancing agent in clinical investigations. The application of MRI and neutron capture therapy could be performed simultaneously which might lead to better diagnosis and treatment planning [201]. GdC_2 nanoparticles have been proposed as a better candidate for application in mammography screening in comparison to Gd and Gd_2O_3 nanoparticles [202].

Thus, Gd-based nanoparticles are of current interest due to their magnetic properties and the potential enhancement that the nanoscale or nanocomposite materials may exhibit due to their finite size and surface-interface effects. Magnetic properties of bulk gadolinium are of great interest to researchers and have been studied extensively [203]. However, to date, only one literature have reported magnetic properties of bulk GdC_2 [204] and two literatures has reported magnetic properties of GdC_2 nanoparticles with a mixed phases such as Gd/GdC_2 [205] and Gd_2C_3/GdC_2 [206]. Rare earth nanoparticles such as Gd have a high surface to volume ratio and are very reactive in nature. Synthesis of single phase nanoparticles is thus challenging and it results into mixed phase nanoparticles [205-209]. This limits further characterization of physical properties of these phases.

In this paper, we describe the synthesis of single phase GdC_2 nanoparticles using cavitation plasma and their structural and magnetic characterization. Synthesis of nanoparticles using plasma offers the advantages of simplicity, ease of scale-up, and the possibilities of size control.GdC_2 nanoparticles have a tetragonal crystal structure. The paramagnetic properties of the GdC_2 are also reported.

9.2 Experimental method

Figure 9.1 shows a schematic diagram of the experimental apparatus. Gd nanoparticles are synthesized using a facile method in toluene (Sigma Aldrich, anhydrous 99.8%) by the plasma generated between two Gd electrodes due to cavitations. Two Gd electrodes (Alfa Aesar, 0.62 mm in diameter, 99.9% REO) were inserted 0.5 mm apart from each other beneath the bottom of the ultrasonic horn. The distance between the electrodes and the bottom of the horn was kept constant at 10 mm. During the ultrasonic irradiation, the voltage on the electrodes was kept at 4.1 kV using a constant voltage power supply. A glass vessel filled with ice water was underneath and an Argon gas flow was directed into the closed geometry containing toluene to maintain an inert atmosphere.

Ultrasound in liquid media can generate acoustic cavitations, which is the formation and implosive collapse of bubbles. The collapse of such bubbles creates hot spots with temperatures as high as 5000 K and pressures up to 800 atmospheres [56, 83]. When cavitation bubbles are between the Gd electrodes, the applied electric field polarizes the π-electrons in toluene thus breaking chemical bonds during generation of plasma. Dissociation of toluene leads to free radicals (C atoms / C^+ ions) [84, 85]. High-temperature plasma between Gd electrodes forms Gd vapor. This vapor reacted with carbon forming quasi-liquid GdC_2 nanoparticles. Thereafter rapid quenching leads to form stable nanoparticles. Metals such as rare earth and transition elements are used as a catalyst for graphitization [91, 210]. These nanoparticles may thus play a role of catalyst. During quenching, cooling goes on from surface to the center of the nanoparticle and hence the graphitization initiates at the surface and progress until saturation which leads to carbon shell of the core GdC_2 nanoparticles. However, without ultrasonic irradiation, no plasma was generated with currently used power supply. The plasma was stable during the experiment and hence the positions of the electrodes were fixed throughout the synthesis. The synthesis of nanoparticles was continued for an hour. The liquid turned uniformly black, nanoparticles dispersed in the toluene were later separated by centrifugation, washed with toluene and dried in an oven at 318 K. In our recent work, we have demonstrated this method as a new route to synthesize various nanoparticles [6, 48, 58].

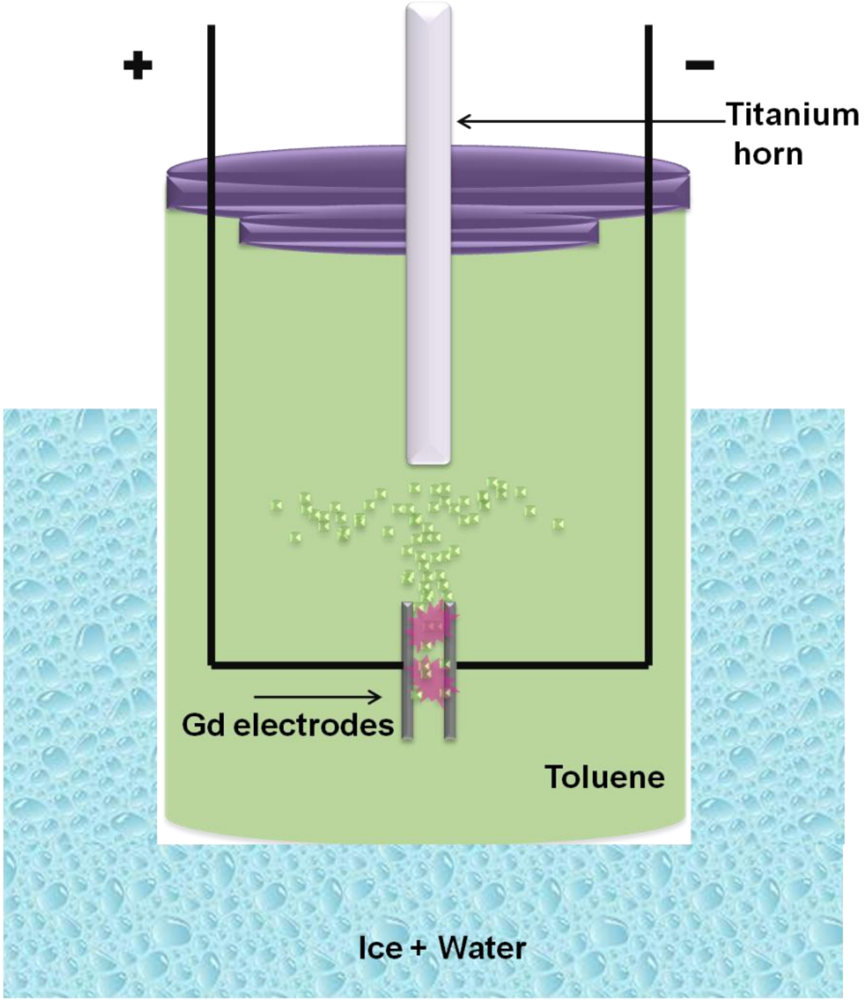

Figure 9.1Schematic of the experimental set up that is used to synthesize nanoparticles.

Nanoparticles were dispersed in toluene, dropped onto a carbon-coated copper grid and dried for the TEM investigation. The TEM (JEOL 1200 EX, operated at 120kV) observations allowed us to determine the overall morphology of the specimen. HRTEM (Hitachi H-9500, operated at 300kV) was used to determine the crystal structure of the nanoparticles. The crystal structure of nanoparticle powder was also determined using XRD with monochromatic Cu K_α radiation (Bruker D8 diffractometer). The chemical composition of the nanoparticles was analyzed using Energy Dispersive X-ray spectroscopy (EDX) linked with the TEM. Magnetic measurements of the powder sample were performed using a Quantum Design MPMS magnetometer (SQUID).

9.3 Results and discussion

9.3.1 Morphology of GdC_2 nanoparticles

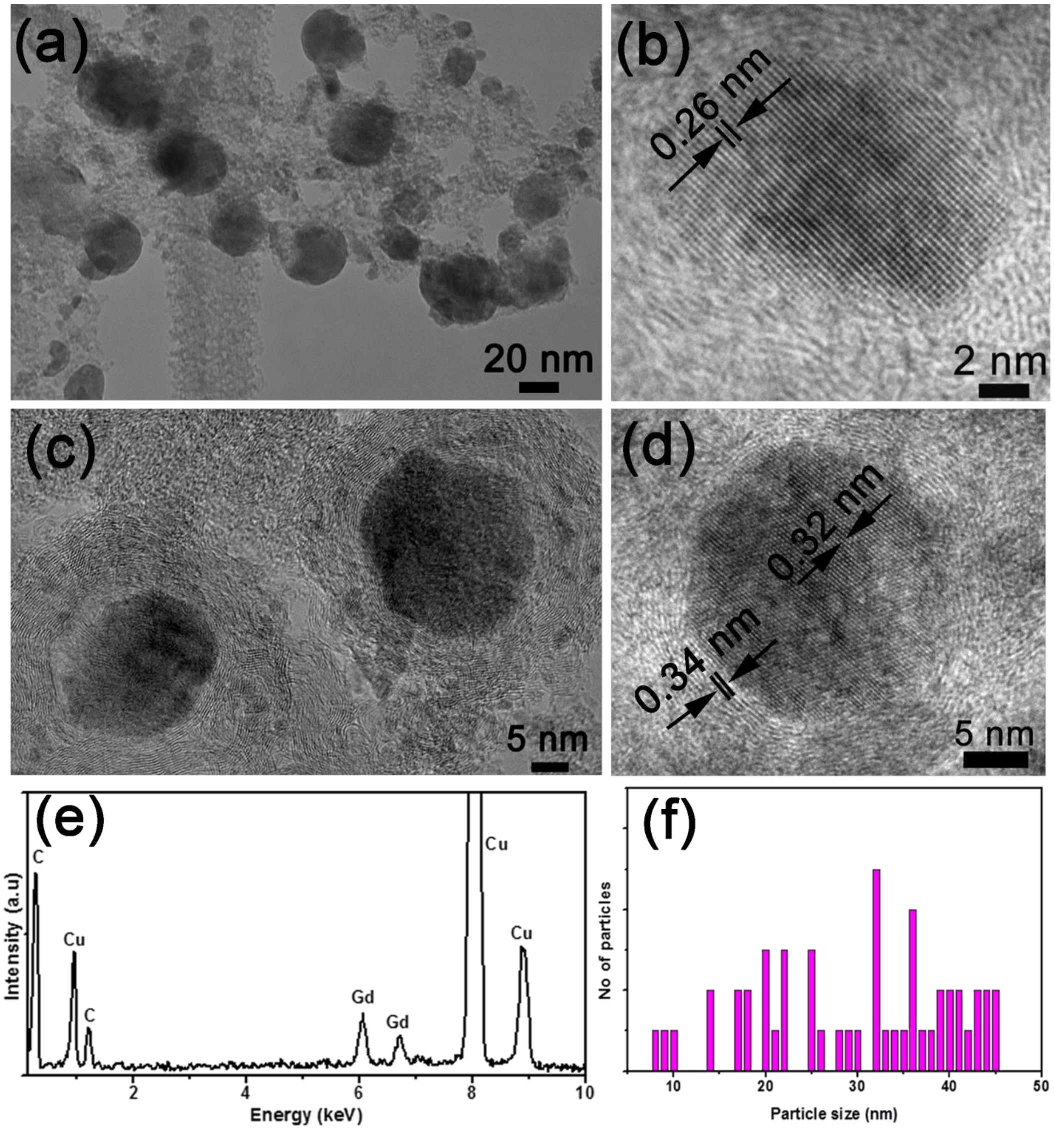

Figure 9.2 TEM image of GdC_2 nanoparticles, (b) HRTEM image of a single GdC_2 nanoparticle, HRTEM image of GdC_2 core – Carbon shell (c) nanoparticles and (d) nanoparticle, (e) EDX spectrum of the synthesized nanoparticles and (f) size distribution of nanoparticles.

Nanoparticles size and morphology were examined using TEM. TEM image (Figure 9.2(a)) shows nearly spherical GdC_2 nanoparticles with diameter of 8-45 nm along with amorphous carbon matrix. HRTEM (Figure 9.2(b)) shows a quasi-spherical particle of 14 nm in diameter. The spacing of lattice fringes from HRTEM and is 0.263 nm corresponding to (110) plane of tetragonal GdC_2 [PDF#01-073-2621]. Carbon encapsulated GdC_2 core nanoparticles were also observed using HRTEM as shown in Figure 9.2(c). Figure 9.2(d) shows that the carbon shells tightly surround the core nanoparticles, no obvious voids can be observed between the core and the shell. The shells consist of 10-11 layers (3.5 - 3.85 nm thick). The spacing of the lattice fringes of carbon shell is about 0.35 nm, which is close to that of the graphite (002) planes. The spacing of the lattice fringes of core is about 0.32 nm corresponding to (101) planes. Elemental compositions of the nanoparticles were analyzed using EDX. The EDX spectra of nanoparticles exposed to air exhibited the characteristic peaks associated with Gd and C which indicate that carbon shell and carbon matrix protects nanoparticles from environmental degradation, particularly oxidation. is shown in Figure 9.2(e). The presence of Cu is due to the TEM grid. Figure 9.2(f) shows relatively narrow particle size distribution with mean diameter of 30 nm.

9.3.2 Structure and magnetic properties of GdC_2 nanoparticles

XRD (Figure 9.3 (a)) analysis of the synthesized nanoparticles showed that it consists of a single phase GdC_2 which is uncommon due to the reactive nature of Gd [13-17]. Absence of Gd_2O_3 means that the GdC_2 phase appears to be stable in air. Structural assignment is based on XRD peaks. The peaks at 2θ values of 27.83°, 29.16°, 34.11°, 44.94°, 49.02°, 50.01°, and 57.18° are assigned as (101), (002) , (110) , (112) , (200) , (103) , and (211) diffraction lines of tetragonal GdC_2 phase respectively (PDF: 01-073-2621). No evidence was observed for Gd_2C_3, Gd_2C, Gd_2O_3 phases, or of Gd crystallites in XRD.

Specific magnetization (M) has been determined by applying a magnetic field (H) in the ± 5T range for temperatures from 10 to 300K. Figure 9.3 (b) shows magnetization data as a function of H for temperature 10, 50, 300 K. Paramagnetic response of the powder GdC_2 sample

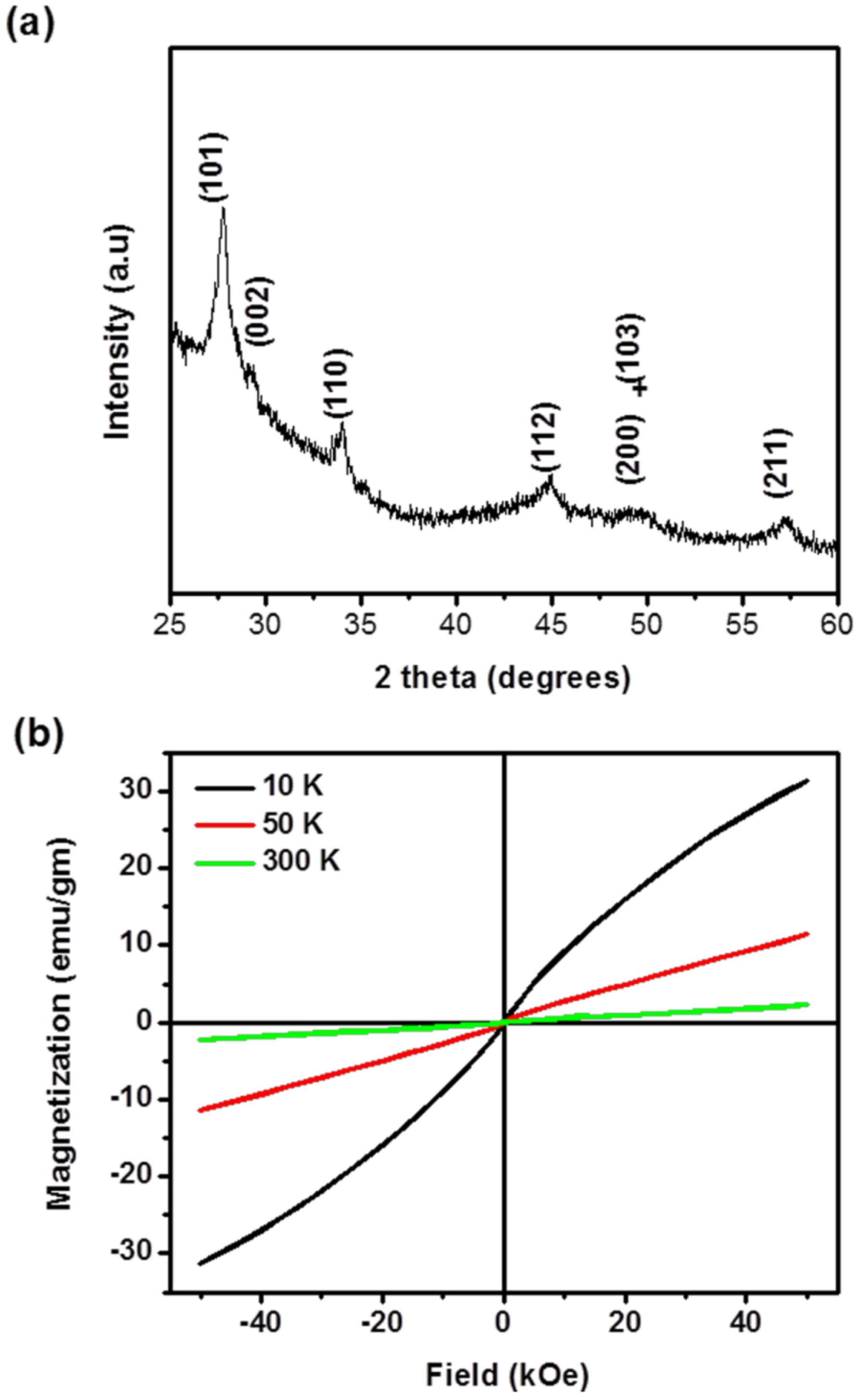

Figure 9.3 (a) XRD pattern of the synthesized nanoparticles and (b) Magnetization vs field of the synthesized nanoparticles at 10, 50 and 300 K.

is apparent. Bulk GdC_2 has an antiferromagnetic transition at 42 K [12]. From the TEM observations, the size of GdC_2 particles is on the order of 50 nm or less. Since their moments are essentially isolated and uncoupled an antiferromagnetic transition temperature for GdC_2 at 42K is not observed [12, 14]. The effect of strong external magnetic fields in aligning the moments of a paramagnet material is small compared to the disordering effect of thermal energy at room temperature. The effect of an increase in temperature is to increase the randomizing effect of thermal agitations and therefore to decrease the magnetization as shown in Figure 9.3 (b). The diamagnetic contribution of carbon will slightly decrease the specific magnetization of the synthesized nanoparticles.

9.4 Conclusions

In conclusion, this is the first report on magnetic properties of single phase GdC_2 nanoparticles. GdC_2 nanoparticles were synthesized using an advanced and cost effective method by plasma due to ultrasonication in toluene. The crystal structure and magnetic properties of the synthesized nanoparticles were studied. XRD and HRTEM results indicate that a single phase of GdC_2 is formed, as opposed to a mixture of gadolinium carbides and gadolinium oxides that are usually produced by conventional arc discharge methods. Magnetic properties of GdC_2 nanoparticles have been studied using SQUID which shows paramagnetic behavior. This method could also be extended for the synthesis of different metal nanoparticles if appropriate electrodes and solvents are selected.

Chapter 10

Summary and conclusions

Magnetic nanoparticles exhibit unique properties leading to diverse applications in the areas of magnetic data storage, magnetic fluids, drug delivery, hyperthermia, photothermal therapy and magnetic resonance imaging (MRI). In order to use these nanoparticles for in vivo or in vitro biomedical applications such as MRI contrast enhancement, the combined properties of high magnetic saturation, stability, biocompatibility, and interactive functions at the surface are essentially required. Carbon-encapsulated magnetic metal nanoparticles may offer novel properties arising from the core–shell structure due to the interfacial interaction between magnetic and dielectric layers. Carbon coatings can endow these magnetic nanoparticles with biocompatibility, stability in many organic and inorganic media, and protection from agglomeration and retain their intrinsic magnetic properties. Therefore, these multifunction core-shell nanoparticles are interesting candidates for fundamentals science and their potential applications.

This dissertation focuses on exploring the synthesis method to develop nanostructured materials including core-shell nanoparticles and investigates their structural and magnetic properties. Nanomaterials were synthesized by a plasma discharge between desired metal electrodes in the cavitation field of organic solvent. Multifunctional core-shell magnetic nanoparticles of 3d transition elements (Fe, Ni) and bimetallic (FeNi) were synthesized by varying experimental conditions. The phase, crystallinity and the magnetic properties of the materials synthesized were found to be dependent on experimental reaction parameters such as different solvents, electrodes, spacing between electrodes, applied voltage, experiment time and high-temperature annealing.

Carbon-encapsulated Fe nanoparticles were synthesized by plasma due to ultrasonication in toluene. Fe nanoparticles of diameter 7-115 nm are encapsulated by 7-8 nm thick carbon layers. SAED and XRD results indicate that all carbon coated metal nanoparticles are elemental rather than metal carbides, which are usually produced by conventional arc or plasma discharge method. The Fe nanoparticles have body-centered cubic (bcc) crystal structure. Magnetic measurement from the hysteresis loops indicates ferromagnetic properties of these materials. The saturation magnetization of synthesized and annealed nanoparticles is 9 emu/g and 24 emu/g at room temperature.

The effect of thermal annealing on the synthesized core-shell nanoparticles leads to change in particle size, structure, and magnetic properties. Carbon-encapsulated Fe nanoparticles are biologically friendly and were developed for high-performance Magnetic Resonance Imaging (MRI) contrast enhancement. Biocompatible hybrid composite of Fe core – C shell nanoparticles evaluated as negative MRI contrast agents display remarkably high transverse relaxivity (r_2) of 70 $mM^{-1}S^{-1}$ at 7T.

Ni nanoparticles were synthesized by plasma discharge method in toluene using Ni electrodes. The electrode spacing between Ni was varied and the effect on phase, crystallinity and magnetic properties was investigated. The crystal structure and crystalline quality of nanoparticle change from hcp and good to fcc and amorphization. HRTEM images showed carbon coated Ni nanoparticles. The magnetic measurement reveals superparamagnetic properties. The saturation magnetization (Ms) for the synthesized nanoparticles at 0.3 mm and 0.6 mm electrode spacing is 1.1 and 0.3 emu/g respectively.

$Fe_{20}Ni_{80}$ were synthesized using a versatile plasma discharge method. For $Fe_{20}Ni_{80}$ composition, the effect of solvent on morphology and the magnetic property was investigated. FeNi core of 15-820 nm in diameter were covered by 1-34 C shell in ethanol. FeNi core of 3-820 nm in diameter were covered by 1-60 C shell in toluene. The shell thickness is lower in particle synthesized by ethanol in comparison to toluene. Magnetization decreases from 3.6 emu/g when prepared in ethanol to 1.34 emu/g to toluene. The effect of applied voltage on magnetic property of nanoparticles was also investigated. The saturation magnetization decreases with increase in voltage (3.5 kV to 4.5 kV) from 1.34 emu/g to 0.75 emu/g.

For $Fe_{50}Ni_{50}$ composition, the effect of electrode spacing on the structure and the magnetic property was investigated while keeping the voltage constant. When the spacing of electrode was increased from 0.35 mm to 0.7 mm, hcp Ni transformed to fcc FeNi. It was observed that the crystalline nature of the nanoparticles was transformed to amorphous. It also leads to decrease in magnetization from 8.6 emu/g to 1.65 emu/g.

In the second part, the effect of varying voltage on the structure and the magnetic property was investigated while keeping constant electrode spacing. When the voltage was increased from 2.5 kV to 4.0 kV to 4.8 kV, hcp FeNi transformed to a mixture of fcc plus hcp FeNi and to fcc FeNi at the cost of crystallinity. The powder transforms from crystalline to amorphous. Magnetization also decreases with increase in voltage. The saturation magnetization at 2.5 kV, 4.0 kV and 4.8 kV is 9.7 emu/g, 2.95 emu/g, and 1.54 emu/g.

Monodispersed Pd nanoparticles with a narrow particle size distribution were also successfully synthesized by a plasma discharge for hydrogen storage. The particle size and lattice expansion increased with experiment time. The lattice constant Pd nanoparticles synthesized for 1 h and 2 h experiment times are 0.395 nm and 0.403 nm respectively. The lattice constant for pristine Pd is 0.389 nm. The increase in lattice constant for 1 h and 2 h experiment time are 0.0056 nm and 0.014 nm respectively. The lattice expansion is 1.44% and 3.60% respectively. Dilated lattices result in a volume expansion of 4.4 % and 11.15 % for 1 h and 2 h experiment time respectively. The role of hydrogen induced lattice expansion of Pd was investigated using density functional theory (DFT) studies and the results are in agreement with the experiment.

In addition to 3d transition magnetic materials, the magnetism of carbon-based ferromagnets of multilayer graphene nanosheets with only s and p electrons was investigated to understand and explain the intrinsic origin of ferromagnetism in the carbon-based material. Graphite nanosheets approximately 3-12 nm thick and up to approximately 5000 nm in lateral size were synthesized by plasma in ultrasonically cavitated toluene. Measurement of hysteresis loops using VSM indicates the ferromagnetic ordering in graphite nanosheets at room temperature. The saturation magnetization of 0.05 emu/g and coercivity of 75 Oe was measured at room temperature. The observed ferromagnetic order was due to intrinsic origin rather than ferromagnetic impurities as confirmed by laser ablation inductively coupled plasma mass spectrometry (LA-ICP-MS). Room temperature ferromagnetism in graphite nanosheets is likely due to lattice disorder and hydrogenation at edges of nanosheets.

Appendix A

Research accomplishments

Awards

- Scharff Award for research achievement, Department of Physics, UTA 2017
- Scharff Award for research achievement, Department of Physics, UTA 2014
- DOE ARPA-E award to attend Rare-Earth and Future Permanent Magnets workshop at Annapolis, MD 2014

Publications

1. R. P. Chaudhary, S. Barman, M. N. Huda, and A. R. Koymen, Effect of hydrogen in plasma generated Pd nanoparticles (submitted).
2. R. P. Chaudhary, K. Kangasniemi, M. Takahashi, S. K. Mohanty, and A. R Koymen, Fe core – Carbon shell nanoparticles as advanced MRI contrast enhancer (submitted).
3. K. Gandha, R. P. Chaudhary, J. Mohapatra, A. R. Koymen, and J. P. Liu, Giant Exchange Bias and Its Angular Dependence in Co/CoO Core-Shell Nanowires Assemblies. *Phys. Lett.* 2017, https://doi.org/10.1016/j.physleta.2017.04.025.
4. R. P. Chaudhary, and Ali. R. Koymen, Synthesis of magnetic GdC_2 nanoparticles using cavitation plasma, *Mater. Lett.* 2015, 158, 194-197.
5. R. P. Chaudhary, S. K. Mohanty, and A. R Koymen, Novel method for synthesis of Fe core and C shell magnetic nanoparticles, *Carbon* 2014, 79, 67-73.
6. R. P. Chaudhary, S. K. Mohanty, and A. R. Koymen, New method for synthesis of Pt nanoparticles embedded in Carbon matrix, *J. Nanosci. Nanotechnol.*2011, 11, 10396-400.
7. R. Chaudhary, V. Varadarajan, S. K. Mohanty and A. R. Koymen, Fluorescent Carbon nanoparticles synthesized from benzene by electric plasma discharge, *Proc. SPIE,* 2011, 7908, 79080C-1.

Conference presentations

1. Unconventional top-down synthesis of FeNi core and C shell magnetic nanoparticle, APS March Meeting, San Antonio, TX, USA March 2015 (Oral)
2. Synthesis of graphene-like graphite sheets and its ferromagnetism, APS March Meeting, San Antonio, TX, USA March 2015 (Oral)
3. Synthesis of magnetic GdC2 nanoparticles using cavitation plasma, APS March Meeting, San Antonio, TX, USA March 2015 (Poster)
4. Ferromagnetism in graphene-like nano graphite, ACES Meeting, University of Texas at Arlington, Arlington, TX, USA March 2015 (Oral)
5. Synthesis of core-shell iron nanoparticles via a new (novel) approach, APS March Meeting, Denver, Co, USA March 2014 (Oral)
6. MRI contrast enhancement using Magnetic Carbon Nanoparticles, APS March Meeting, Denver, Co, USA March 2014 (Poster)
7. Novel method for synthesis of Fe core and C shell magnetic nanoparticles, Texas Society of Microscopy (TSM) Irving, TX, USA March 2014 (Oral)
8. New method to synthesize nanoparticles for alternative energy and biological applications, WBT Innovation Marketplace, Arlington, TX, USA March 2011 (Poster)

References

[1] B.D. Cullity, C.D. Graham, Introduction to magnetic materials, John Wiley & Sons, 2011.

[2] S. Tikadzumi, Physics of ferromagnetism, Magnetic Characteristics and Practical Applications, (1983).

[3] R.C. O'Handley, Modern Magnetic Materials: Principles and Applications, Wiley, 1999.

[4] N.A. Spaldin, Magnetic materials: fundamentals and applications, Cambridge University Press, 2010.

[5] K. Gandha, J. Mohapatra, J.P. Liu, Coherent magnetization reversal and high magnetic coercivity in Co nanowire assemblies, Journal of Magnetism and Magnetic Materials.

[6] R.P. Chaudhary, S.K. Mohanty, A.R. Koymen, Novel method for synthesis of Fe core and C shell magnetic nanoparticles, Carbon, 79 (2014) 67-73.

[7] K. Gandha, N. Poudyal, Q. Zhang, J.P. Liu, Effect of $RuCl_3$ on Morphology and Magnetic Properties of CoNi Nanowires, IEEE Transactions on Magnetics, 49 (2013) 3273-3276.

[8] J.P. Liu, N. Poudyal, K. Gandha, Synthesis and Characterization of CoNi and FeCo Nanowires With High Coercivity, in: APS Meeting Abstracts, 2013.

[9] K. Gandha, K. Elkins, N. Poudyal, X. Liu, J.P. Liu, High Energy Product Developed from Cobalt Nanowires, Scientific Reports, 4 (2014) 5345.

[10] K.H. Gandha, K. Elkins, J.P. Liu, Synthesis of Fe Nanowires via a Novel Approach, in: APS March Meeting Abstracts, 2014, pp. 7009.

[11] K. Gandha, K. Elkins, N. Poudyal, J.P. Liu, Synthesis and characterization of CoFe2O4 nanoparticles with high coercivity, Journal of Applied Physics, 117 (2015) 17A736.

[12] K. Gandha, K. Elkins, N. Poudyal, J.P. Liu, Structure and magnetic properties of Co/CoO core-shell nanowires, in: APS Meeting Abstracts, 2015, pp. 30003.

[13] K. Gandha, P. Tsai, G. Chaubey, N. Poudyal, K. Elkins, J. Cui, J.P. Liu, Synthesis and characterization of FeCo nanowires with high coercivity, Nanotechnology, 26 (2015) 075601.

[14] K. Gandha, J. Mohapatra, M.K. Hossain, K. Elkins, N. Poudyal, K. Rajeshwar, J.P. Liu, Mesoporous iron oxide nanowires: synthesis, magnetic and photocatalytic properties, RSC Advances, 6 (2016) 90537-90546.

[15] K. Gandha, J. Mohapatra, N. Poudyal, K. Elkins, J.P. Liu, Enhanced coercivity in Co-doped α-Fe2O3 cubic nanocrystal assemblies prepared via a magnetic field-assisted hydrothermal synthesis, AIP Advances, 7 (2017) 056324.

[16] K. Gandha, K. Elkins, N. Poudyal, J.P. Liu, Angular dependence of magnetization in single crystalline cobalt nanowires, in: APS March Meeting Abstracts, 2016.

[17] K. Gandha, K. Elkins, N. Poudyal, J. Ping Liu, Synthesis and characterization of CoFe2O4 nanoparticles with high coercivity, Journal of Applied Physics, 117 (2015) 17A736.

[18] K. Gandha, R.P. Chaudhary, J. Mohapatra, A.R. Koymen, J. Ping Liu, Giant exchange bias and its angular dependence in Co/CoO core-shell nanowire assemblies, Physics Letters A.

[19] J.M.D. Coey, Permanent magnetism, Solid State Communications, 102 (1997) 101-105.

[20] J.M. Coey, Magnetism and magnetic materials, Cambridge University Press, 2010.

[21] K. Gandha, Synthesis and magnetic properties of high-aspect-ratio nanocrystals, in, University of Texas at Arlington, 2015.

[22] Y.L. Ma, X.B. Liu, K. Gandha, N.V. Vuong, Y.B. Yang, J.B. Yang, N. Poudyal, J. Cui, J.P. Liu, Preparation and magnetic properties of MnBi-based hard/soft composite magnets, Journal of Applied Physics, 115 (2014) 17A755.

[23] N. Poudyal, K. Elkins, K. Gandha, J.P. Liu, FeCo Coating on SmCo₅ Nanochips by a Sonochemical Method, IEEE Transactions on Magnetics, 51 (2015) 1-4.

[24] N. Poudyal, K. Gandha, K. Elkins, J.P. Liu, Anisotropic SmCo 5/FeCo core/shell nanocomposite chips prepared via electroless coating, (2015).

[25] N. Poudyal, K. Gandha, W. Wang, X. Liu, Z. Qiu, K. Elkins, J.P. Liu, J. Cui, Fabrication and Characterization of MnBi/Co and MnBi/FeCo Nanocomposite Bulk Magnets, in: APS Meeting Abstracts, 2015, pp. 30005.

[26] N. Poudyal, X. Liu, W. Wang, V.V. Nguyen, Y. Ma, K. Gandha, K. Elkins, J.P. Liu, K. Sun, M.J. Kramer, J. Cui, Processing of MnBi bulk magnets with enhanced energy product, AIP Advances, 6 (2016) 056004.

[27] N. Poudyal, G. Han, Z. Qiu, K. Elkins, J. Mohapatra, K. Gandha, R.B. Timmons, J.P. Liu, Cleaning of magnetic nanoparticle surfaces via cold plasmas treatments, AIP Advances, 7 (2017) 056233.

[28] N. Poudyal, K.H. Gandha, J. Liu, K.E. Elkins, H. Arami, J.P. Liu, Ferromagnetic FePt/Au Core/Shell Nanoparticles Prepared by Solvothermal Annealing, IEEE Magnetics Letters, 7 (2016) 1-5.

[29] E.H. Frei, S. Shtrikman, D. Treves, Critical Size and Nucleation Field of Ideal Ferromagnetic Particles, Physical Review, 106 (1957) 446-455.

[30] I.S. Jacobs, C.P. Bean, An Approach to Elongated Fine-Particle Magnets, Physical Review, 100 (1955) 1060-1067.

[31] H.-B. Braun, Thermally Activated Magnetization Reversal in Elongated Ferromagnetic Particles, Physical review letters, 71 (1993) 3557-3560.

[32] U. Nowak, R.W. Chantrell, E.C. Kennedy, Monte Carlo Simulation with Time Step Quantification in Terms of Langevin Dynamics, Physical review letters, 84 (2000) 163-166.

[33] F.E. Luborsky, Development of Elongated Particle Magnets, Journal of Applied Physics, 32 (1961) S171-S183.

[34] Y.-w. Jun, J.-w. Seo, J. Cheon, Nanoscaling Laws of Magnetic Nanoparticles and Their Applicabilities in Biomedical Sciences, Accounts of Chemical Research, 41 (2008) 179-189.

[35] N. Poudyal, Fabrication of superparamagnetic and ferromagnetic nanoparticles, ProQuest, 2008.

[36] V. Nandwana, Synthesis, characterization and potential applications of FePt nanoparticles, in, UNIVERSITY OF TEXAS AT ARLINGTON, 2009.

[37] K. Gandha, Synthesis and magnetic properties of high-aspect-ratio nanocrystals, in: Physics Department,

, University of Texas at Arlington, 2015.

[38] R.F. Service, Materials Science: Mixing Nanotube Structures to Make a Tiny Switch, Science, 271 (1996) 1232-1232.

[39] P.I. Yu, L.G. Vivas, A. Asenjo, A. Chuvilin, O. Chubykalo-fesenko, M. Vázquez, Magnetic structure of a single-crystal hcp electrodeposited cobalt nanowire, EPL (Europhysics Letters), 102 (2013) 17009.

[40] L.G. Vivas, M. Vázquez, V. Vega, J. García, W.O. Rosa, R.P.d. Real, V.M. Prida, Temperature dependent magnetization in Co-base nanowire arrays: Role of crystalline anisotropy, Journal of Applied Physics, 111 (2012) 07A325.

[41] F. Dumestre, B. Chaudret, C. Amiens, M.-C. Fromen, M.-J. Casanove, P. Renaud, P. Zurcher, Shape Control of Thermodynamically Stable Cobalt Nanorods through Organometallic Chemistry, Angewandte Chemie, 114 (2002) 4462-4465.

[42] B.L. Cushing, V.L. Kolesnichenko, C.J. O'Connor, Recent Advances in the Liquid-Phase Syntheses of Inorganic Nanoparticles, Chemical Reviews, 104 (2004) 3893-3946.

[43] C. Burda, X. Chen, R. Narayanan, M.A. El-Sayed, Chemistry and Properties of Nanocrystals of Different Shapes, Chemical Reviews, 105 (2005) 1025-1102.

[44] M.K. Hossain, G.F. Samu, K.H. Gandha, S. Santhanagopalan, J.P. Liu, C. Janáky, K. Rajeshwar, Solution Combustion Synthesis, Characterization, and Photocatalytic Activity of CuBi2O4 and its Nanocomposites with CuO and α-Bi2O3, The Journal of Physical Chemistry C, (2017).

[45] M.G. Spirin, S.B. Brichkin, V.F. Razumov, Studies on absorption spectra of uniform gold nanoparticles prepared in Triton X-100 reverse micelles, Journal of Photochemistry and Photobiology A: Chemistry, 196 (2008) 174-179.

[46] E. Shibata, R. Sergiienko, H. Suwa, T. Nakamura, Synthesis of amorphous carbon particles by an electric arc in the ultrasonic cavitation field of liquid benzene, Carbon, 42 (2004) 885-888.

[47] M. Muniz-Miranda, C. Gellini, P. Canton, P. Marsili, E. Giorgetti, SERS and catalytically active Ag/Pd nanoparticles obtained by combining laser ablation and galvanic replacement, Journal of Alloys and Compounds, 615, Supplement 1 (2014) S352-S356.

[48] R.P. Chaudhary, S.K. Mohanty, A.R. Koymen, New Method for Synthesis of Pt Nanoparticles Embedded in a Carbon Matrix, Journal of Nanoscience and Nanotechnology, 11 (2011) 10396-10400.

[49] R.P. Chaudhary, A.R. Koymen, Synthesis of magnetic GdC2 nanoparticles using cavitation plasma, Materials Letters, 158 (2015) 194-197.

[50] R.N. Thurston, 1 - Wave Propagation in Fluids and Normal Solids A2 - MASON, WARREN P, in: Physical Acoustics, Academic Press, 1964, pp. 1-110.

[51] C.E. Brennen, Cavitation and bubble dynamics, Cambridge University Press, 2013.

[52] A. Khachatryan, R. Sarkissyan, L. Hassratyan, V. Khachatryan, Influence of ultrasound on nanostructural iron formed by electrochemical reduction, Ultrasonics Sonochemistry, 11 (2004) 405-408.

[53] J.-L. Delplancke, J. Dille, J. Reisse, G.J. Long, A. Mohan, F. Grandjean, Magnetic Nanopowders: Ultrasound-Assisted Electrochemical Preparation and Properties, Chemistry of Materials, 12 (2000) 946-955.

[54] K.S. Suslick, M. Fang, T. Hyeon, Sonochemical Synthesis of Iron Colloids, Journal of the American Chemical Society, 118 (1996) 11960-11961.

[55] Y.T. Didenko, W.B. McNamara, K.S. Suslick, Hot Spot Conditions during Cavitation in Water, Journal of the American Chemical Society, 121 (1999) 5817-5818.

[56] W.B. McNamara, Y.T. Didenko, K.S. Suslick, Sonoluminescence temperatures during multi-bubble cavitation, Nature, 401 (1999) 772-775.

[57] E.A. Neppiras, Acoustic cavitation, Physics Reports, 61 (1980) 159-251.

[58] R. Chaudhary, V. Varadarajan, S.K. Mohanty, A.R. Koymen, Fluorescent carbon nanoparticles synthesized from benzene by electric plasma discharge, in, 2011, pp. 79080C-79080C-79089.

[59] B.D. Cullity, S.R. Stock, Elements of X-ray Diffraction, Prentice Hall, 2001.

[60] S.M. Turner, Transmission electron microscopy characterisation of 0-D nanomaterials, 2010.

[61] S.K. Sahi, <Sunil Sahi.pdf>, in: Physics, University of Texas at Arlington.

[62] B.C. Smith, Fundamentals of Fourier Transform Infrared Spectroscopy, Taylor & Francis, 1995.

[63] S.K. Sahi, <Synthesis and characterization of nanocomposite scintillators for radiation detection.pdf>, in, University of Texas at Arlington, May 2016.

[64] D. Weller, A. Moser, Thermal effect limits in ultrahigh-density magnetic recording, IEEE Transactions on Magnetics, 35 (1999) 4423-4439.

[65] C. Ross, Patterned Magnetic Recording Media, Annual Review of Materials Research, 31 (2001) 203-235.

[66] Y. Yang, L. Li, G. Chen, E. Liu, Synthesis and characterization of iron-based alloy nanoparticles for magnetorheological fluids, Journal of Magnetism and Magnetic Materials, 320 (2008) 2030-2038.

[67] M. Arruebo, M. Galán, N. Navascués, C. Téllez, C. Marquina, M.R. Ibarra, J. Santamaría, Development of Magnetic Nanostructured Silica-Based Materials as Potential Vectors for Drug-Delivery Applications, Chemistry of Materials, 18 (2006) 1911-1919.

[68] S. Laurent, D. Forge, M. Port, A. Roch, C. Robic, L. Vander Elst, R.N. Muller, Magnetic Iron Oxide Nanoparticles: Synthesis, Stabilization, Vectorization, Physicochemical Characterizations, and Biological Applications, Chemical Reviews, 108 (2008) 2064-2110.

[69] D.L. Huber, Synthesis, Properties, and Applications of Iron Nanoparticles, Small, 1 (2005) 482-501.

[70] Q.A. Pankhurst, J. Connolly, S.K. Jones, J. Dobson, Applications of magnetic nanoparticles in biomedicine, Journal of Physics D: Applied Physics, 36 (2003) R167.

[71] R. Weissleder, A. Bogdanov, E.A. Neuwelt, M. Papisov, Long-circulating iron oxides for MR imaging, Advanced Drug Delivery Reviews, 16 (1995) 321-334.

[72] L. Gu, V. Vardarajan, A.R. Koymen, S.K. Mohanty, Magnetic-field-assisted photothermal therapy of cancer cells using Fe-doped carbon nanoparticles, BIOMEDO, 17 (2012) 0180031-0180038.

[73] V. Gupta, M.K. Patra, A. Shukla, L. Saini, S. Songara, R. Jani, S.R. Vadera, N. Kumar, Synthesis of core–shell iron nanoparticles from decomposition of Fe–Sn nanocomposite and studies on their microwave absorption properties, Journal of Nanoparticle Research, 14 (2012) 1271.

[74] V.P. Dravid, J.J. Host, M.H. Teng, B.E.J. Hwang, D.L. Johnson, T.O. Mason, J.R. Weertman, Controlled-size nanocapsules, Nature, 374 (1995) 602-602.

[75] Y. Saito, T. Yoshikawa, M. Inagaki, M. Tomita, T. Hayashi, Growth and structure of graphitic tubules and polyhedral particles in arc-discharge, Chemical Physics Letters, 204 (1993) 277-282.

[76] J. Huo, H. Song, X. Chen, Preparation of carbon-encapsulated iron nanoparticles by co-carbonization of aromatic heavy oil and ferrocene, Carbon, 42 (2004) 3177-3182.

[77] R.S. Ruoff, D.C. Lorents, B. Chan, R. Malhotra, S. Subramoney, Single Crystal Metals Encapsulated in Carbon Nanoparticles, Science, 259 (1993) 346-348.

[78] J. Borysiuk, A. Grabias, J. Szczytko, M. Bystrzejewski, A. Twardowski, H. Lange, Structure and magnetic properties of carbon encapsulated Fe nanoparticles obtained by arc plasma and combustion synthesis, Carbon, 46 (2008) 1693-1701.

[79] J.H.J. Scott, S.A. Majetich, Morphology, structure, and growth of nanoparticles produced in a carbon arc, Physical Review B, 52 (1995) 12564-12571.

[80] Y. Lu, Z. Zhu, Z. Liu, Carbon-encapsulated Fe nanoparticles from detonation-induced pyrolysis of ferrocene, Carbon, 43 (2005) 369-374.

[81] T. Hayashi, S. Hirono, M. Tomita, S. Umemura, Magnetic thin films of cobalt nanocrystals encapsulated in graphite-like carbon, Nature, 381 (1996) 772-774.

[82] Z.H. Wang, C.J. Choi, B.K. Kim, J.C. Kim, Z.D. Zhang, Characterization and magnetic properties of carbon-coated cobalt nanocapsules synthesized by the chemical vapor-condensation process, Carbon, 41 (2003) 1751-1758.

[83] E.B. FLINT, K.S. SUSLICK, The Temperature of Cavitation, Science, 253 (1991) 1397-1399.

[84] R. Katoh, E. Yanase, H. Yokoi, S. Usuba, Y. Kakudate, S. Fujiwara, Possible new route for the production of C6 by ultrasound, Ultrasonics Sonochemistry, 5 (1998) 37-38.

[85] R. Sergiienko, E. Shibata, Z. Akase, H. Suwa, T. Nakamura, D. Shindo, Carbon encapsulated iron carbide nanoparticles synthesized in ethanol by an electric plasma discharge in an ultrasonic cavitation field, Materials Chemistry and Physics, 98 (2006) 34-38.

[86] R. Sergiienko, E. Shibata, Z. Akase, H. Suwa, D. Shindo, T. Nakamura, Synthesis of Fe-filled carbon nanocapsules by an electric plasma discharge in an ultrasonic cavitation field of liquid ethanol, Journal of Materials Research, 21 (2011) 2524-2533.

[87] J. Huo, H. Song, X. Chen, S. Zhao, C. Xu, Structural transformation of carbon-encapsulated iron nanoparticles during heat treatment at 1000 °C, Materials Chemistry and Physics, 101 (2007) 221-227.

[88] C. Yu, Y. Sun, X. Fan, Z. Zhao, J. Qiu, Hierarchical Carbon-Encapsulated Iron Nanoparticles as a Magnetically Separable Adsorbent for Removing Thiophene in Liquid Fuel, Particle & Particle Systems Characterization, 30 (2013) 637-644.

[89] J. Qiu, Y. Li, Y. Wang, Y. An, Z. Zhao, Y. Zhou, W. Li, Preparation of carbon-coated magnetic iron nanoparticles from composite rods made from coal and iron powders, Fuel Processing Technology, 86 (2004) 267-274.

[90] A. Ōya, S. Ōtani, Influences of particle size of metal on catalytic graphitization of non-graphitizing carbons, Carbon, 19 (1981) 391-400.

[91] A. Ōya, H. Marsh, Phenomena of catalytic graphitization, Journal of Materials Science, 17 (1982) 309-322.

[92] H. Marsh, D. Crawford, D.W. Taylor, Catalytic graphitization by iron of isotropic carbon from polyfurfuryl alcohol, 725–1090 K. A high resolution electron microscope study, Carbon, 21 (1983) 81-87.

[93] W. Zhou, X. Hu, X. Bai, S. Zhou, C. Sun, J. Yan, P. Chen, Synthesis and Electromagnetic, Microwave Absorbing Properties of Core–Shell Fe3O4–Poly(3, 4-ethylenedioxythiophene) Microspheres, ACS Applied Materials & Interfaces, 3 (2011) 3839-3845.

[94] R.M. Bozorth, Ferromagnetism, Wiley, 1993.

[95] O. Veiseh, J.W. Gunn, M. Zhang, Design and fabrication of magnetic nanoparticles for targeted drug delivery and imaging, Advanced Drug Delivery Reviews, 62 (2010) 284-304.

[96] R. Hao, R. Xing, Z. Xu, Y. Hou, S. Gao, S. Sun, Synthesis, Functionalization, and Biomedical Applications of Multifunctional Magnetic Nanoparticles, Advanced Materials, 22 (2010) 2729-2742.

[97] C.S.S.R. Kumar, F. Mohammad, Magnetic nanomaterials for hyperthermia-based therapy and controlled drug delivery, Advanced Drug Delivery Reviews, 63 (2011) 789-808.

[98] Y.-M. Huh, Y.-w. Jun, H.-T. Song, S. Kim, J.-s. Choi, J.-H. Lee, S. Yoon, K.-S. Kim, J.-S. Shin, J.-S. Suh, J. Cheon, In Vivo Magnetic Resonance Detection of Cancer by Using Multifunctional Magnetic Nanocrystals, Journal of the American Chemical Society, 127 (2005) 12387-12391.

[99] O. Bomatí-Miguel, M.P. Morales, P. Tartaj, J. Ruiz-Cabello, P. Bonville, M. Santos, X. Zhao, S. Veintemillas-Verdaguer, Fe-based nanoparticulate metallic alloys as contrast agents for magnetic resonance imaging, Biomaterials, 26 (2005) 5695-5703.

[100] E.A. Neuwelt, P. Várallyay, A.G. Bagó, L.L. Muldoon, G. Nesbit, R. Nixon, Imaging of iron oxide nanoparticles by MR and light microscopy in patients with malignant brain tumours, Neuropathology and Applied Neurobiology, 30 (2004) 456-471.

[101] E.M. Shapiro, S. Skrtic, K. Sharer, J.M. Hill, C.E. Dunbar, A.P. Koretsky, MRI detection of single particles for cellular imaging, Proceedings of the National Academy of Sciences of the United States of America, 101 (2004) 10901-10906.

[102] J.R. Slotkin, K.S. Cahill, S.A. Tharin, E.M. Shapiro, Cellular magnetic resonance imaging: Nanometer and micrometer size particles for noninvasive cell localization, Neurotherapeutics, 4 (2007) 428-433.

[103] J.-H. Lee, Y.-M. Huh, Y.-w. Jun, J.-w. Seo, J.-t. Jang, H.-T. Song, S. Kim, E.-J. Cho, H.-G. Yoon, J.-S. Suh, J. Cheon, Artificially engineered magnetic nanoparticles for ultra-sensitive molecular imaging, Nat Med, 13 (2007) 95-99.

[104] J.R. McCarthy, K.A. Kelly, E.Y. Sun, R. Weissleder, Targeted delivery of multifunctional magnetic nanoparticles, Nanomedicine, 2 (2007) 153-167.

[105] M. Lewin, N. Carlesso, C.-H. Tung, X.-W. Tang, D. Cory, D.T. Scadden, R. Weissleder, Tat peptide-derivatized magnetic nanoparticles allow in vivo tracking and recovery of progenitor cells, Nat Biotech, 18 (2000) 410-414.

[106] A. Moore, E. Marecos, J. Alexei Bogdanov, R. Weissleder, Tumoral Distribution of Long-circulating Dextran-coated Iron Oxide Nanoparticles in a Rodent Model, Radiology, 214 (2000) 568-574.

[107] K. Ohno, C. Mori, T. Akashi, S. Yoshida, Y. Tago, Y. Tsujii, Y. Tabata, Fabrication of Contrast Agents for Magnetic Resonance Imaging from Polymer-Brush-Afforded Iron

Oxide Magnetic Nanoparticles Prepared by Surface-Initiated Living Radical Polymerization, Biomacromolecules, 14 (2013) 3453-3462.

[108] W. Wei, W. Zhaohui, Y. Taekyung, J. Changzhong, K. Woo-Sik, Recent progress on magnetic iron oxide nanoparticles: synthesis, surface functional strategies and biomedical applications, Science and Technology of Advanced Materials, 16 (2015) 023501.

[109] B. Karagoz, J. Yeow, L. Esser, S.M. Prakash, R.P. Kuchel, T.P. Davis, C. Boyer, An Efficient and Highly Versatile Synthetic Route to Prepare Iron Oxide Nanoparticles/Nanocomposites with Tunable Morphologies, Langmuir, 30 (2014) 10493-10502.

[110] H. Bae, T. Ahmad, I. Rhee, Y. Chang, S.-U. Jin, S. Hong, Carbon-coated iron oxide nanoparticles as contrast agents in magnetic resonance imaging, Nanoscale Research Letters, 7 (2012) 44.

[111] C.G. Hadjipanayis, M.J. Bonder, S. Balakrishnan, X. Wang, H. Mao, G.C. Hadjipanayis, Metallic Iron Nanoparticles for MRI Contrast Enhancement and Local Hyperthermia, Small, 4 (2008) 1925-1929.

[112] A.-H. Lu, E.L. Salabas, F. Schüth, Magnetic Nanoparticles: Synthesis, Protection, Functionalization, and Application, Angewandte Chemie International Edition, 46 (2007) 1222-1244.

[113] S. Riaz, A. Akbar, S. Naseem, Controlled Nanostructuring of Multiphase Core-Shell Iron Oxide Nanoparticles, IEEE Transactions on Magnetics, 50 (2014) 1-4.

[114] C.B. Murray, S. Sun, H. Doyle, T. Betley, Monodisperse 3d Transition-Metal (Co,Ni,Fe) Nanoparticles and Their Assembly intoNanoparticle Superlattices, MRS Bulletin, 26 (2012) 985-991.

[115] S. Hofmann, R. Sharma, C. Ducati, G. Du, C. Mattevi, C. Cepek, M. Cantoro, S. Pisana, A. Parvez, F. Cervantes-Sodi, A.C. Ferrari, R. Dunin-Borkowski, S. Lizzit, L. Petaccia, A. Goldoni, J. Robertson, In situ Observations of Catalyst Dynamics during Surface-Bound Carbon Nanotube Nucleation, Nano Letters, 7 (2007) 602-608.

[116] D.A. Papaconstantopoulos, J.L. Fry, N.E. Brener, Ferromagnetism in hexagonal-close-packed elements, Physical Review B, 39 (1989) 2526-2528.

[117] X. He, L.T. Kong, B.X. Liu, Calculation of ferromagnetic states in metastable bcc and hcp Ni by projector-augmented wave method, Journal of Applied Physics, 97 (2005) 106107.

[118] W. Tian, H.P. Sun, X.Q. Pan, J.H. Yu, M. Yeadon, C.B. Boothroyd, Y.P. Feng, R.A. Lukaszew, R. Clarke, Hexagonal close-packed Ni nanostructures grown on the (001) surface of MgO, Applied Physics Letters, 86 (2005) 131915.

[119] C.S. Tian, D. Qian, D. Wu, R.H. He, Y.Z. Wu, W.X. Tang, L.F. Yin, Y.S. Shi, G.S. Dong, X.F. Jin, X.M. Jiang, F.Q. Liu, H.J. Qian, K. Sun, L.M. Wang, G. Rossi, Z.Q. Qiu, J. Shi, Body-Centered-Cubic Ni and Its Magnetic Properties, Physical review letters, 94 (2005) 137210.

[120] N. Cordente, M. Respaud, F. Senocq, M.-J. Casanove, C. Amiens, B. Chaudret, Synthesis and Magnetic Properties of Nickel Nanorods, Nano Letters, 1 (2001) 565-568.

[121] S. Carenco, C. Boissière, L. Nicole, C. Sanchez, P. Le Floch, N. Mézailles, Controlled Design of Size-Tunable Monodisperse Nickel Nanoparticles, Chemistry of Materials, 22 (2010) 1340-1349.

[122] C.N. Chinnasamy, B. Jeyadevan, K. Shinoda, K. Tohji, A. Narayanasamy, K. Sato, S. Hisano, Synthesis and magnetic properties of face-centered-cubic and hexagonal-close-packed Ni nanoparticles through polyol process, Journal of Applied Physics, 97 (2005) 10J309.

[123] Y. Mi, D. Yuan, Y. Liu, J. Zhang, Y. Xiao, Synthesis of hexagonal close-packed nanocrystalline nickel by a thermal reduction process, Materials Chemistry and Physics, 89 (2005) 359-361.

[124] F. Andrej, L. Jun, H. Lars, J. Ulf, M. Martin, Crystallization characteristics and chemical bonding properties of nickel carbide thin film nanocomposites, Journal of Physics: Condensed Matter, 26 (2014) 415501.

[125] Z. Zhang, T.M. Nenoff, J.Y. Huang, D.T. Berry, P.P. Provencio, Room Temperature Synthesis of Thermally Immiscible Ag−Ni Nanoalloys, The Journal of Physical Chemistry C, 113 (2009) 1155-1159.

[126] R. Ferrando, J. Jellinek, R.L. Johnston, Nanoalloys: From Theory to Applications of Alloy Clusters and Nanoparticles, Chemical Reviews, 108 (2008) 845-910.

[127] Y. Zhang, W. Huang, S.E. Habas, J.N. Kuhn, M.E. Grass, Y. Yamada, P. Yang, G.A. Somorjai, Near-Monodisperse Ni−Cu Bimetallic Nanocrystals of Variable Composition: Controlled Synthesis and Catalytic Activity for H2 Generation, The Journal of Physical Chemistry C, 112 (2008) 12092-12095.

[128] A.W.C. van den Berg, C.O. Arean, Materials for hydrogen storage: current research trends and perspectives, Chemical Communications, (2008) 668-681.

[129] F. Raimondi, G.G. Scherer, R. Kötz, A. Wokaun, Nanoparticles in Energy Technology: Examples from Electrochemistry and Catalysis, Angewandte Chemie International Edition, 44 (2005) 2190-2209.

[130] A. Chen, C. Ostrom, Palladium-Based Nanomaterials: Synthesis and Electrochemical Applications, Chemical Reviews, 115 (2015) 11999-12044.

[131] N.G. Semaltianos, P. Petkov, S. Scholz, L. Guetaz, Palladium or palladium hydride nanoparticles synthesized by laser ablation of a bulk palladium target in liquids, Journal of Colloid and Interface Science, 402 (2013) 307-311.

[132] M. Khanuja, B.R. Mehta, P. Agar, P.K. Kulriya, D.K. Avasthi, Hydrogen induced lattice expansion and crystallinity degradation in palladium nanoparticles: Effect of hydrogen concentration, pressure, and temperature, Journal of Applied Physics, 106 (2009) 093515.

[133] H. Huang, S. Bao, Q. Chen, Y. Yang, Z. Jiang, Q. Kuang, X. Wu, Z. Xie, L. Zheng, Novel hydrogen storage properties of palladium nanocrystals activated by a pentagonal cyclic twinned structure, Nano Research, 8 (2015) 2698-2705.

[134] W. Ludwig, A. Savara, R.J. Madix, S. Schauermann, H.-J. Freund, Subsurface Hydrogen Diffusion into Pd Nanoparticles: Role of Low-Coordinated Surface Sites and Facilitation by Carbon, The Journal of Physical Chemistry C, 116 (2012) 3539-3544.

[135] R. Campesi, F. Cuevas, R. Gadiou, E. Leroy, M. Hirscher, C. Vix-Guterl, M. Latroche, Hydrogen storage properties of Pd nanoparticle/carbon template composites, Carbon, 46 (2008) 206-214.

[136] O. Savadogo, K. Lee, K. Oishi, S. Mitsushima, N. Kamiya, K.I. Ota, New palladium alloys catalyst for the oxygen reduction reaction in an acid medium, Electrochemistry Communications, 6 (2004) 105-109.

[137] B. Amin-Ahmadi, H. Idrissi, M. Galceran, M.S. Colla, J.P. Raskin, T. Pardoen, S. Godet, D. Schryvers, Effect of deposition rate on the microstructure of electron beam evaporated nanocrystalline palladium thin films, Thin Solid Films, 539 (2013) 145-150.

[138] B.D. Adams, G. Wu, S. Nigro, A. Chen, Facile Synthesis of Pd−Cd Nanostructures with High Capacity for Hydrogen Storage, Journal of the American Chemical Society, 131 (2009) 6930-6931.

[139] Y. Zhao, S.-J. Qin, Y. Li, F.-X. Deng, Y.-Q. Liu, G.-B. Pan, Electrodeposition of dendritic Pd nanoarchitectures on n-GaN(0001): nucleation and electrocatalysis for direct formic acid fuel cells, Electrochimica Acta, 145 (2014) 148-153.

[140] V.B. Parambhath, R. Nagar, K. Sethupathi, S. Ramaprabhu, Investigation of Spillover Mechanism in Palladium Decorated Hydrogen Exfoliated Functionalized Graphene, The Journal of Physical Chemistry C, 115 (2011) 15679-15685.

[141] K. Suslick, Handbook of heterogeneous catalysis, Wiley-VCH, Weinheim, Germany, 1997.

[142] G. Kresse, J. Furthmüller, Efficient iterative schemes for ab initio total-energy calculations using a plane-wave basis set, Physical Review B, 54 (1996) 11169-11186.

[143] G. Kresse, J. Furthmüller, Efficiency of ab-initio total energy calculations for metals and semiconductors using a plane-wave basis set, Computational Materials Science, 6 (1996) 15-50.

[144] P. Hohenberg, W. Kohn, Inhomogeneous Electron Gas, Physical Review, 136 (1964) B864-B871.

[145] W. Kohn, L.J. Sham, Self-Consistent Equations Including Exchange and Correlation Effects, Physical Review, 140 (1965) A1133-A1138.

[146] P.E. Blöchl, Projector augmented-wave method, Physical Review B, 50 (1994) 17953-17979.

[147] M. Gajdoš, K. Hummer, G. Kresse, J. Furthmüller, F. Bechstedt, Linear optical properties in the projector-augmented wave methodology, Physical Review B, 73 (2006) 045112.

[148] J.P. Perdew, K. Burke, Y. Wang, Generalized gradient approximation for the exchange-correlation hole of a many-electron system, Physical Review B, 54 (1996) 16533-16539.

[149] M. Methfessel, A.T. Paxton, High-precision sampling for Brillouin-zone integration in metals, Physical Review B, 40 (1989) 3616-3621.

[150] P.E. Blöchl, O. Jepsen, O.K. Andersen, Improved tetrahedron method for Brillouin-zone integrations, Physical Review B, 49 (1994) 16223-16233.

[151] M. Ellner, Zusammenhang zwischen strukturellen und thermo-dynamischen eigenschaften bei phasen der kupfer-familie in T10-B4-systemen, Journal of the Less Common Metals, 78 (1981) 21-32.

[152] F.A. Lewis, The palladium hydrogen system, Academic Press, 1967.

[153] H. Kobayashi, M. Yamauchi, H. Kitagawa, Y. Kubota, K. Kato, M. Takata, On the Nature of Strong Hydrogen Atom Trapping Inside Pd Nanoparticles, Journal of the American Chemical Society, 130 (2008) 1828-1829.

[154] R. Caputo, A.L.I. Alavi, Where do the H atoms reside in PdH x systems?, Molecular Physics, 101 (2003) 1781-1787.

[155] P. Esquinazi, D. Spemann, R. Hohne, A. Setzer, K.H. Han, T. Butz, Induced magnetic ordering by proton irradiation in graphite, Physical review letters, 91 (2003) 227201.

[156] A.W. Mombru, H. Pardo, R. Faccio, O.F. de Lima, E.R. Leite, G. Zanelatto, A.J.C. Lanfredi, C.A. Cardoso, F.M. Araujo-Moreira, Multilevel ferromagnetic behavior of room-temperature bulk magnetic graphite, Phys Rev B, 71 (2005).

[157] P. Esquinazi, R. Hohn, Magnetism in carbon structures, J Magn Magn Mater, 290 (2005) 20-27.

[158] Ferromagnetism in oriented graphite samples.

[159] J. Červenka, M.I. Katsnelson, C.F.J. Flipse, Room-temperature ferromagnetism in graphite driven by two-dimensional networks of point defects, Nature Physics, 5 (2009) 840-844.

[160] D. Soriano, N. Leconte, P. Ordejón, J.-C. Charlier, J.-J. Palacios, S. Roche, Magnetoresistance and Magnetic Ordering Fingerprints in Hydrogenated Graphene, Physical review letters, 107 (2011).

[161] K. Tada, J. Haruyama, H.X. Yang, M. Chshiev, T. Matsui, H. Fukuyama, Graphene magnet realized by hydrogenated graphene nanopore arrays, Applied Physics Letters, 99 (2011) 183111.

[162] E. Duplock, M. Scheffler, P. Lindan, Hallmark of Perfect Graphene, Physical review letters, 92 (2004).

[163] A. Rode, E. Gamaly, A. Christy, J. Fitz Gerald, S. Hyde, R. Elliman, B. Luther-Davies, A. Veinger, J. Androulakis, J. Giapintzakis, Unconventional magnetism in all-carbon nanofoam, Phys Rev B, 70 (2004).

[164] <Magnetic carbon.pdf>.

[165] H. Ohldag, T. Tyliszczak, R. Höhne, D. Spemann, P. Esquinazi, M. Ungureanu, T. Butz, π-Electron Ferromagnetism in Metal-Free Carbon Probed by Soft X-Ray Dichroism, Physical review letters, 98 (2007).

[166] R.P. Chaudhary, S.K. Mohanty, A.R. Koymen, New method for synthesis of Pt nanoparticles embedded in a carbon matrix, Journal of nanoscience and nanotechnology, 11 (2011) 10396-10400.

[167] Q. Hu, T.J. Kneafsey, R.C. Trautz, J.S.Y. Wang, Tracer Penetration into Welded Tuff Matrix from Flowing Fractures, Vadose Zone Journal, 1 (2002) 102-112.

[168] Q. Hu, R.P. Ewing, S. Dultz, Low pore connectivity in natural rock, Journal of Contaminant Hydrology, 133 (2012) 76-83.

[169] S. Peng, Q. Hu, R.P. Ewing, C. Liu, J.M. Zachara, Quantitative 3-D Elemental Mapping by LA-ICP-MS of a Basaltic Clast from the Hanford 300 Area, Washington, USA, Environmental Science & Technology, 46 (2012) 2025-2032.

[170] Q. Hu, X. Mao, Application of Laser Ablation-Inductively Coupled Plasma-Mass Spectrometry to studies of chemical diffusion, sorption, and transport in natural rock, GEOCHEMICAL JOURNAL, 46 (2012) 459-475.

[171] S. Peng, Q. Hu, LA-ICP-MS Calibrations for Intact Rock Samples with Internal Standard and Modified Constant-Sum Methods, American Journal of Analytical Chemistry, 03 (2012) 168-174.

[172] M. Kurosawa, S.E. Jackson, S. Sueno, Trace Element Analysis of NIST SRM 614 and 616 Glass Reference Materials by Laser Ablation Microprobe-Inductively Coupled Plasma-Mass Spectrometry, Geostandards Newsletter, 26 (2002) 75-84.

[173] J.C. Meyer, A.K. Geim, M.I. Katsnelson, K.S. Novoselov, T.J. Booth, S. Roth, The structure of suspended graphene sheets, Nature, 446 (2007) 60-63.

[174] S. Kim, R. Sergiienko, E. Shibata, Y. Hayasaka, T. Nakamura, Production of Graphite Nanosheets by Low-Current Plasma Discharge in Liquid Ethanol, Materials Transactions, 51 (2010) 1455-1459.

[175] J.C. Meyer, A.K. Geim, M.I. Katsnelson, K.S. Novoselov, D. Obergfell, S. Roth, C. Girit, A. Zettl, On the roughness of single- and bi-layer graphene membranes, Solid State Communications, 143 (2007) 101-109.

[176] Y. Hernandez, V. Nicolosi, M. Lotya, F.M. Blighe, Z. Sun, S. De, I.T. McGovern, B. Holland, M. Byrne, Y.K. Gun'Ko, J.J. Boland, P. Niraj, G. Duesberg, S. Krishnamurthy, R. Goodhue, J. Hutchison, V. Scardaci, A.C. Ferrari, J.N. Coleman, High-yield production of graphene by liquid-phase exfoliation of graphite, Nature nanotechnology, 3 (2008) 563-568.

[177] A.H.C. Sirk, D.R. Sadoway, Electrochemical Synthesis of Diamondlike Carbon Films, Journal of The Electrochemical Society, 155 (2008) E49.

[178] <Tracer Penetration into Welded Tuff Matrix from Flowing Fractures.pdf>.

[179] P. Esquinazi, A. Setzer, R. Höhne, C. Semmelhack, Y. Kopelevich, D. Spemann, T. Butz, B. Kohlstrunk, M. Lösche, Ferromagnetism in oriented graphite samples, Phys Rev B, 66 (2002).

[180] J. Barzola-Quiquia, P. Esquinazi, M. Rothermel, D. Spemann, T. Butz, Magnetic order in proton irradiated graphite: Curie temperatures and magnetoresistance effect, Journal of Nuclear Materials, 389 (2009) 336-340.

[181] O. Yazyev, M. Katsnelson, Magnetic Correlations at Graphene Edges: Basis for Novel Spintronics Devices, Physical review letters, 100 (2008).

[182] J. Robertson, Hard amorphous (diamond-like) carbons, Progress in Solid State Chemistry, 21 (1991) 199-333.

[183] <Interpretation of Raman spectra of disordered and amorphous carbon.pdf>.

[184] <Ferromagnetic spots in graphite produced by proton irradiation.pdf>.

[185] <Chemical storage of hydrogen in few-layer graphene.pdf>.

[186] Z. Yang, Y. Sun, L.B. Alemany, T.N. Narayanan, W.E. Billups, Birch reduction of graphite. Edge and interior functionalization by hydrogen, Journal of the American Chemical Society, 134 (2012) 18689-18694.

[187] <organic ferromagnets.pdf>.

[188] X. Yang, H. Xia, X. Qin, W. Li, Y. Dai, X. Liu, M. Zhao, Y. Xia, S. Yan, B. Wang, Correlation between the vacancy defects and ferromagnetism in graphite, Carbon, 47 (2009) 1399-1406.

[189] M.A. Ramos, J. Barzola-Quiquia, P. Esquinazi, A. Muñoz-Martin, A. Climent-Font, M. García-Hernández, Magnetic properties of graphite irradiated with MeV ions, Phys Rev B, 81 (2010).

[190] <Peculiar localized state at zigzag graphite edge.pdf>.

[191] Y.W. Son, M.L. Cohen, S.G. Louie, Half-metallic graphene nanoribbons, Nature, 444 (2006) 347-349.

[192] K. Kusakabe, M. Maruyama, Magnetic nanographite, Phys Rev B, 67 (2003).

[193] J.-C. Park, H.-K. Moon, D.-K. Kim, S.-H. Byeon, B.-C. Kim, K.-S. Suh, Morphology and cathodoluminescence of Li-doped Gd2O3:Eu3+, a red phosphor operating at low voltages, Applied Physics Letters, 77 (2000) 2162-2164.

[194] D. Roberts, W.L. Zhu, C.M. Frommen, Z. Rosenzweig, Synthesis of gadolinium oxide magnetoliposomes for magnetic resonance imaging, Journal of Applied Physics, 87 (2000) 6208-6210.

[195] V.K. Pecharsky, J.K.A. Gschneidner, Giant Magnetocaloric Effect in ${\mathrm{Gd}}_{5}({\mathrm{Si}}_{2}{\mathrm{Ge}}_{2})$, Physical review letters, 78 (1997) 4494-4497.

[196] P.K. Lightfoot, V.A. Kudryavtsev, N.J.C. Spooner, I. Liubarsky, R. Luscher, N.J.T. Smith, Development of a gadolinium-loaded liquid scintillator for solar neutrino detection and neutron measurements, Nuclear Instruments and Methods in Physics Research Section A: Accelerators, Spectrometers, Detectors and Associated Equipment, 522 (2004) 439-446.

[197] J.A. Ransohoff, Nuclear reactor control rods, in, Google Patents, 1963.

[198] S.A. Enger, V. Giusti, M.-A. Fortin, H. Lundqvist, P.M. af Rosenschöld, Dosimetry for gadolinium neutron capture therapy (GdNCT), Radiation Measurements, 59 (2013) 233-240.

[199] N. Dewi, H. Yanagie, H. Zhu, K. Demachi, A. Shinohara, K. Yokoyama, M. Sekino, Y. Sakurai, Y. Morishita, N. Iyomoto, T. Nagasaki, Y. Horiguchi, Y. Nagasaki, J. Nakajima, M. Ono, K. Kakimi, H. Takahashi, Tumor growth suppression by gadolinium-

neutron capture therapy using gadolinium-entrapped liposome as gadolinium delivery agent, Biomedicine & Pharmacotherapy, 67 (2013) 451-457.

[200] C. Salt, A.J. Lennox, M. Takagaki, J.A. Maguire, N.S. Hosmane, Boron and gadolinium neutron capture therapy, Russian Chemical Bulletin, 53 (2004) 1871-1888.

[201] M.J. Moghaddam, L. de Campo, M. Hirabayashi, P.A. Bean, L.J. Waddington, J.A. Scoble, G. Coia, C.J. Drummond, Gadolinium-DTPA amphiphile nanoassemblies: agents for magnetic resonance imaging and neutron capture therapy, Biomaterials Science, 2 (2014) 924-935.

[202] I. Waki, Y. Sato, K. Motomiya, B. Jeyadevan, K. Tohji, Efficient Synthesis of Gadolinium Carbide Encapsulating Carbon Nanocapsules, AIP Conference Proceedings, 898 (2007) 139-142.

[203] J.M.D. Coey, V. Skumryev, K. Gallagher, Rare-earth metals: Is gadolinium really ferromagnetic?, Nature, 401 (1999) 35-36.

[204] T. Sakai, G.y. Adachi, J. Shiokawa, Magnetic properties of the system GdC2-DyC2, Journal of Applied Physics, 50 (1979) 3592-3595.

[205] P.Z. Si, I. Škorvánek, J. Kováč, D.Y. Geng, X.G. Zhao, Z.D. Zhang, Structure and magnetic properties of Gd nanoparticles and carbon coated Gd/GdC2 nanocapsules, Journal of Applied Physics, 94 (2003) 6779-6784.

[206] S. Subramoney, R.S. Ruoff, D.C. Lorents, B. Chan, R. Malhotra, M.J. Dyer, K. Parvin, Magnetic separation of GdC2 encapsulated in carbon nanoparticles, Carbon, 32 (1994) 507-513.

[207] J.A. Nelson, L.H. Bennett, M.J. Wagner, Solution Synthesis of Gadolinium Nanoparticles, Journal of the American Chemical Society, 124 (2002) 2979-2983.

[208] X.G. Liu, D.Y. Geng, Q. Zhang, J.J. Jiang, W. Liu, Z.D. Zhang, Microstructure and magnetic properties of graphite-coated Gd nanocapsules, Applied Physics Letters, 94 (2009) 103104.

[209] N.V. Tarasenko, A.V. Butsen, A.A. Nevar, Laser ablation of gadolinium targets in liquids for nanoparticle preparation, Applied Physics A, 93 (2008) 837-841.

[210] C. Zhang, G. Lu, Z. Sun, J. Yu, Catalytic graphitization of carbon/carbon composites by lanthanum oxide, Journal of Rare Earths, 30 (2012) 128-132.

Biographical information

Rakesh Chaudhary earned his BSc degree in Physics at M. G. Science College, Gujarat University, India in 2005. He completed his MSc in 2007 at Sardar Patel University, India. He came to USA for further studies and he completed his MS in Materials Science and Engineering at University of Texas at Arlington in 2010. He started his PhD studies in 2011 under supervision of Prof. Ali R. Koymen at University of Texas at Arlington. His thesis research was focused on the plasma-based synthesis of nanostructured materials and their characterization. He is the author of 7 papers (5 published and 2 submitted). He wants to continue his research in magnetism and magnetic material.